STUDIES ON PERFORMANCE CHARACTERISTICS

OF

NONEQUILIBRIUM PLASMA FARADAY AND DISK MHD GENERATORS

BY

YOSHITAKA INUI

MAY 1987

DEPARTMENT OF ELECTRICAL ENGINEERING
KYOTO UNIVERSITY

STUDIES ON PERFORMANCE CHARACTERISTICS

OF

NONEQUILIBRIUM PLASMA FARADAY AND DISK MHD GENERATORS

BY

YOSHITAKA INUI

MAY 1987

DEPARTMENT OF ELECTRICAL ENGINEERING
KYOTO UNIVERSITY

CONTENTS

CHAPTER 1

GENERAL INTRODUCTION

1.1 Importance and Research Trend on Nonequilibrium MHD Electrical Power Generation

Fairly long ago, it was pointed out that the total thermal efficiency of a heat power plant must be more increased to utilize efficiently fossil fuels such as petroleum, coal, etc. and to decrease the thermal pollution bringing with air contamination. As an MHD(magnetohydrodynamic)-steam binary power plant is expected to have a potential to improve the thermal efficiency of the power one to 50 to 60 %, many researches on MHD generator have been carried out in many countries[1],[2] since the first success in the MHD power generation in 1959 by Kantrowitz, Rosa, et al. at AVCO Everett Research Laboratory in USA[3].

The MHD generators using the gas plasma as the working fluid are classified into the following two types according to its sort[4]. One is the open-cycle MHD generator in which alkali metal seeded fossil fuel combustion gas plasma of about 2800 K is used as the working fluid. The other is the closed-cycle or the nonequilibrium plasma MHD generator in which nonequilibrium one of the alkali metal seeded noble gas of about 2000 K is used.

In relation to the open-cycle MHD generator, a large number of experimental and theoretical studies have been done in many countries. Currently, in USA, many experiments are performed by using large scale facilities, such as CDIF(Component Development & Integration Facility) in Montana[5],[6], CFFF(Coal Fired Flow Facility) in UTSI(University of Tennessee Space Institute)[7], etc.

In USSR, the U-25 pilot plant of maximum output 20 MW in High Temperature Institute is being operated for more than 15 years and the U-500 plant of the maximum output 500 MW is now under construction[1],[2]. In Japan, many experiments have been carried out mainly in ETL(Electrotechnical Laboratory)[8].

In relation to the nonequilibrium plasma MHD generator, which is dealt with in this thesis, at the start, it was planed under the conception that it would be able to be combined with HTGR(High Temperature Gas Reactor) and fundamental experiments using shock tube were performed by Zauderer[9], Brederlow[10], et al. However, afterwards, it was made clear that the gas temperature at the outlet of HTGR does not exceed 1300 K and accordingly there is no possibility the nonequilibrium generator is combined with HTGR. Nevertheless, Shioda[11], Rietjens[12], et al. changed the heat source from HTGR to fossil fuel fired heat exchanger[13], and they are continuing the researches on the nonequilibrium plasma MHD generator, because it has the following advantages in comparison with the open-cycle MHD generator[2].

(1) The generator size is small, because the output power density is large.

(2) When the fossil fuel fired heat exchanger is used as the heat source, there is no necessity for using a special combustor and the heat of the fossil fuel combustion gas can be utilized very efficiently, because the temperature of the fossil fuel flame in the air of room temperature is almost equal to the stagnation temperature which is required to the nonequilibrium plasma MHD generator.

(3) The nonequilibrium plasma generator can be combined with a fusion reactor in future.

(4) Since the temperature of the working fluid is about 2000 K, high reliability can be expected from the viewpoint of channel material.

Up to now, Shioda, et al. have already developed the

regenerative heat exchanger[14], and now they are performing experiments of the nonequilibrium plasma MHD generator by the blow down MHD facility FUJI-I[15],[16] which was made by themselves. Rietjens, et al. also have been completed the blow down experimental facility, and they are performing experiments of the nonequilibrium plasma MHD generator by it[17].

On the other hand, the brief history of the theoretical researches on the nonequilibrium plasma MHD generator is as follows. In 1964, Kerrebrock pointed out the existence of ionization instability of the nonequilibrium plasma by the analysis using the linear perturbation theory in the first place[18]. Since the ionization instability much deteriorates generator performances, many analyses using linear perturbation theory were performed by Solbes[19], Nelson & Haines[20], Nakamura & Riedmüllar[21], Yoshikawa[22], et al. and it was shown that the plasma is stable when the seed is fully ionized. However, the linear perturbation theory can only distinguish the stability of uniform plasma and it cannot give any information about the transient formation process and the final steady state of the current distribution in the channel. For making clear those transient and steady states, it is most useful to solve numerically the basic nonlinear differential equations which govern the ionization and the recombination phenomena of the working plasma in the channel. Such numerical analyses have been carried out by Velikov[23], Lengyel[24], Unkel[25], Blom[26], Ishikawa[27], Hara[28],[29], et al. However, they could not sufficiently explain the experimental results because most of them did not take into the account the effect of the convection of the plasma[24]-[27] and others assumed some periodic conditions in one pitch region of the generator[28],[29].

1.2 Purpose and Synopsis of This Thesis

Considering the above-mentioned matters, this thesis aims, at explaining theoretically the transient and the steady current distributions and the other generator performances observed in the experiments by the two-dimensional time-dependent numerical analysis of the working plasma, in which the effect of the convection of the plasma is taken into account and the periodic conditions in one pitch region are not imposed. In this connection, since it was shown experimentally by Shioda, et al. that the disk generator possesses an advantage in suppressing the ionization instability of the plasma over the linear Faraday generator[30]-[32], the author adopts not only the linear Faraday generator but also the disk one as the research subjects. Also, as the working fluid, cesium or potassium seeded argon gas plasma and cesium seeded helium one are chosen because Shioda, Rietjens, et al. use them in the experiments.

In Chapter 2, there are introduced a two-dimensional time-dependent numerical solution of the small-sized linear Faraday generator with constant rectangular cross section using alkali metal seeded argon plasma, in which the convection effect is taken into account and the periodic conditions in one pitch region are not imposed. At first, the channel model of the linear Faraday generator used in the numerical analysis and the basic equations which govern the partially ionized nonequilibrium plasma are introduced. Next, some inevitable assumptions are introduced and the basic equations are transformed into the simplified two-dimensional basic equations to be solved, and also the boundary conditions are presented. And the numerical solution for calculating the electric potential in the channel by applying the finite element method to the above two-dimensional basic equations and the boundary conditions is derived. Finally, the method to compute the current stream function by using the electric potential and the ones to evaluate the electron temperature and the electron

density are shown.

In Chapter 3, the transient and the steady current distributions in the linear Faraday generator using the cesium seeded argon plasma are investigated by the numerical solution introduced in the preceding chapter. At first, the transient formation process and the steady state of the inhomogeneous current distributions are made clear and it is shown that those calculated distributions are in good agreement with the experimental results. Next, the influences of the electrode configuration and the convection effect of the plasma on the current distribution are investigated, and it is clarified that the main factors which govern the transient and the steady current distributions are the ionization instability and the convection effect of the plasma.

In Chapter 4, the influences of the various factors on the current distribution in the channel and the other generator performances are investigated. At first, the influences of the load resistance, the seed fraction and the magnetic flux density on the performance characteristics of the generator using the cesium seeded argon plasma are made clear. Next, the same investigations are performed with respect to the generator using the potassium seeded argon plasma and the differences between the former and the latter characteristics are also made clear.

In Chapter 5, the two-dimensional time-dependent numerical solution for the small-sized outflow disk generator is introduced. At first, the channel model of the disk generator and the basic equations used in the numerical analysis are introduced. Next some assumptions are introduced and the basic equations are transformed into the simplified two-dimensional basic equations to be solved, and also the boundary conditions are presented. And the numerical solution for calculating the electric potential by applying the finite element method is derived. Finally, the method to compute the current stream function and the ones to evaluate the electron temperature and the electron density are shown.

In Chapter 6, the transient and the steady current distributions in the disk generator using the cesium seeded argon plasma are studied by the numerical solution obtained in the preceding chapter. At first, the transient formation process and the steady state of the inhomogeneous current distributions are made clear. Also, the features of the distributions of the current, the electron temperature, the electron density, the conductivity and the electric potential in the steady state are clarified. Next, the influence of the magnetic flux density on the current distribution is studied. Also, the advantage of the disk generator in stabilizing the plasma in comparison with the linear Faraday generator, which has been known by the previous experiments, is theoretically confirmed by the present analysis.

In Chapter 7, the performance characteristics of the disk generator using argon gas are studied. At first, the voltage-current curve of the generator using the cesium seeded argon plasma is investigated under typical conditions and the relations between the curve and the average electron density, the current distribution and the other quantities are studied. The influences of the seed fraction and the magnetic flux density on the generator performances are also investigated in detail. Next, the same performance characteristics of the generator using the potassium seeded argon plasma are researched and the differences between the former and the latter performance characteristics are made clear.

In Chapter 8, the performance characteristics of the disk generator using the cesium seeded helium plasma are investigated. The differences between the performances of the generator using the helium and the argon are studied in detail, and it is clarified that the higher output power density and the wider stable region are obtained by the former than the latter. Moreover, the influences of the seed fraction and the magnetic flux density on the generator performances are made clear.

CHAPTER 2

NUMERICAL SOLUTION FOR LINEAR FARADAY GENERATOR

2.1 Introduction

In a nonequilibrium MHD generator channel using alkali metal seeded noble gas plasma as the working fluid, the appearance of the inhomogeneous current distribution based on the ionization instability of the plasma was predicted by the linear perturbation theory by Kerrebrock[18], and it was confirmed by many experiments[9],[10]. And the inhomogeneous current distribution much deteriorates the generator performances. However, as the linear perturbation theory can only distinguish the stability of the plasma and it cannot give any information about the transient formation process and the final steady state of the inhomogeneous current distribution in the channel, there exist many items which cannot be explained by the theory in the experimental evidences. To clarify this inhomogeneous current distribution, the numerical simulation of the plasma with the boundary conditions of the generator channel is most useful.

Therefore, up to now, many researches have been tried to obtain the current distribution in the channel and clarify the experimental results by solving numerically the basic equations governing the working gas plasma[23]-[29]. However, they could not explain sufficiently the experimental results, because most of them did not take into account the time-dependent terms, the convection effect of the plasma, etc.[23]-[27] and others assumed some periodic conditions in one pitch region[28],[29].

Considering the above-mentioned, there are introduced a

two-dimensional time-dependent numerical solution of the small-sized linear Faraday generator with constant rectangular cross section using alkali metal seeded argon plasma, in which the convection effect is taken into account and the periodic conditions in one pitch region are not imposed[33].

First, the channel model of the linear Faraday generator used in the numerical analysis and the basic equations which govern the partially ionized nonequilibrium plasma are introduced. Next, some inevitable assumptions are introduced and the basic equations are transformed into the simplified two-dimensional basic equations to be solved, and also the boundary conditions are presented. And the numerical solution for calculating the electric potential in the channel by applying the finite element method to the above two-dimensional basic equations and the boundary conditions is derived. Finally, the method to compute the current stream function by using the electric potential and the ones to evaluate the electron temperature and the electron density are shown.

2.2 Channel Model

Since one of the purposes of this analysis is to simulate the nonequilibrium MHD generator channel without the periodic conditions, it is desirable to simulate the whole region of the channel. However, as the characteristic length of change of the electrical quantities in the channel are much shorter than the generator size, it is very difficult to simulate the whole region of the channel. On the other hand, it is made clear by experiments[9],[10] that the inhomogeneous current distribution is formed in the inlet region of the channel. Therefore, for the author's analysis, the analytical region is limited to the inlet region of the linear Faraday generator channel with constant rectangular cross section and the channel model as shown in Fig. 2.1 is adopted. In this figure, l, l_i and h are the length of

the inlet region of the channel, the length without electrode and the height of the channel, respectively, c and s the width and the pitch of the electrodes, B, u and R_L explained later and the nozzle is connected at $x = 0$.

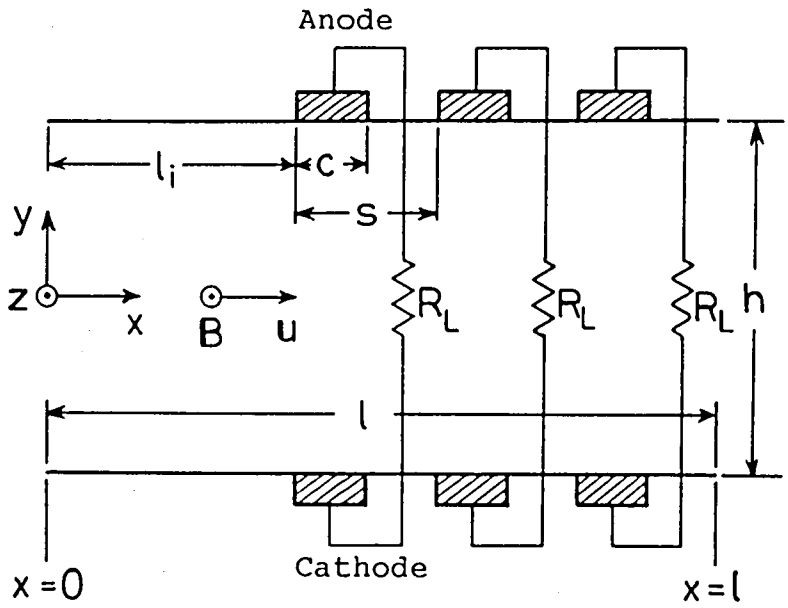

Fig. 2.1 Channel model of linear Faraday generator.

2.3 Basic Equations[29),(33)]

In this analysis, cesium or potassium seeded argon plasma is considered as the working fluid in the generator channel. Usually so far as the stability of the partially ionized nonequilibrium plasma and the qualitative investigation of the performance characteristics of the generator are concerned, it is sufficient to consider that the interactions between the gasdynamic and the electrical quantities are negligible and the distributions of the gasdynamic quantities are constant in time, because the channel size is small and the characteristic length and time of change of the gasdynamic quantities are much longer than those of the

electrical quantities[26],[28]. Moreover, the single ionization of the argon and the seed atom and the so-called three-body recombination among each ion and two electrons are dominant compared with the other processes in the range of the electron temperature used in MHD generator.

Under the above limits, the governing equations of the plasma in the channel become the generalized Ohm's law, the Maxwell's equations, the conservation equations of the argon ions, the seed ions and the electrons and the energy equation of the electrons as follows:

First, the generalized Ohme's law is written as

$$J + \frac{\beta}{B}(J\times B) = \sigma(E^* + \frac{\nabla p_e}{en_e}) \tag{2.1}$$

where

$$\sigma = \frac{e^2 n_e}{m_e \nu_e} \tag{2.2}$$

$$\beta = \frac{eB}{m_e \nu_e} \tag{2.3}$$

$$E^* = E + u\times B \tag{2.4}$$

$$J = en_e(u - u_e) \tag{2.5}$$

$$\nu_e = \nu_a + \nu_s + \nu_{ia} + \nu_{is} \tag{2.6}$$

$$p_e = n_e k T_e \tag{2.7}$$

$$\nu_a = n_a Q_a (\frac{8kT_e}{\pi m_e})^{1/2} \tag{2.8}$$

$$\nu_s = n_s Q_s (\frac{8kT_e}{\pi m_e})^{1/2} \tag{2.9}$$

$$\nu_{ia} = n_{ia} Q_{ia} (\frac{8kT_e}{\pi m_e})^{1/2} \tag{2.10}$$

$$\nu_{is} = n_{is} Q_{is} (\frac{8kT_e}{\pi m_e})^{1/2}. \tag{2.11}$$

In the above equations, J is the current density, u and u_e the heavy particle and the electron drift velocities, E and E^* the electric and the induced electric fields, respectively, T_e the electron temperature, B the magnetic flux density, σ the electrical conductivity, β the Hall parameter for electron, p_e the electron partial pressure, e the charge of the electron and k the Boltzmann constant. Also, m and n the mass and the number density of a particle, respectively, ν the collision frequency, Q the collision cross section and the subscripts e, a, s, ia and is denote electron, argon atom, seed atom, argon ion and seed ion, respectively.

In the author's analysis, Q_a, Q_s, Q_{ia} and Q_{is} are chosen as follows(4),(28),(34):

$$Q_a = 0.28\times10^{-20}(1.46\times10^{-3}\cdot T_e - 0.535) \tag{2.12}$$

$$Q_s = \begin{cases} 0.5\times10^{-17} & \text{(for cesium)} \quad (2.13) \\ 0.4\times10^{-17} & \text{(for potassium)} \quad (2.14) \end{cases}$$

$$Q_{ia} = Q_{is} = 5.85\times10^{-10}\frac{\ln\Lambda}{T_e^2} \tag{2.15}$$

where

$$\Lambda = 1.24\times10^{7}\cdot n_e^{-1/2}T_e^{3/2}. \tag{2.16}$$

The Maxwell's equations are written as

$$\nabla\times E = 0 \tag{2.17}$$

$$\nabla\cdot J = 0. \tag{2.18}$$

The conservation equations of the argon ions, the seed ions and the electrons, in which the single ionization of the argon and the seed atom and the three-body recombination among each ion and two electrons are taken into account, are written as follows:

$$\frac{\partial n_{ia}}{\partial t} + \nabla\cdot(n_{ia}u) = k_{fa}n_e n_a - k_{ra}n_e^2 n_{ia} \tag{2.19}$$

$$\frac{\partial n_{is}}{\partial t} + \nabla \cdot (n_{is}u) = k_{fs}n_e n_s - k_{rs}n_e{}^2 n_{is} \tag{2.20}$$

$$n_e = n_{ia} + n_{is} \tag{2.21}$$

and from the following Saha's equations for thermal ionization

$$\frac{n_e n_{ia}}{n_a} = \frac{2g_{ia}}{g_a}\left(\frac{2\pi m_e kT_e}{h^2}\right)^{3/2}\exp\left(-\frac{\varepsilon_{ia}}{kT_e}\right)$$

$$= 2.9\times 10^{22} T_e^{3/2}\exp\left(-\frac{\varepsilon_{ia}}{kT_e}\right) \tag{2.22}$$

$$\frac{n_e n_{is}}{n_s} = \frac{2g_{is}}{g_s}\left(\frac{2\pi m_e kT_e}{h^2}\right)^{3/2}\exp\left(-\frac{\varepsilon_{is}}{kT_e}\right)$$

$$= 2.42\times 10^{21} T_e{}^{3/2}\exp\left(-\frac{\varepsilon_{is}}{kT_e}\right) \tag{2.23}$$

there exist the following relations between k_{fa} and k_{ra} and between k_{fs} and k_{rs}, respectively

$$k_{fa} = 2.9\times 10^{22} T_e{}^{3/2}\exp\left(-\frac{\varepsilon_{ia}}{kT_e}\right)k_{ra} \tag{2.24}$$

$$k_{fs} = 2.42\times 10^{21} T_e{}^{3/2}\exp\left(-\frac{\varepsilon_{is}}{kT_e}\right)k_{rs}. \tag{2.25}$$

Moreover, in this analysis, k_{ra} and k_{rs} are chosen as follows[20],[35],[36]:

$$k_{ra} = 1.29\times 10^{-44}\left(11.5\frac{e}{kT_e} + 2\right)\exp\left(4.25\frac{e}{kT_e}\right) \tag{2.26}$$

$$k_{rs} = \begin{cases} 2.58\times 10^{-39}\exp\left(1.337\frac{e}{kT_e}\right) & \text{(for cesium)} \quad (2.27) \\ 1.09\times 10^{-20}\cdot T_e{}^{-9/2} & \text{(for potassium).} \quad (2.28) \end{cases}$$

In the above equations, k_{fa} and k_{fs} are the ionization rate coefficients of the argon and the seed, k_{ra} and k_{rs} the recombination rate coefficients of the argon and the seed, ε_{ia} and ε_{is} the ionization potentials of the argon and the seed, h the Planck's constant, g_a, g_s, g_{ia} and g_{is} the statistical weights of the ground state of the argon atom, the seed atom, the argon ion

and the seed ion, respectively.

Finally, the energy equation of electrons is given as

$$\frac{\partial}{\partial t}\{n_{ia}(\frac{3}{2}kT_e + \varepsilon_{ia}) + n_{is}(\frac{3}{2}kT_e + \varepsilon_{is})\}$$

$$+ \nabla \cdot [\{n_{ia}(\frac{3}{2}kT_e + \varepsilon_{ia}) + n_{is}(\frac{3}{2}kT_e + \varepsilon_{is})\}u_e]$$

$$= J \cdot E^* - \nabla \cdot (p_e u_e) - \frac{3}{2}\delta n_e m_e k(T_e - T)$$

$$\times (\frac{\nu_a}{m_a} + \frac{\nu_s}{m_s} + \frac{\nu_{ia}}{m_a} + \frac{\nu_{is}}{m_s}) \qquad (2.29)$$

where T is the temperature of heavy particles except electron and δ is the collision loss factor. As δ takes the value 2 in an elastic collision, it is chosen as 2 in this analysis.

2.4 Assumptions

2.4.1 Gasdynamic quantities and assumptions for them

As mentioned in the preceding section, in the present analysis, it can be assumed that the interactions between the gasdynamic and the electrical quantities are negligible and the distributions of the gasdynamic quantities are constant in time. Therefore, let us use the distributions of the gasdynamic quantities which are obtained by the following quasi-one-dimensional analysis without magnetic field in the steady state.

At first, in the case of no magnetic field in the steady state, the conservation laws of mass, momentum and energy of the working gas fluid are given by the following equations[37]

$$\nabla \cdot (\rho u) = 0 \qquad (2.30)$$

$$\rho u \cdot \nabla u = -\nabla p \qquad (2.31)$$

$$\rho u \cdot \nabla (h + \frac{u^2}{2}) = 0 \qquad (2.32)$$

respectively, where

$$p = \rho RT \tag{2.33}$$

$$h = c_p T. \tag{2.34}$$

In the above equations, ρ is the mass density, h the enthalpy, R the gas constant, c_p the specific heat at constant gas pressure and the friction and the heat transfer losses are not taken into account.

Next, for simplifying the calculation, the following two assumptions are introduced.

(1) Gas velocity u has the following form

$$u = (u, 0, 0). \tag{2.35}$$

(2) All gasdynamic quantities change only in the x direction.

Under the above assumptions, Eqs. (2.30) to (2.32) are reduced into the following quasi-one-dimensional equations.

$$\frac{d}{dx}(\rho u A) = 0 \tag{2.36}$$

$$\rho u \frac{du}{dx} + \frac{dp}{dx} = 0 \tag{2.37}$$

$$\rho u \frac{d}{dx}(h + \frac{u^2}{2}) = 0 \tag{2.38}$$

where A is the cross section.

As the channel has constant cross section, Eq. (2.36) yields

$$\rho u = \text{const.} \tag{2.39}$$

Also by substituting Eq. (2.34) into Eq. (2.38), the following equation is obtained.

$$c_p T + \frac{u^2}{2} = \text{const.} \tag{2.40}$$

By differentiating Eqs. (2.39) and (2.40) with respect to x, the following equations are obtained.

$$\rho \frac{du}{dx} + u \frac{d\rho}{dx} = 0 \tag{2.41}$$

$$c_p\frac{dT}{dx} + u\frac{du}{dx} = 0 \tag{2.42}$$

By substituting Eqs. (2.33), (2.41) and (2.42), Eq. (2.37) is transformed into the following form.

$$\frac{\rho u}{\gamma}(1 - \frac{1}{M^2})\frac{du}{dx} = 0 \tag{2.43}$$

where

$$\gamma = \frac{c_p}{c_v} = \frac{c_p}{c_p - R} \tag{2.44}$$

$$M^2 = \frac{u^2}{\gamma RT} \tag{2.45}$$

In the above equations, c_v is the specific heat for constant volume, γ the specific heat ratio and M the Mach number.

Eq. (2.43) tells that the velocity u is constant all over the channel except the case $M = 1$. Therefore, the velocity of the heavy particles can be assumed to be constant all over the channel and have only x component u. Moreover, considering Eqs. (2.41) and (2.42), all the gasdynamic quantities take the constant values all over the channel in this analysis.

2.4.2 Other assumptions[28]

To simplify the basic equations and obtain the two-dimensional basic equations, the following assumptions are also introduced.

(1) The magnetic flux density B is constant in space and time and has the form

$$B = (0, 0, B). \tag{2.46}$$

(2) All quantities are constant in the z direction, namely

$$\frac{\partial}{\partial z} = 0. \tag{2.47}$$

(3) The term $\nabla p_e/en_e$ in the generalized Ohm's law is negligible.

(4) All terms containing space derivatives in the energy equation (2.29) are negligible.

2.5 Simplified Two-Dimensional Basic Equations

Considering the assumptions introduced in Section 2.4, Eq. (2.1) is reduced to

$$J_x = \frac{\sigma}{1 + \beta^2}\{E_x - \beta(E_y - uB)\} \tag{2.48}$$

$$J_y = \frac{\sigma}{1 + \beta^2}\{\beta E_x + (E_y - uB)\} \tag{2.49}$$

and Eqs. (2.17) and (2.18) are reduced to

$$\frac{\partial E_y}{\partial x} - \frac{\partial E_x}{\partial y} = 0 \tag{2.50}$$

$$\frac{\partial J_x}{\partial x} + \frac{\partial J_y}{\partial y} = 0 \tag{2.51}$$

where the suffixes x and y show the x and y components, respectively, of each vector. Also to decrease the number of unknown variables, the electric potential φ defined by

$$E_x = -\frac{\partial \varphi}{\partial x}, \qquad E_y = -\frac{\partial \varphi}{\partial y} \tag{2.52}$$

is introduced. Eq. (2.50) is satisfied always by Eq. (2.52) and by using Eqs. (2.48), (2.49) and (2.52), Eq.(2.51) is transformed into the following two-dimensional equation for φ

$$\frac{\partial}{\partial x}\{\frac{\sigma}{1 + \beta^2}(-\frac{\partial \varphi}{\partial x} + \beta\frac{\partial \varphi}{\partial y} + \beta uB)\}$$

$$+ \frac{\partial}{\partial y}\{\frac{\sigma}{1 + \beta^2}(-\beta\frac{\partial \varphi}{\partial x} - \frac{\partial \varphi}{\partial y} - uB)\} = 0. \tag{2.53}$$

Next, using the assumption mentioned in Subsection 2.4.1, Eqs. (2.19) and (2.20) are reduced to

$$\frac{\partial n_{ia}}{\partial t} = \dot{n}_{ia} - u\frac{\partial n_{ia}}{\partial x} \tag{2.54}$$

$$\frac{\partial n_{is}}{\partial t} = \dot{n}_{is} - u\frac{\partial n_{is}}{\partial x} \tag{2.55}$$

where $\dot{n}_{ia}$ and $\dot{n}_{is}$ are defined as follows:

$$\dot{n}_{ia} = k_{fa} n_e n_a - k_{ra} n_e^2 n_{ia} \tag{2.56}$$

$$\dot{n}_{is} = k_{fs} n_e n_s - k_{rs} n_e^2 n_{is}. \tag{2.57}$$

By using Eqs. (2.5) and (2.7), Eq. (2.29) becomes

$$\begin{aligned}
&\frac{3}{2}kn_e\frac{\partial T_e}{\partial t} + (\frac{3}{2}kT_e + \varepsilon_{ia})\{\frac{\partial n_{ia}}{\partial t} + \nabla\cdot(n_{ia}u)\} \\
&\quad + (\frac{3}{2}kT_e + \varepsilon_{is})\{\frac{\partial n_{is}}{\partial t} + \nabla\cdot(n_{is}u)\} \\
&\quad - (\frac{3}{2}kT_e + \varepsilon_{ia})\nabla\cdot(\frac{n_{ia}}{en_e}J) - (\frac{3}{2}kT_e + \varepsilon_{is})\nabla\cdot(\frac{n_{is}}{en_e}J) \\
&\quad + \frac{5}{2}kn_e(u - \frac{J}{en_e})\cdot\nabla T_e + kT_e\nabla\cdot(n_e u - \frac{J}{e}) \\
&\quad = J\cdot E^* - \frac{3}{2}\delta n_e m_e k(T_e - T)(\frac{\nu_a}{m_a} + \frac{\nu_s}{m_s} + \frac{\nu_{ia}}{m_a} + \frac{\nu_{is}}{m_s}).
\end{aligned} \tag{2.58}$$

Substituting Eqs. (2.18), (2.48), (2.49), (2.54) and (2.55) into Eq. (2.58), it is transformed into the following form

$$\begin{aligned}
&\frac{3}{2}kn_e\frac{\partial T_e}{\partial t} + (\frac{3}{2}kT_e + \varepsilon_{ia})\dot{n}_{ia} + (\frac{3}{2}kT_e + \varepsilon_{is})\dot{n}_{is} \\
&\quad - \frac{\varepsilon_{ia}}{e}J\cdot\nabla(\frac{n_{ia}}{n_e}) - \frac{\varepsilon_{is}}{e}J\cdot\nabla(\frac{n_{is}}{n_e}) \\
&\quad + \frac{5}{2}k(n_e u - \frac{J}{e})\cdot\nabla T_e + kT_e\nabla\cdot(n_e u) \\
&\quad = \frac{J_x^2 + J_y^2}{\sigma} - \frac{3}{2}\delta n_e m_e k(T_e - T) \\
&\qquad \times(\frac{\nu_a}{m_a} + \frac{\nu_s}{m_s} + \frac{\nu_{ia}}{m_a} + \frac{\nu_{is}}{m_s}).
\end{aligned} \tag{2.59}$$

Therefore, considering the above assumption (4), the energy equation of electrons becomes as follows:

$$\begin{aligned}
\frac{\partial T_e}{\partial t} &= \frac{2}{3kn_e}\frac{J_x^2 + J_y^2}{\sigma} - \delta m_e(T_e - T)(\frac{\nu_a}{m_a} + \frac{\nu_s}{m_s} + \frac{\nu_{ia}}{m_a} + \frac{\nu_{is}}{m_s}) \\
&\quad - (T_e + \frac{2\varepsilon_{ia}}{3k})\frac{\dot{n}_{ia}}{n_e} - (T_e + \frac{2\varepsilon_{is}}{3k})\frac{\dot{n}_{is}}{n_e}.
\end{aligned} \tag{2.60}$$

Lastly, Eqs. (2.21),(2.48),(2.49),(2.52) to (2.55) and (2.60) are the basic equations to be solved.

2.6 Boundary Conditions

In order to solve the above two-dimensional basic equations Eqs. (2.21),(2.48),(2.49),(2.52) to (2.55) and (2.60), some boundary conditions are necessary.

First, the following electrical boundary condition is adopted on each electrode surface

$$\varphi = \text{const.} \tag{2.61}$$

and for each electrode pair, there exists the following relations between the electric potentials of the anode φ_a and the cathode φ_c

$$\varphi_c - \varphi_a = R_L I_L \tag{2.62}$$

$$I_L = -w\int_{anode} J_y dx = -w\int_{cathode} J_y dx \tag{2.63}$$

where w is the channel width and I_L, R_L are the load current and the load resistance, respectively.

Also the following electrical boundary condition is used on each insulator wall surface

$$J_y = 0. \tag{2.64}$$

Next, as a nozzle is connected at $x = 0$ in Fig. 2.1, it can be assumed that current density for $x < 0$ is equal to zero. Therefore, the boundary condition at $x = 0$ is assumed as follows:

$$J_x = 0. \tag{2.65}$$

At last, the boundary condition at $x = l$ is mentioned. Because one of the purposes of this analysis is to obtain the current distribution in the channel without the periodic conditions in one pitch region, these conditions can not be used as the boundary condition at $x = l$. Therefore, another boundary condition must be

adopted. But this condition is unknown. Considering the above fact, in this analysis, it is assumed as follows:

$$J_x = 0. \tag{2.66}$$

The validity of this condition is checked in the next chapter.

2.7 Numerical Solution of Two-Dimensional Basic Equations

2.7.1 Calculation of electric potential[28]

In this analysis, the finite element method is applied to obtain the electric potential φ by solving the partial differential equation (2.53) under the boundary conditions of Eqs. (2.61) to (2.66).

At first, in order to solve Eq. (2.53) by the finite element method, the analytical region is divided into many small finite elements. Here let us use the rectangular bilinear element, which has the widths Δx in x-direction and Δy in y-direction, as shown in Fig. 2.2. Then, the potential $\varphi = \varphi(x,y)$ at any point P = P(x,y) in

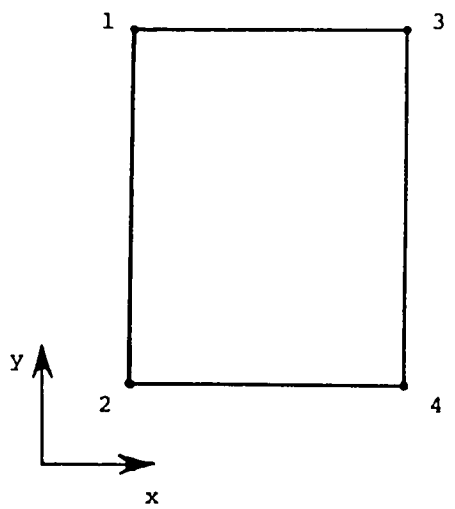

Fig. 2.2 Rectangular element.

this element is given by φ_1, φ_2, φ_3 and φ_4 , which are the values of φ's at the nodes $1 = 1(x_2, y_1)$, $2 = 2(x_2, y_2)$, $3 = 3(x_1, y_1)$ and $4 = 4(x_1, y_2)$ in Fig. 2.2, as follows:

$$\varphi(x,y) = \{N(x,y)\}^T \{\varphi^e\} \tag{2.67}$$

where

$$\{N(x,y)\} = \{N_1(x,y)\ N_2(x,y)\ N_3(x,y)\ N_4(x,y)\}^T$$

$$= \frac{1}{S_e}\begin{Bmatrix} -(x - x_1)(y - y_2) \\ (x - x_1)(y - y_1) \\ (x - x_2)(y - y_2) \\ -(x - x_2)(y - y_1) \end{Bmatrix} \tag{2.68}$$

$$S_e = (x_1 - x_2)(y_1 - y_2) = \Delta x \Delta y \tag{2.69}$$

and

$$\{\varphi^e\} = \{\varphi_1\ \varphi_2\ \varphi_3\ \varphi_4\}^T \tag{2.70}$$

in which $N_1(x,y)$ to $N_4(x,y)$ are the so-called interpolation functions at the nodes 1 to 4, respectively.

In this analysis, the Galerkin process is used because Eq. (2.53) does not have the functional[28]. So it is assumed that for a node i which is contained in the analytical region, the weighted integral of Eq. (2.53) with the weight $N_i(x,y)$, which is the summation of the interpolation functions correspond to the node i, over the analytical region S takes the value 0. Namely, the following equation is established.

$$\iint_S N_i \left[\frac{\partial}{\partial x} \left\{ \frac{\sigma}{1 + \beta^2} \left(-\frac{\partial \varphi}{\partial x} + \beta \frac{\partial \varphi}{\partial y} + \beta u B \right) \right\} \right.$$

$$\left. + \frac{\partial}{\partial y} \left\{ \frac{\sigma}{1 + \beta^2} \left(-\beta \frac{\partial \varphi}{\partial x} - \frac{\partial \varphi}{\partial y} - u B \right) \right\} \right] dxdy = 0 \tag{2.71}$$

Applying the integration by parts to the above equation, it is transformed into the following form

$$\iint_S \{\frac{\sigma}{1+\beta^2}\frac{\partial N_i}{\partial x}(-\frac{\partial \varphi}{\partial x}+\beta\frac{\partial \varphi}{\partial y}+\beta uB)$$

$$+\frac{\sigma}{1+\beta^2}\frac{\partial N_i}{\partial y}(-\beta\frac{\partial \varphi}{\partial x}-\frac{\partial \varphi}{\partial y}-uB)\}\,dxdy$$

$$-\iint_S [\frac{\partial}{\partial x}\{\frac{\sigma}{1+\beta^2}N_i(-\frac{\partial \varphi}{\partial x}+\beta\frac{\partial \varphi}{\partial y}+\beta uB)\}$$

$$+\frac{\partial}{\partial y}\{\frac{\sigma}{1+\beta^2}N_i(-\beta\frac{\partial \varphi}{\partial x}-\frac{\partial \varphi}{\partial y}-uB)\}]dxdy = 0 \qquad (2.72)$$

Furthermore, applying the Gauss' theorem to Eq. (2.72), it becomes

$$\iint_S \{\frac{\sigma}{1+\beta^2}\frac{\partial N_i}{\partial x}(-\frac{\partial \varphi}{\partial x}+\beta\frac{\partial \varphi}{\partial y}+\beta uB)$$

$$+\frac{\sigma}{1+\beta^2}\frac{\partial N_i}{\partial y}(-\beta\frac{\partial \varphi}{\partial x}-\frac{\partial \varphi}{\partial y}-uB)\}\,dxdy$$

$$-\oint_C (N_i J_y dx + N_i J_x dy) = 0 \qquad (2.73)$$

where C is the contour of the analytical region S. By setting up the above equation for all nodes in S and dividing into each element, the following equation is obtained

$$\sum_e [\iint_{S^e} \{\frac{\sigma}{1+\beta^2}\frac{\partial N_j}{\partial x}(-\frac{\partial \varphi}{\partial x}+\beta\frac{\partial \varphi}{\partial y}+\beta uB)$$

$$+\frac{\sigma}{1+\beta^2}\frac{\partial N_j}{\partial y}(-\beta\frac{\partial \varphi}{\partial x}-\frac{\partial \varphi}{\partial y}-uB)\}\,dxdy$$

$$-\oint_{C^e} (N_j J_y dx + N_j J_x dy)] = 0, \qquad j = 1 \text{ to } 4 \qquad (2.74)$$

in which S^e is the region of an element, C^e the contour of S^e and $\sum_e$ means the summation with respect to all the elements. By using Eq. (2.67) and representing N_j (j = 1 to 4) as $\{N\}$, Eq. (2.74) becomes

$$\sum_e (-\iint_{S^e} \frac{\sigma}{1+\beta^2} [\{N_x\}\{N_x\}^T + \{N_y\}\{N_y\}^T$$

$$- \beta\{N_x\}\{N_y\}^T + \beta\{N_y\}\{N_x\}^T] dxdy \cdot \{\varphi^e\}$$

$$+ \iint_{S^e} \frac{\sigma}{1+\beta^2} uB[\beta\{N_x\} - \{N_y\}] dxdy$$

$$- \oint_{C^e} [\{N\} J_y dx + \{N\} J_x dy]) = 0 \qquad (2.75)$$

where $\{N_x\}$, $\{N_y\}$ represent

$$\{N_x\} = \{\frac{\partial N}{\partial x}\} = \frac{1}{S_e}\begin{Bmatrix} -(y - y_2) \\ (y - y_1) \\ (y - y_2) \\ -(y - y_1) \end{Bmatrix} \qquad (2.76)$$

$$\{N_y\} = \{\frac{\partial N}{\partial y}\} = \frac{1}{S_e}\begin{Bmatrix} -(x - x_1) \\ (x - x_1) \\ (x - x_2) \\ -(x - x_2) \end{Bmatrix} \qquad (2.77)$$

respectively.

From Eq. (2.75), the following set of the simultaneous equations can be derived

$$\sum_e ([K^e]\{\varphi^e\} - \{F_1^e\} - \{F_2^e\}) = 0 \qquad (2.78)$$

where

$$[K^e] = -\iint_{S^e} \frac{\sigma}{1+\beta^2} [\{N_x\}\{N_x\}^T + \{N_y\}\{N_y\}^T$$

$$- \beta\{N_x\}\{N_y\}^T + \beta\{N_y\}\{N_x\}^T] dxdy \qquad (2.79)$$

$$\{F_1^e\} = -\iint_{S^e} \frac{\sigma}{1+\beta^2} uB[\beta\{N_x\} - \{N_y\}] dxdy \qquad (2.80)$$

$$\{F_2^e\} = \oint_{C^e} (\{N\} J_y dx + \{N\} J_x dy). \qquad (2.81)$$

Accordingly, by solving the above set of the simultaneous equations, the electric potential φ at every node is obtained.

In this analysis, the dimensions of an element is chosen as Δx = 0.25 mm, Δy = 4 mm and Eq. (2.78) is solved by Gaussian elimination.

2.7.2 Calculation of ion and electron densities[28]

The argon and the seed ion densities n_{ia} and n_{is} and the electron density n_e are calculated by solving Eqs. (2.21), (2.54) and (2.55). In most of the past analyses, the terms containing space derivatives in Eqs. (2.54) and (2.55) are assumed to be negligible. Since this assumption means that the convection effect of the working plasma is negligible, it is not suitable for this analysis. Accordingly, the following method is adopted for it. On the characteristic curves given by the following equations

$$\frac{dx}{dt} = u \tag{2.82}$$

$$\frac{dy}{dt} = 0 \tag{2.83}$$

the Eqs. (2.54) and (2.55) take the following forms

$$\frac{dn_{ia}}{dt} = \dot{n}_{ia} \tag{2.84}$$

$$\frac{dn_{is}}{dt} = \dot{n}_{is} \tag{2.85}$$

respectively. And these equations can be numerically solved by the Runge-Kutta method.

2.7.3 Calculation of electron temperature

The electron temperature T_e is obtained by Eq. (2.60). As the relaxation of electron temperature can be assumed to be instantaneous compared to the relaxation of electron density, the instantaneous temperature relaxation can be assumed[28]. Then Eq. (2.60) is reduced to the following form

$$\frac{2}{3kn_e}\frac{J_x^2 + J_y^2}{\sigma} - \delta m_e(T_e - T)\left(\frac{\nu_a}{m_a} + \frac{\nu_s}{m_s} + \frac{\nu_{ia}}{m_a} + \frac{\nu_{is}}{m_s}\right)$$

$$-\left(T_e + \frac{2\varepsilon_{ia}}{3k}\right)\frac{\dot{n}_{ia}}{n_e} - \left(T_e + \frac{2\varepsilon_{is}}{3k}\right)\frac{\dot{n}_{is}}{n_e} = 0. \tag{2.86}$$

From this equation the electron temperature T_e can be calculated by using the Newton-Raphson method. In this method, T_e is obtained by converging the following iteration

$$T_e^{n+1} = T_e^n - \frac{f(T_e^n)}{f'(T_e^n)} \tag{2.87}$$

where

$$f(T_e) = \frac{2}{3kn_e}\frac{J_x^2 + J_y^2}{\sigma} - \delta m_e(T_e - T)\left(\frac{\nu_a}{m_a} + \frac{\nu_s}{m_s} + \frac{\nu_{ia}}{m_a} + \frac{\nu_{is}}{m_s}\right)$$

$$-\left(T_e + \frac{2\varepsilon_{ia}}{3k}\right)\frac{\dot{n}_{ia}}{n_e} - \left(T_e + \frac{2\varepsilon_{is}}{3k}\right)\frac{\dot{n}_{is}}{n_e} \tag{2.88}$$

$$f'(T_e) = \frac{df(T_e)}{dT_e} \tag{2.89}$$

and T_e^n is the approximate value of T_e obtained by n-th iteration.

Because of this simplification, the time step Δt for the Runge-Kutta method must be chosen appropriately between the relaxation times of the electron temperature and the electron density. In this analysis, considering the above requirement, $\Delta t = 0.255\ \mu s$ is selected[28].

2.7.4 Calculation of current stream function

To study the current distribution in the channel, the current stream function Ψ is useful. In this analysis, considering the channel width w, it is defined as

$$J_x = \frac{1}{w}\frac{\partial \Psi}{\partial y} \tag{2.90}$$

$$J_y = -\frac{1}{w}\frac{\partial \Psi}{\partial x} \tag{2.91}$$

which satisfy Eq. (2.51). By integrating Eqs. (2.90) and (2.91) Ψ can be obtained.

2.7.5 Flow chart

At last, the flow chart of the calculation by using the numerical solutions mentioned in this section is shown in Fig. 2.3. The calculation processes are as follows:

(1) The channel size, the load resistance, the magnetic flux density, the gasdynamic conditions and the initial value of electron density are provided.

(2) The conductivity σ and the Hall parameter β in each element are calculated by Eqs. (2.2) and (2.3).

(3) By using the finite element method, the electric potential φ on each node is calculated.

(4) The electric fields E_x and E_y in each element is calculated by Eq. (2.52).

(5) The current densities J_x and J_y in each element is calculated by Eqs. (2.48) and (2.49).

(6) By using Newton-Raphson method, the electron temperature T_e in each element is calculated by Eq. (2.86).

(7) The processes (2) to (6) are iterated till T_e in all elements are converged.

(8) The current stream function Ψ on each node is calculated by Eqs. (2.90) and (2.91).

(9) By Runge-Kutta method, the electron density n_e in each element at the next time step $t = t + \Delta t$ is calculated by Eqs. (2.21), (2.84) and (2.85).

(10) The processes (2) to (9) are iterated till $t = t_{max}$, where t_{max} is the calculation interval needed to investigate the transient response of the current distribution in the channel.

2.8 Concluding Remarks

The main conclusions obtained in this chapter are as follows:

(1) A two-dimensional model of the linear Faraday generator

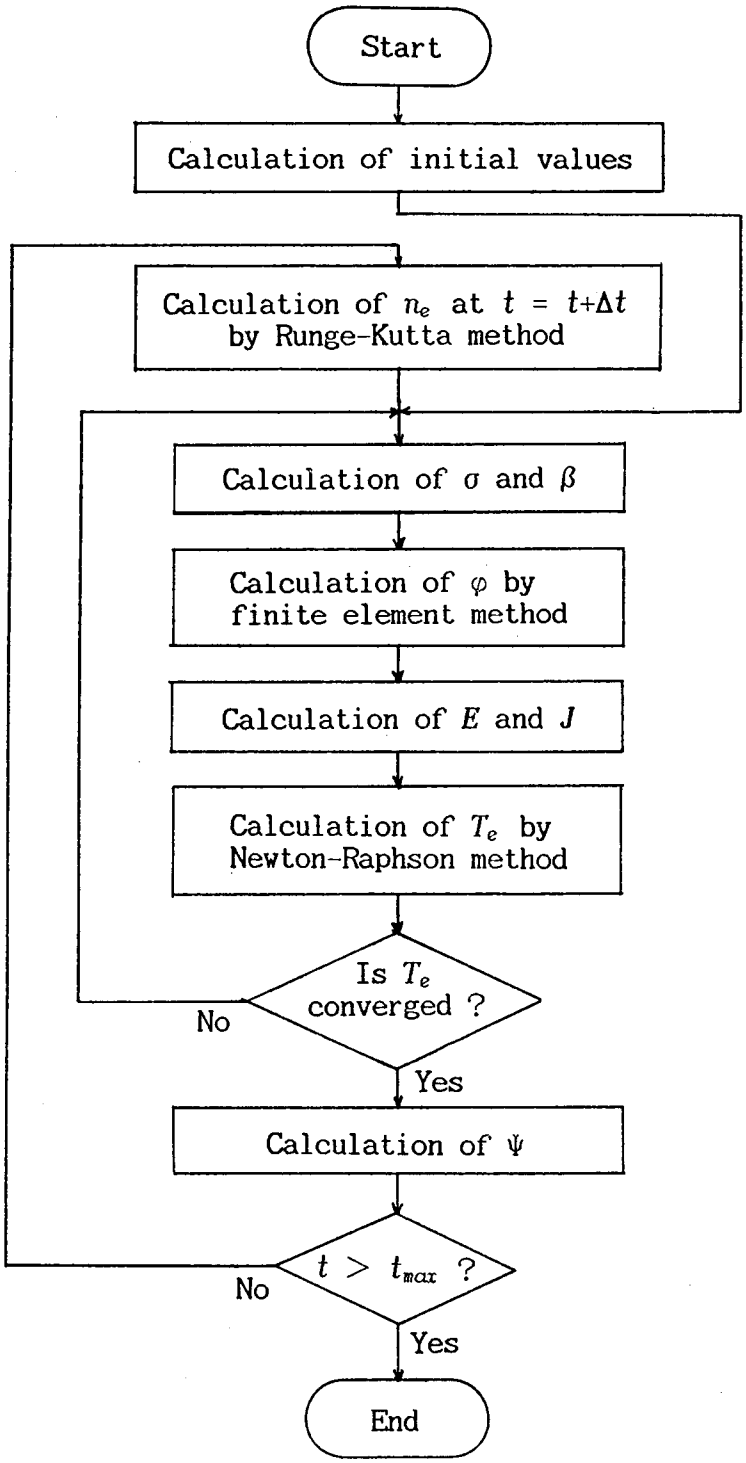

Fig. 2.3 Flow chart of calculation processes.

channel without the periodic conditions in one pitch region was introduced.

(2) Using some inevitable assumptions, the two-dimensional basic equations, by which the electric potential, the electron temperature and the electron density in the channel can be numerically calculated, were derived from the basic equations.

(3) To calculate the electric potential on each node, the numerical solution was introduced, which is obtained by applying the finite element method to the above two-dimensional basic equations and boundary conditions.

(4) The methods to calculate the electron temperature, the electron density and the current stream function were shown.

(5) The flow chart for solving the above two-dimensional basic equations was shown.

CHAPTER 3

INFLUENCES OF VARIOUS FACTORS ON CURRENT DISTRIBUTION IN LINEAR FARADAY GENERATOR

3.1 Introduction

As mentioned in the preceding two chapters, up to now, many researchers have tried to obtain the current distribution in the channel and clarify the experimental results by solving numerically the differential equations governing the working gas plasma. However, they could not explain the transient formation process and the steady state of the current distribution which are observed in the experiments. Considering those, the author derived a new two-dimensional time-dependent numerical solution for the linear Faraday generator in the preceding chapter. In this chapter, by applying this numerical method to the models of the linear generator in which the cesium seeded argon plasma is used as the working fluid, there are studied in detail on the inhomogeneous current distribution in the one[33),(38)-(40)].

In this chapter, at first, the transient formation process and the steady state of the inhomogeneous current distributions are made clear, and it is shown that those calculated distributions are in good agreement with the experimental results. Next, the influences of the electrode configuration and the convection effect of the plasma on the current distribution are investigated, and it is clarified that the main factors which govern the transient and steady current distributions are the ionization instability and the convection effect of the plasma.

3.2 Numerical Conditions

The numerical analyses in this and the next chapters are carried out for the three kinds of Faraday generator models of Types 1, 2 and 3, whose whole length l, height h, width w, length with no electrode l_i, electrode pitch and width s and c, and electrode number n_{ele} are shown in Table 3.1. In the table, also there are shown the values of the stagnation and static temperatures of the gas T_s and T, the stagnation and static pressures p_s and p, the Mach number M, the gas velocity u, the argon number density n_{a0}, the magnetic flux density B, the seed fraction ε, the load resistance R_L, the dimensions of an element Δx and Δy, and the time step Δt used in the analyses. In this connection, Fig. 3.1 shows the relations of the electron density n_e to the electron temperature T_e obtained by using Saha's equations for thermal ionization (2.22) and (2.23) for various seed fractions ε.

3.3 Validity of Boundary Condition

In this chapter, at first, let us check the validity of the boundary condition at $x = l$ introduced in the preceding chapter. For this purpose, it is thought a good way to perform numerical simulations on two channel models, which are the inlet region of a same channel and have different lengths of the analytical regions, and to compare the calculated results. So in the numerical calculations, the author chooses two channel models of Types 1 and 2 shown in Table 3.1, where $B = 3$ T, $\varepsilon = 2 \times 10^{-4}$ and $R_L = 1\ \Omega$ are adopted. As the initial condition, the author assumes that the load resistances are connected to each pair of the anode and the cathode at $t = 0$.

Figure 3.2 shows the current distributions in Types 1 and 2 channels at $t = 163.2\ \mu$s, which corresponds to the 640th step. In the figure, the contour interval between neighboring current

Table 3.1 Numerical conditions used in calculations.

		Type 1	Type 2	Type 3
Length of channel model	l	120 mm	200 mm	120 mm
Channel height	h	40 mm	40 mm	40 mm
Channel width	w	40 mm	40 mm	40 mm
Length with no electrode	l_i	40 mm	40 mm	40 mm
Electrode pitch	s	5 mm	5 mm	10 mm
Electrode width	c	2.5 mm	2.5 mm	5 mm
Number of electrodes	n_{ele}	16	32	8
Stagnation temperature	T_s	2000 K		
Static temperature	T	1079 K		
Stagnation pressure	p_s	5.6 atm		
Static pressure	p	1.2 atm		
Mach number	M	1.6		
Gas velocity	u	980 m/s		
Argon number density	n_{a0}	8.16×10^{24} m^{-3}		
Magnetic flux density	B	4 T, 3 T, 2 T, 1 T		
Seed fraction	ε	2×10^{-4}, 5×10^{-5}, 10^{-5}		
Load resistance	R_L	20 Ω, 4 Ω, 1 Ω, 0.5 Ω, 0.2 Ω		
Dimension of element	Δx	0.25 mm		
Dimension of element	Δy	4 mm		
Time step	Δt	0.255 μs		

streamlines $\Delta\Psi$ = 5 A. The figures tell that the current distributions in the region which is included to both channel models are almost same. Namely, the boundary condition of Eq. (2.66) at $x = l$ introduced in the preceding chapter has scarcely influence on the simulation results except only near this boundary. Accordingly, it can be said that the boundary condition is sufficiently valid.

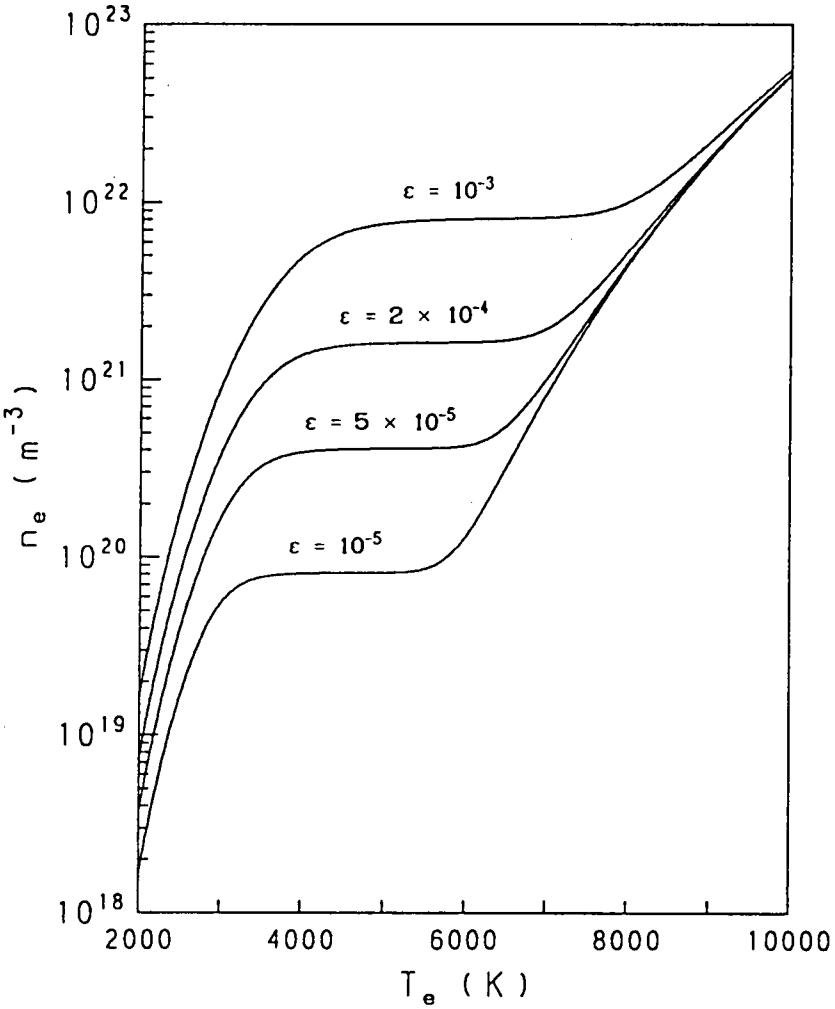

Fig. 3.1 Relations between electron temperature and electron density obtained by Saha's equations for various seed fractions.

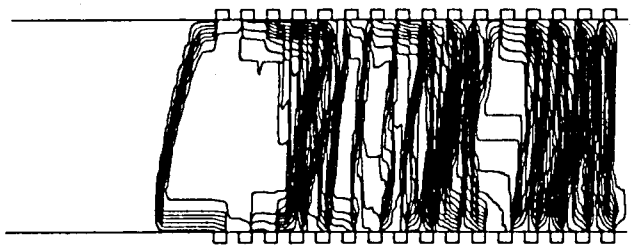

Type 1 channel

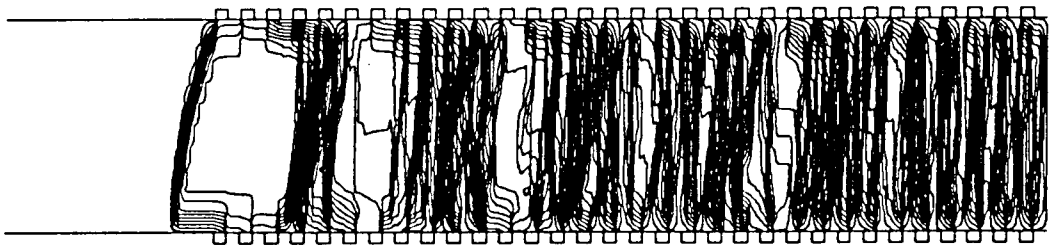

Type 2 channel

Fig. 3.2 Dependence of current distributions on length of channel model used in calculation.

3.4 Transient Formation Process and Steady State of Inhomogeneous Current Distribution

In this section, the transient formation process and the steady state of the inhomogeneous current distribution in nonequilibrium ionization plasma generator channel are made clear. For this purpose, the numerical analysis is performed under the conditions which are usually used in the experiments[41]. In this analysis, the channel of Type 1 in Table 3.1 is chosen, where the magnetic flux density B = 3 T, the seed fraction $\varepsilon = 2 \times 10^{-4}$ and the load resistance R_L = 4 Ω are adopted.

Figures 3.3(a) to (c) show the transient current distributions in the channel at t = 0 to t = 76.5 μs(the 300th step) on the same initial condition used in the preceding section. Since the magnetic

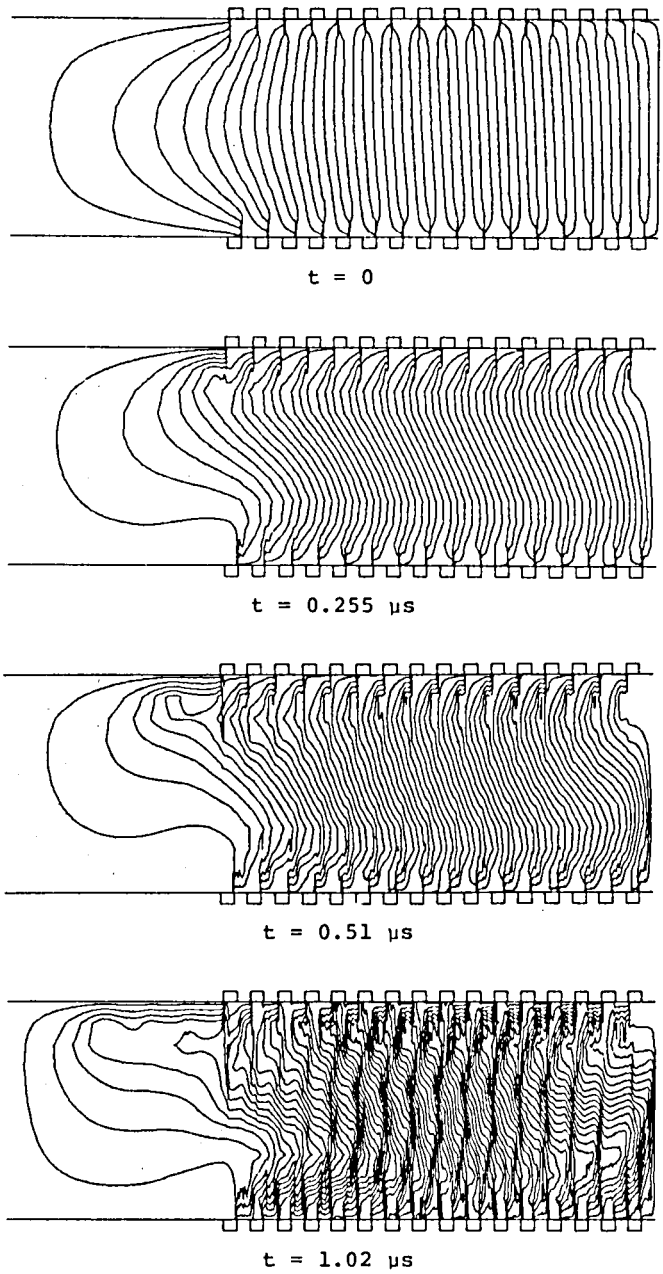

Fig. 3.3(a) Transient current distributions for B = 3 T, $\varepsilon = 2 \times 10^{-4}$ and R_L = 4 Ω ($\Delta\Psi$ = 0.1 A).

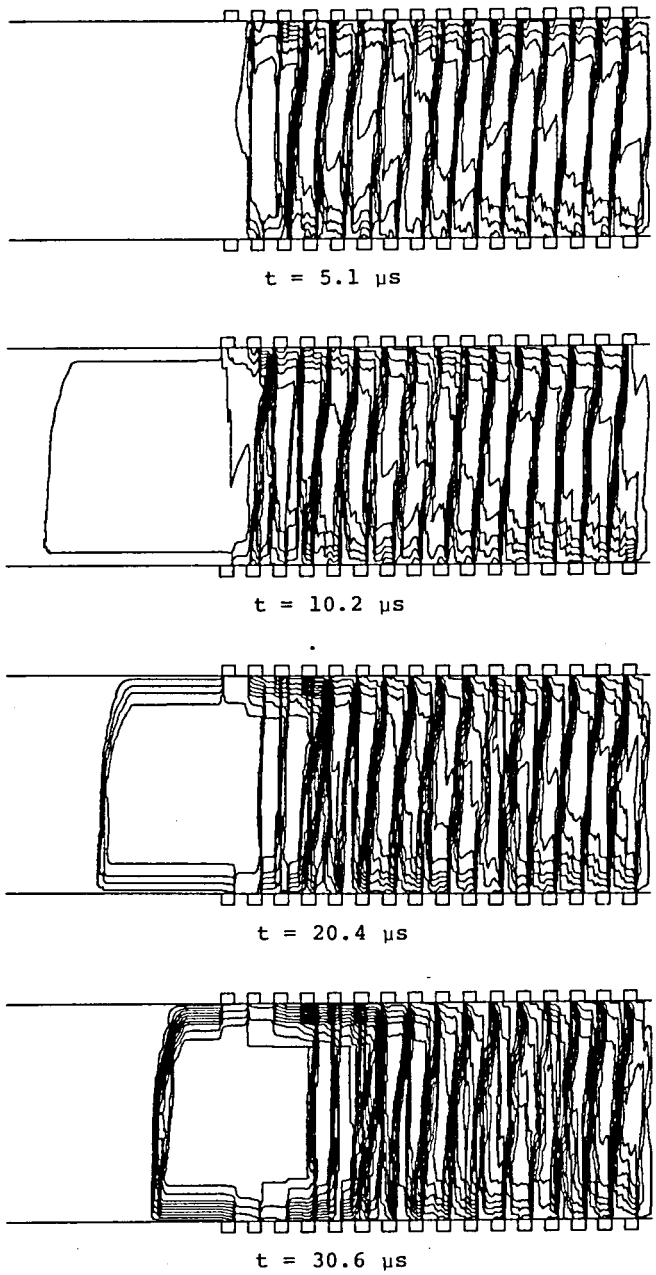

Fig. 3.3(b) Transient current distributions for B = 3 T, $\varepsilon = 2 \times 10^{-4}$ and R_L = 4 Ω ($\Delta\Psi$ = 2 A).

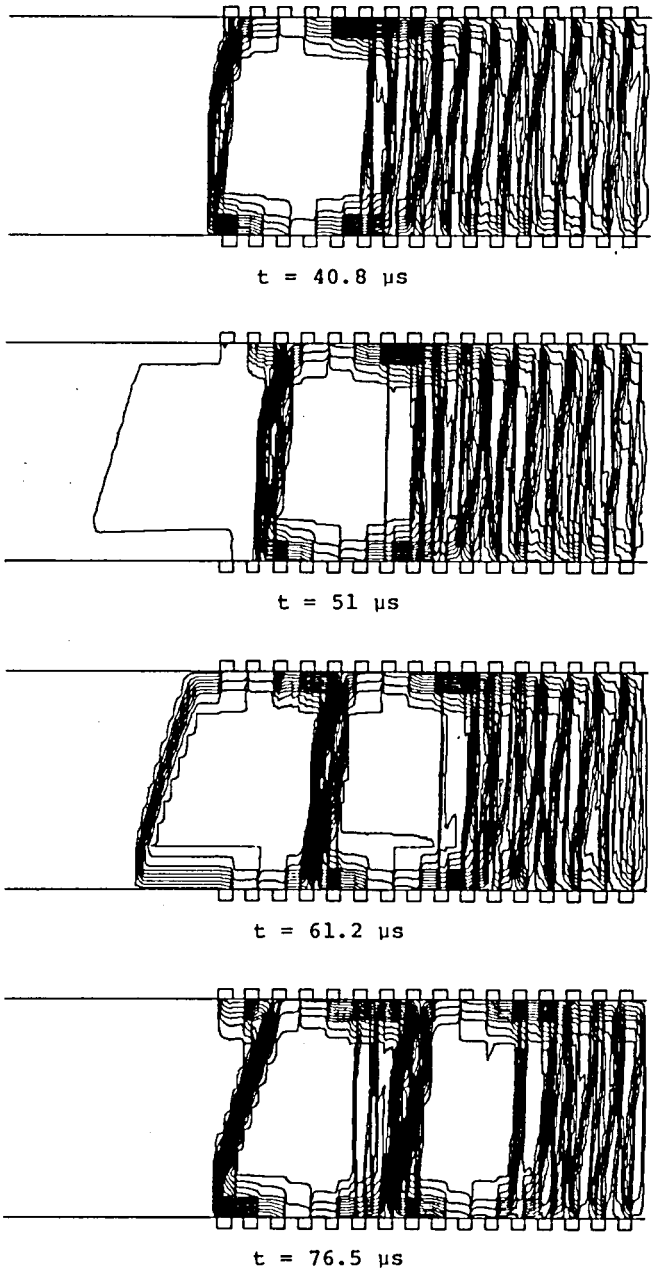

Fig. 3.3(c) Transient current distributions for B = 3 T, $\varepsilon = 2 \times 10^{-4}$ and R_L = 4 Ω ($\Delta\Psi$ = 2 A).

field is applied to the channel, the regions where the current density becomes high appear near each electrode edge at $t = 0$. In these regions, the electron temperature is increased by the Joule heat. This causes the rise of the electron density and so the conductivity of the plasma increases. This leads again to the rise of the current density, and then its inhomogeneity becomes strong.

As time goes on, the high current density regions spread out spatially, and as shown in Figs. 3.3(a) and (b), the regions interconnect the anodes and the cathodes at last. In such a way, strong concentrated current paths interconnecting the anodes and the cathodes, which are usually called streamers, are formed in the channel. Although the origins of the streamers make the angle of about $\pi/4$ from the corresponding current density vectors as seen from the figure at $t = 0.51$ μs in Fig. 3.3(a), their directions are almost same as those of the corresponding current density vectors when they have been formed as seen from Fig. 3.3(b). However, the above process of nonlinear growth of the ionization instability could not be made clear by the linear perturbation theory. As shown in Fig. 3.3(b), the pitch of the streamer is equal to that of the electrode at $t = 5.1$ μs. The formation process of the streamers obtained by this numerical analysis is about same with the results obtained by the simulation in which the periodic conditions in one pitch region were used.

Moreover, Figs. 3.3(b) and (c) tell that by the convection effect of the plasma, the streamers are carried downstream in the channel at the speed equal to that of the working plasma. This speed of streamers is in good agreement with the experimental evidences.

In the above way, the streamers are formed from the electrode edges just after the load resistances are connected to the electrodes. However, The current distributions at $t = 10.2$ and 20.4 μs in Fig. 3.3(b) tell that a next streamer is formed just after the inlet of the channel. Its origin is considered as the

inhomogeneity of the current density there. The streamer is also carried downstream in the channel at the speed equal to that of the working plasma and grows much wider than the one formed just after the load resistances are connected to the electrodes. After this streamer is formed, no streamer is formed from the electrode edges. Instead of it, the next streamers are formed just after the inlet of the channel and these streamers govern the current distribution in the channel.

Figure 3.4 shows the streamer structures which repeatedly produced in the steady state. The figure tells that the streamer structure in the steady state is different from the one just after connecting the load resistances to the electrodes and the pitch of the streamers is not equal to the electrode pitch. Near the inlet of the channel, the streamers have certain inclination from y direction. However, as they flow to downstream, some new fine current paths in the y direction, which connect the anode and the cathode, are overlapped to the core streamers. This makes each streamer be consisted of several fine striated structures. The above results obtained by this simulation, namely, the current distribution in the steady state, the speed of the streamers, etc. are in good agreement with the experimentally observed results[9],[10].

The time-dependent electron temperature T_e and electron density n_e distributions in the x direction on the center line of the channel are shown in Figs. 3.5 and 3.6, respectively. From these figures, it is made clear that both T_e and n_e are high in the streamers. From not only Figs. 3.3(a) to (c) but also Figs. 3.5 and 3.6, it is evident that the streamers are carried downstream in the channel at the speed equal to that of the working plasma.

The figures show that $T_e \fallingdotseq 4000$ K and n_e is of order 10^{21} m^{-3} in the streamers. And Figure 3.1 tells that the plasma of $T_e \fallingdotseq 4000$ K and $n_e \fallingdotseq 10^{21}$ m^{-3} is about in the so-called Saha

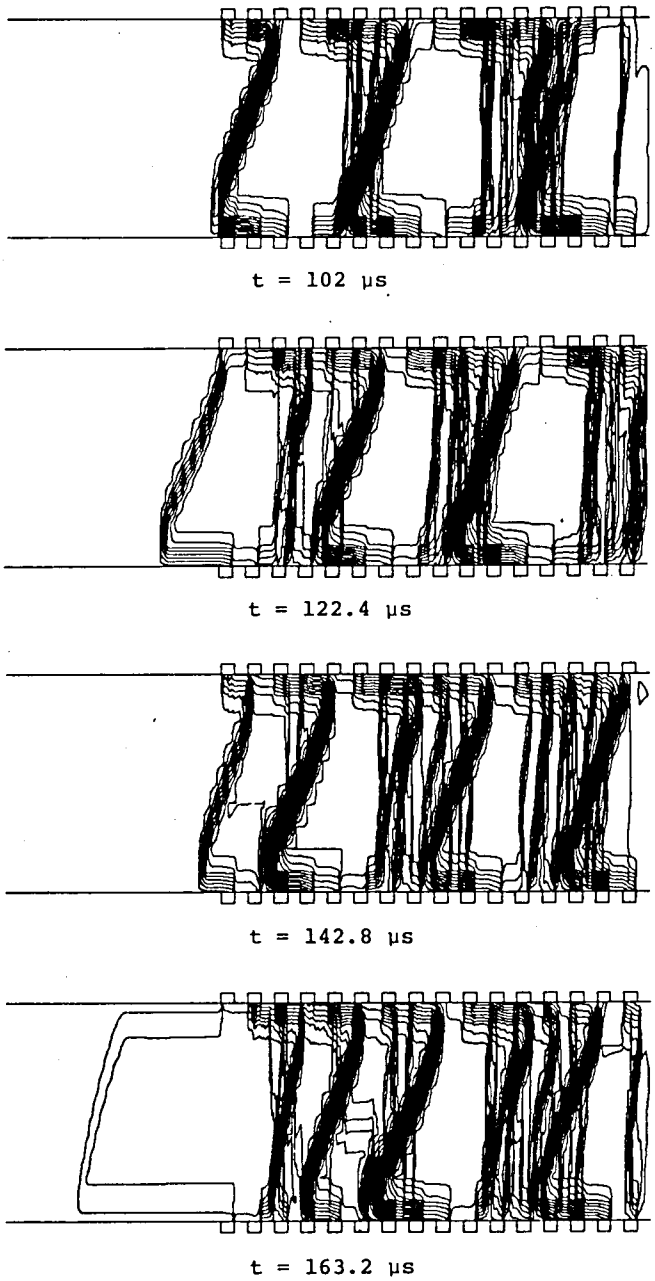

Fig. 3.4 Current distributions for B = 3 T, $\varepsilon = 2 \times 10^{-4}$ and R_L = 4 Ω ($\Delta\Psi$ = 2 A).

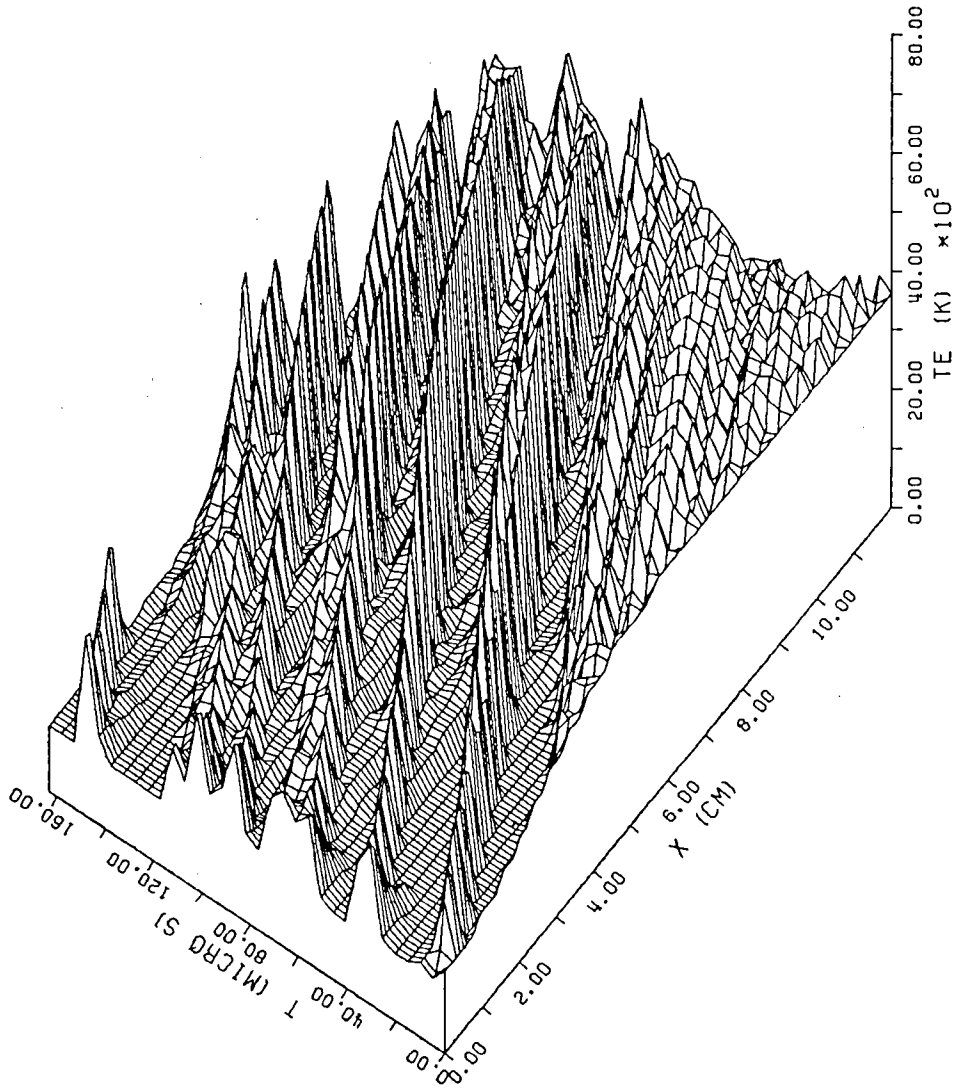

Fig. 3.5 Time-dependent electron temperature distribution in x direction for B = 3 T, $\varepsilon = 2 \times 10^{-4}$ and R_L = 4 Ω.

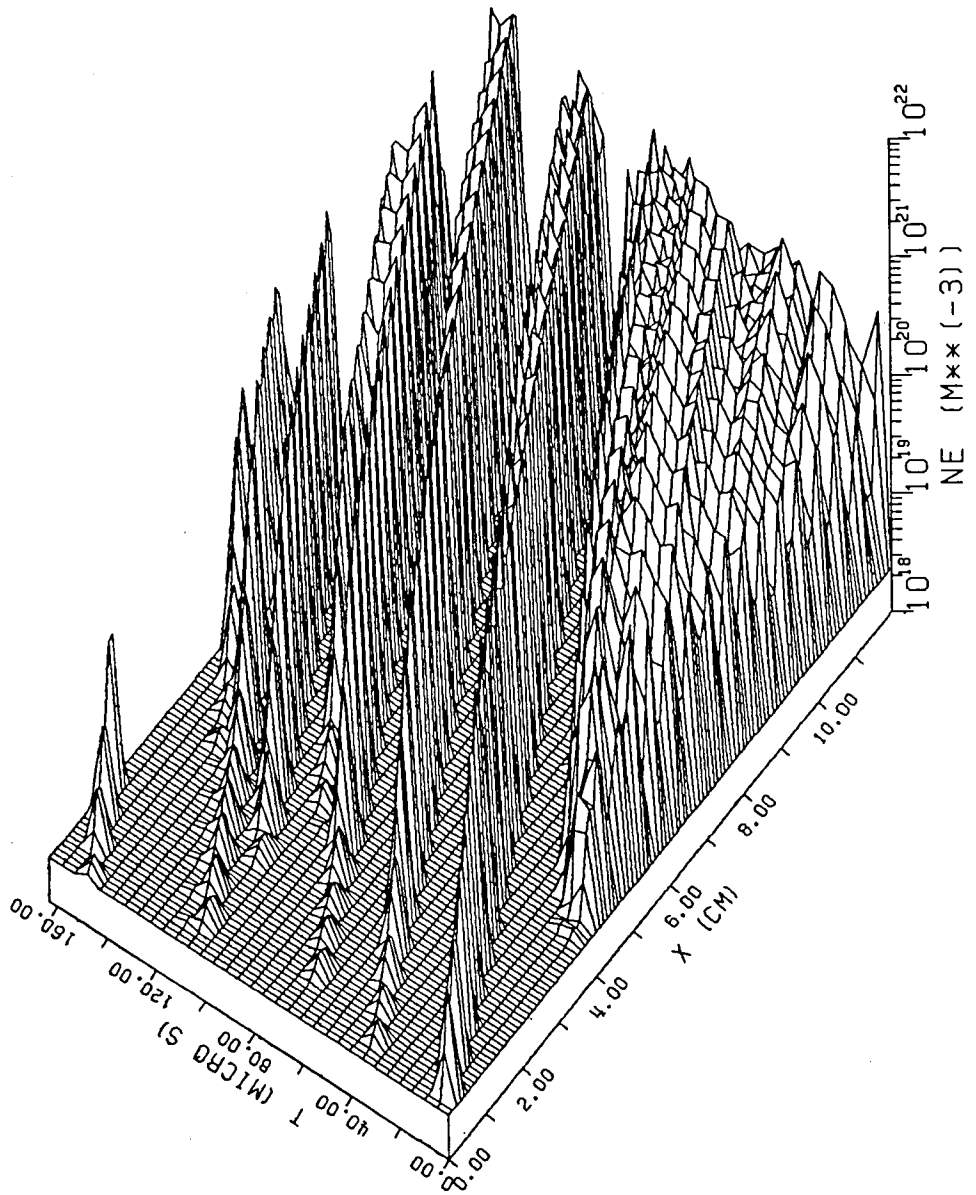

Fig. 3.6 Time-dependent electron density distribution in x direction for B = 3 T, $\varepsilon = 2 \times 10^{-4}$ and R_L = 4 Ω.

equilibrium and the cesium is almost fully ionized. Therefore, the plasma in the streamers is stable according to the linear perturbation theory. Outside the streamers, 1500 K $< T_e <$ 2000 K and $n_e \fallingdotseq 2 \times 10^{18}$ m^{-3}, which are almost equal to the initial conditions. On the other hand, according to the conventional linear perturbation theory, such plasma is unstable and so it cannot exist steadily in the channel at B = 3 T. Therefore, the above facts cannot be explained by the conventional one. So, it is evident that the conventional one cannot clarify the steady state of the plasma after the nonlinear growth of the ionization instability. This is because the nonuniformity of the plasma and the influences of the external circuit are not considered in the conventional theory.

3.5 Influence of Electrode Configuration on Current Distribution

The results obtained in the preceding section tell that the pitch of the streamers in the steady state does not coincide with that of the electrodes. Not only this fact but also the following fact were found by experiments[10]: the current distribution in the channel does not depend on the electrode configuration. However, this fact cannot be explained by the previous analysis on which the periodic conditions in one pitch region were imposed. To explain it, simulations are made for two channels with different electrode configurations of Types 1 and 3 shown in Table 3.1, where the magnetic flux density B = 3 T and the seed fraction $\varepsilon = 2 \times 10^{-4}$ are adopted for both channels. Since the load per unit length must be same in both channels and the electrode pitch of Type 3 channel is two times as long as that of Type 1 channel, the load resistances R_L = 1 and 0.5 Ω for Types 1 and 3 channels, respectively, are used.

The current distributions in the steady state in the Types 1 and 3 channels are shown in Figs. 3.7 and 3.8, respectively. The figures denote that the current distributions in

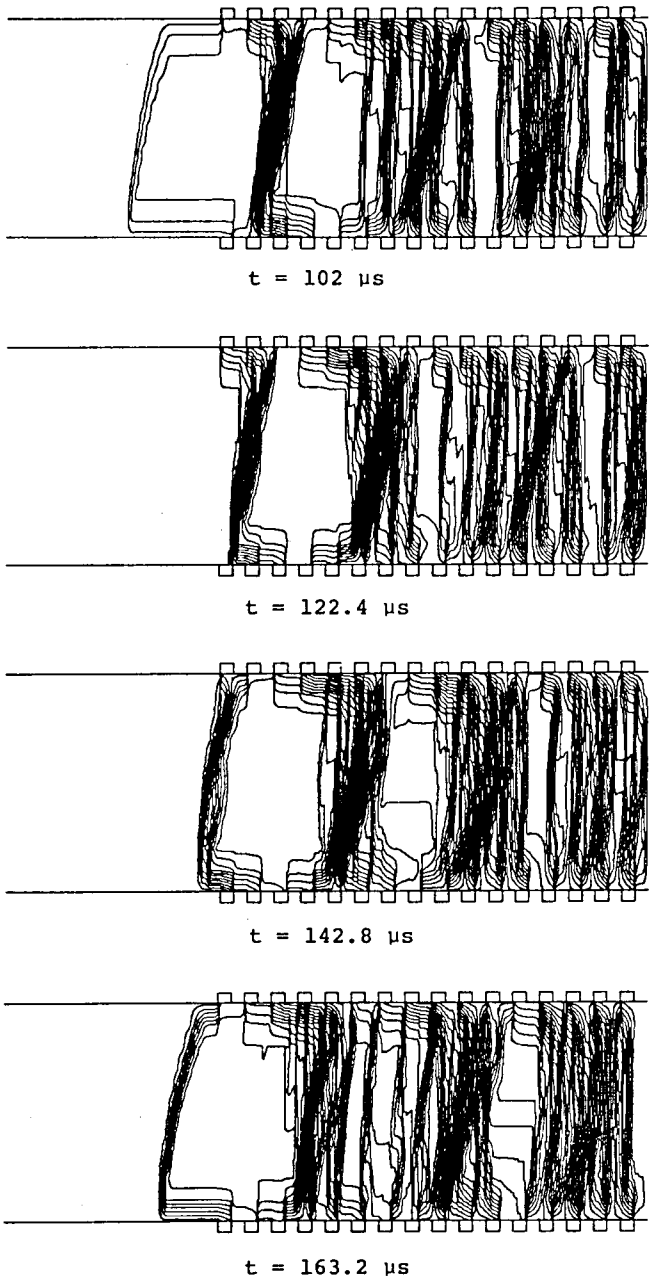

Fig. 3.7 Current distributions in Type 1 channel for B = 3 T, $\varepsilon = 2 \times 10^{-4}$ and R_L = 1 Ω ($\Delta\Psi$ = 5 A).

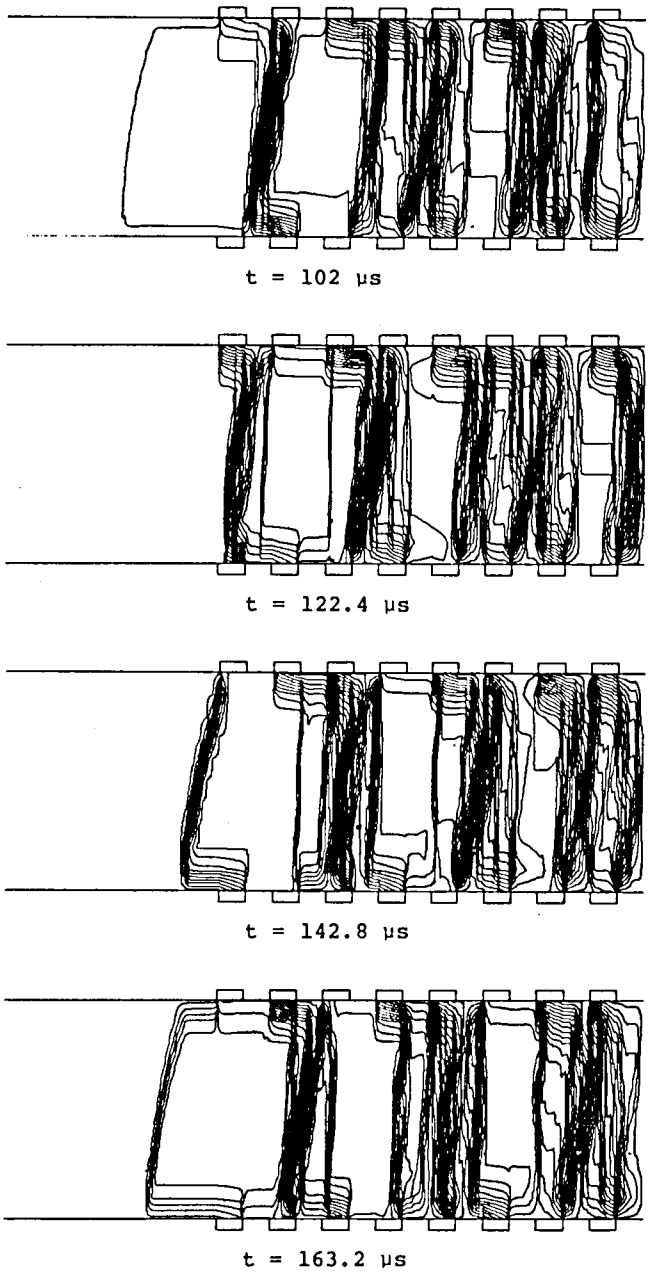

Fig. 3.8 Current distributions in Type 3 channel for B = 3 T, $\varepsilon = 2 \times 10^{-4}$ and R_L = 1 Ω ($\Delta\Psi$ = 5 A).

both channels are almost same at any time, except that the streamers in the Type 3 channel are slightly thinner than in the Type 1 channel and the total current in the Type 3 channel is smaller than the one in the Type 1 channel by the effect of finite segmenting. Therefore, if the load per unit length is same, the current distributions in the channels are almost same regardless of the electrode configuration.

By the above explanation, it was made clear that the author's numerical simulation can explain the experimental results very well. Moreover, these could be explained theoretically for the first time.

3.6 Influence of Convection of Plasma on Current Distribution

In Sections 3.4 and 3.5, it was already made clear that, although the the pitch of the streamers is equal to the electrode pitch just after the load resistances are connected to the electrodes, it does not depend on the electrode configuration in the steady state. It is also clarified that the streamers are formed near the inlet of the channel in the steady state and they are carried downstream in the channel at the speed equal to that of the working plasma. From these facts, main factor which determines the current distribution in the channel in the steady state is considered to be the convection effect of the plasma.

To confirm the above consideration, a numerical analysis is performed for the case that there exists no convection effect but exists the electromotive force. Physically such conditions do not exist, but it is useful to investigate the current distribution in this case. In the analysis, the plasma velocity u in Eqs. (2.54) and (2.55) is assumed to be 0 and all other numerical conditions are chosen the same as those used in Section 3.4.

Figures 3.9(a) and (b) show the time dependent current distributions in the channel from $t = 0$ to $t = 76.5\ \mu s$.

Figures 3.3(a) to (c), 3.9(a) and (b) denote that the current distributions in both channels are almost same and the pitch of the streamers are almost equal to the electrode pitch for $t < 10.2\ \mu s$. Also for $t > 10.2\ \mu s$, although the current distribution changes and becomes independent of the electrode configuration in the case where the convection effect of the plasma is taken into account, it does not change and depends on the electrode pitch in the case where the convection effect of the plasma is not taken into account.

The above results make clear that the main factors which determine the current distribution in the channel are not only the ionization instability but also the convection effect of the plasma. Namely, the origin of the inhomogeneous current distribution in the channel is the instability of the plasma and another main factor which determines the current one in the steady state is the convection effect of the plasma.

3.7 Concluding Remarks

In this chapter, there were carried out the two-dimensional time-dependent numerical analyses of the current distributions in the inlet region of the nonequilibrium linear Faraday generator channels with constant rectangular cross section by the numerical solution introduced in the preceding chapter, and the obtained results are as follows:

(1) In the transient state just after every load resistance is connected to every anode and cathode, the pitch of the streamers is equal to the electrode pitch because their origins are the current concentrations near the electrode edges. However, after those streamers have been carried downstream, the streamers are formed near the inlet of the channel and the pitch of the streamers does not coincide with the electrode pitch.

(2) For the conditions which are usually used in the experiments,

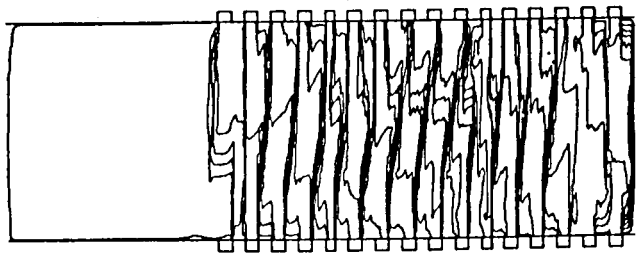

t = 5.1 μs

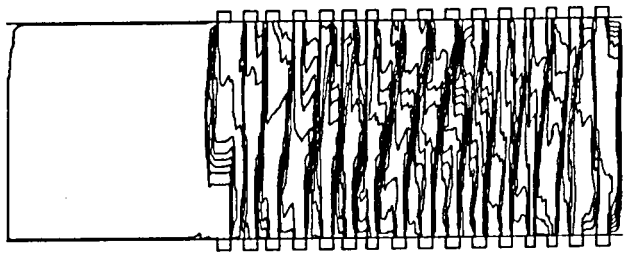

t = 10.2 μs

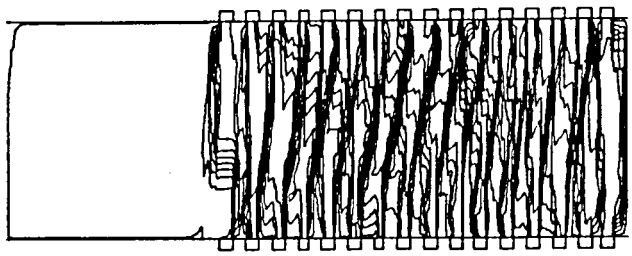

t = 20.4 μs

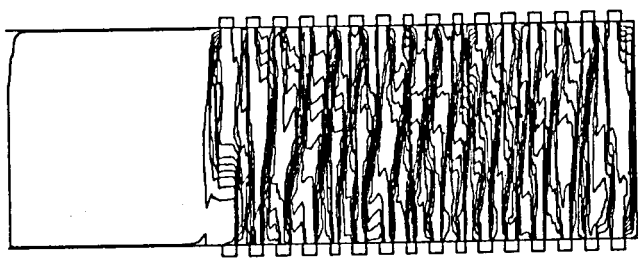

t = 30.6 μs

Fig. 3.9(a) Current distributions without convection for B = 3 T, $\varepsilon = 2 \times 10^{-4}$ and R_L = 4 Ω ($\Delta\Psi$ = 2 A).

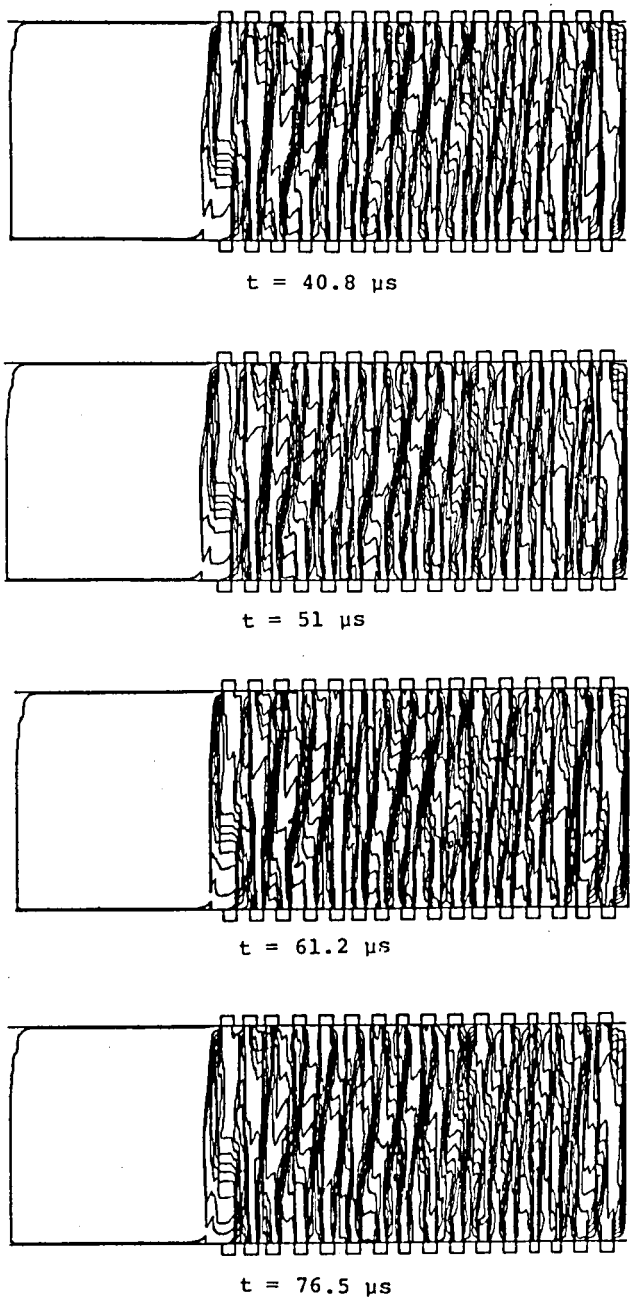

Fig. 3.9(b) Current distributions without convection for B = 3 T, $\varepsilon = 2 \times 10^{-4}$ and R_L = 4 Ω ($\Delta\Psi$ = 2 A).

the current distribution in the channel in the steady state is inhomogeneous and the streamers are formed to interconnect the anode and the cathode.

(3) By the convection effect of the plasma, the streamers are carried downstream in the channel at the speed equal to that of the working plasma.

(4) In the steady state, each streamer is consisted of several finely striated structures.

(5) In the steady state, if the load per unit length is same, the current distributions in the channel are almost the same independent of the electrode configuration.

(6) The origin of the inhomogeneous current distribution in the channel is the ionization instability of the plasma and another main factor which determine the current one in the steady state is the convection effect of the plasma.

(7) The above results can well explain the experimentally observed evidences, which could not be explained by the previous analyses.

CHAPTER 4

INFLUENCES OF VARIOUS FACTORS ON PERFORMANCE CHARACTERISTICS OF LINEAR FARADAY GENERATOR

4.1 Introduction

In the preceding chapter, the formation process of the inhomogeneous current distribution in the linear Faraday generator channel and the main factors which determine the distribution were theoretically made clear. It has been shown by many experiments that the current distribution is also influenced by the values of load resistance, seed fraction, etc.

However, since it was not yet theoretically clarified, in this chapter, the dependences of the current distribution and the other generator performances on the above factors are investigated by the numerical solution introduced in Chapter 2[42]. At first, the influences of the load resistance, the seed fraction and the magnetic flux density on the performance characteristics of the generator using the cesium seeded argon plasma are made clear. Next, the same investigations are performed with respect to the generator using the potassium seeded argon plasma and the differences between the former and the latter characteristics are also made clear.

4.2 Performance Characteristics of Faraday Generator Using Cesium Seeded Argon Plasma

4.2.1 Influence of load resistance[43]

At first, influences of the load resistance on the current distribution in the channel and the other generator performances are investigated. In this chapter, Type 1 channel in Table 3.1 is analyzed and the gasdynamic conditions are chosen as same as used in the preceding chapter. Moreover, magnetic flux density B = 3 T and seed fraction $\varepsilon = 2 \times 10^{-4}$ are adopted. Numerical analyses are performed in the cases of the load resistances R_L = 20 and 0.2 Ω in addition to the cases of R_L = 4 and 1 Ω which were already analyzed in the preceding chapter.

Figures 4.1(a) to (c) show the current distribution in the channel in the steady state, where t = 163.2 μs, the one of the electron density n_e in the x direction on the center line of the channel at t = 163.2 μs and the time dependence of the load current of the 10th electrode pair from the channel inlet, respectively, in the case of R_L = 20 Ω. The similar figures in the cases of R_L = 4, 1 and 0.2 Ω are also shown in Figs. 4.2 to 4.4.

These current distributions show that the pitch of the streamers becomes short as the load resistance becomes small. In addition, the width of the streamers becomes wide as the load resistance lowers. Consequently, the width becomes almost equal to the pitch, and so the current distribution in the channel becomes almost homogeneous for R_L = 0.2 Ω. Since the electron density $n_e = 1.63 \times 10^{21}$ m^{-3} in the case of fully ionized seed, the figures showing the electron density distributions tell that the seed is almost fully ionized and the argon is scarcely ionized in the streamers for all load resistances. Namely, the argon is not ionized but the region of the streamers becomes wide as the current becomes large in the channel.

The figures showing the time dependence of the load current denote that it fluctuates in time and the period of the fluctuation becomes short as the load resistance lowers. Accordingly, this fluctuation of the load current is considered to be originated in the inhomogeneous current distribution in the channel.

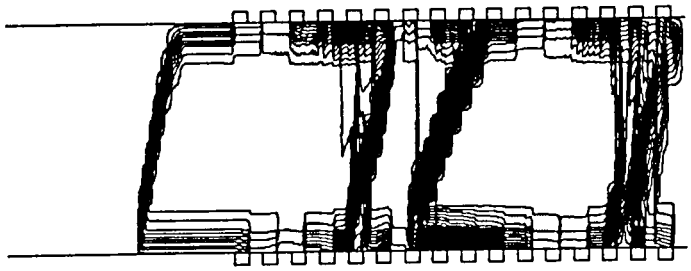

(a) Current distribution at t = 163.2 μs ($\Delta\Psi$ = 0.5 A).

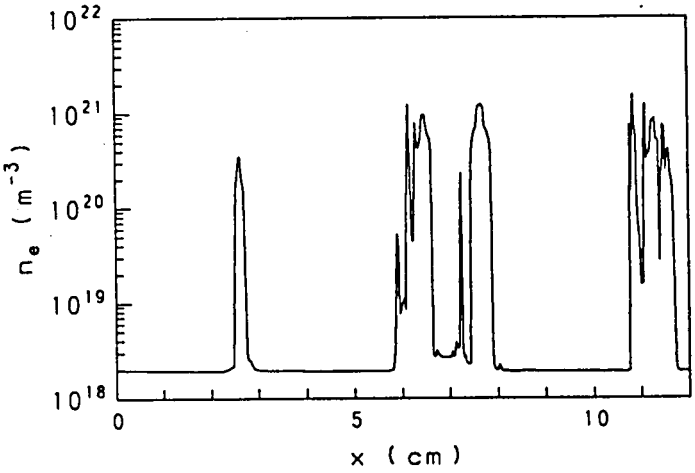

(b) Electron density distribution at t = 163.2 μs.

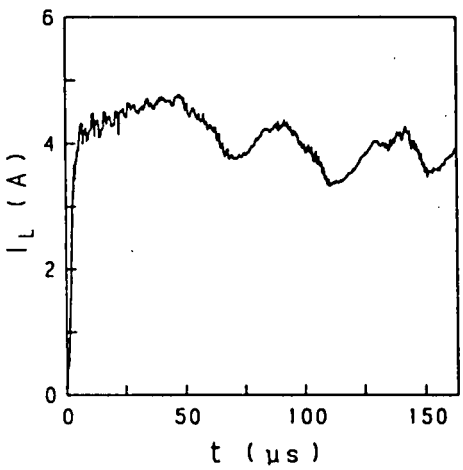

(c) Time dependence of 10th electrode current.

Fig. 4.1 Performance characteristics of generator using C_s-A_r for B = 3 T, ε = 2 × 10^{-4} and R_L = 20 Ω.

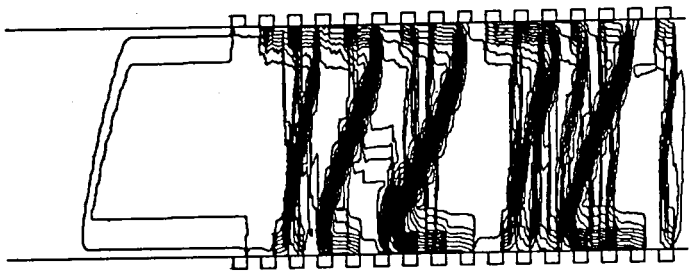

(a) Current distribution at t = 163.2 μs ($\Delta\Psi$ = 2 A).

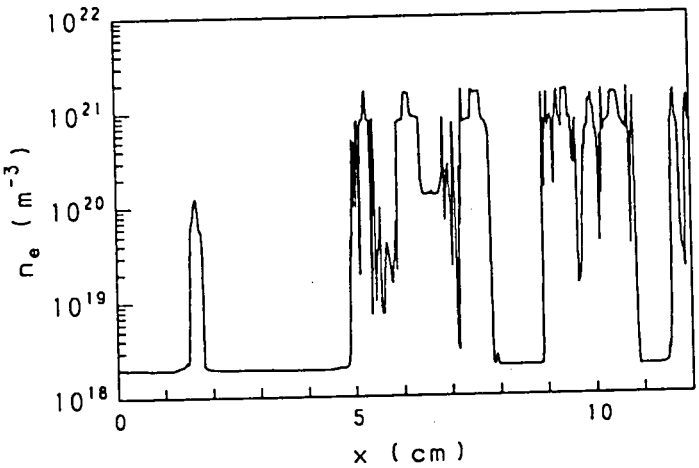

(b) Electron density distribution at t = 163.2 μs.

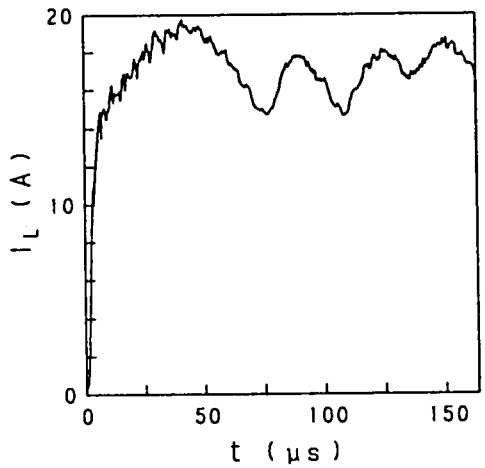

(c) Time dependence of 10th electrode current.

Fig. 4.2 Performance characteristics of generator using C_s-A_r for B = 3 T, $\varepsilon = 2 \times 10^{-4}$ and R_L = 4 Ω.

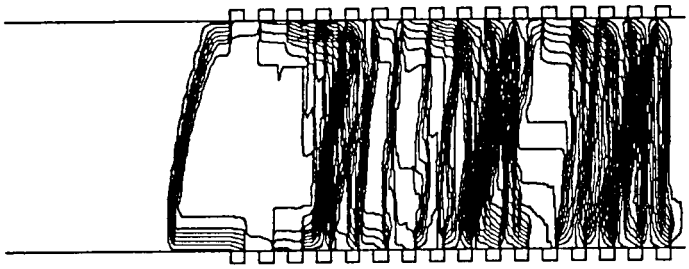

(a) Current distribution at t = 163.2 μs ($\Delta\Psi$ = 5 A).

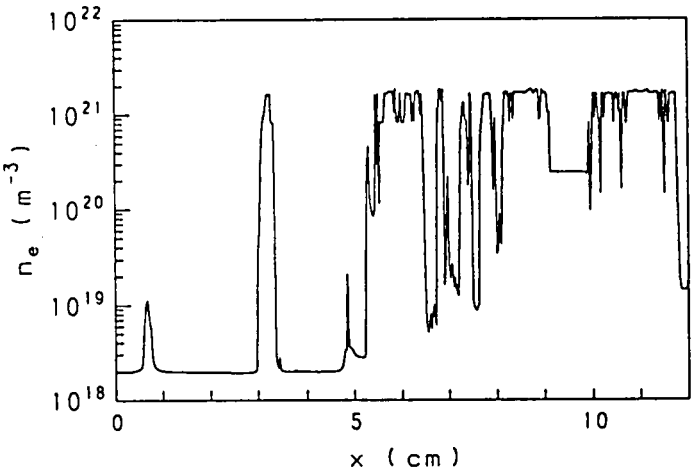

(b) Electron density distribution at t = 163.2 μs.

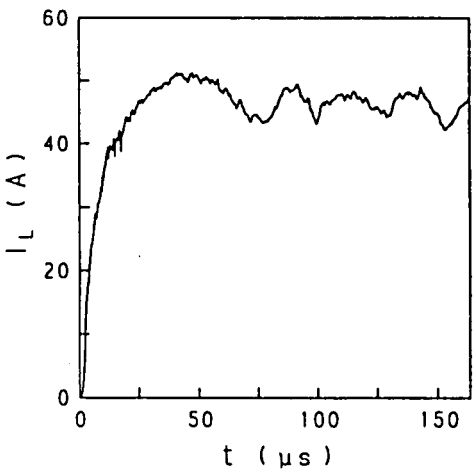

(c) Time dependence of 10th electrode current.

Fig. 4.3 Performance characteristics of generator using C_s-A_r for B = 3 T, ε = 2 × 10^{-4} and R_L = 1 Ω.

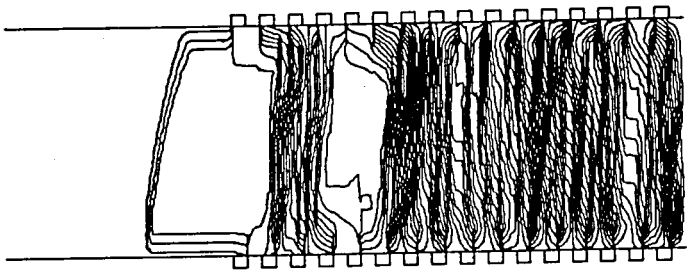

(a) Current distribution at t = 163.2 μs ($\Delta\Psi$ = 10 A).

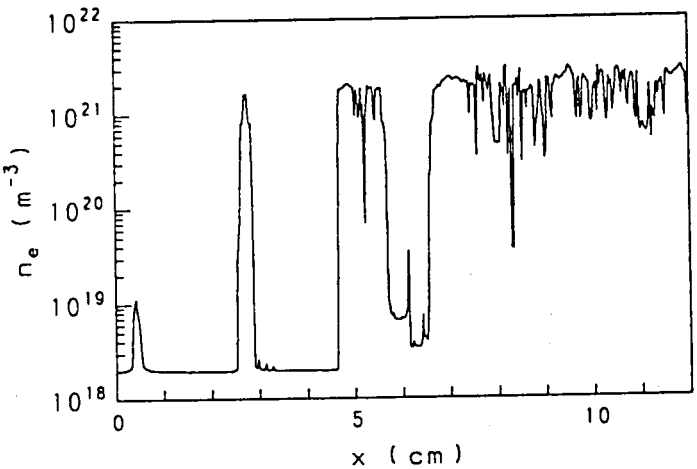

(b) Electron density distribution at t = 163.2 μs.

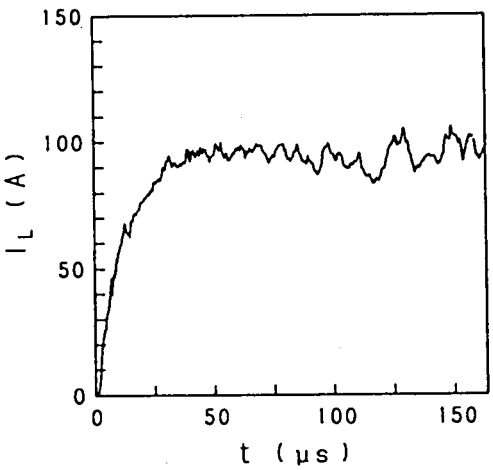

(c) Time dependence of 10th electrode current.

Fig. 4.4 Performance characteristics of generator using C_s-A_r for B = 3 T, ε = 2 × 10^{-4} and R_L = 0.2 Ω.

The above facts tell that the plasma in the channel is unstable and the current distribution becomes inhomogeneous when $R_L \geqq 1\ \Omega$ but the plasma is stable and the current distribution becomes homogeneous when $R_L = 0.2\ \Omega$. This is due to the fact that the Joule heat is not sufficient to realize the fully ionized seed when $R_L \geqq 1\ \Omega$ and it is sufficient when $R_L = 0.2\ \Omega$ because it becomes large as the load resistance lowers.

The Faraday generator is usually operated in the condition that the load factor $K = V_L/V_{open} = 0.5$ to 0.6, where V_L and V_{open} are the load voltage and the open-circuit voltage, respectively. Since $V_{open} = uBh \fallingdotseq 120$ V, it is appropriate that $V_L = 60$ to 70 V in the present case. Accordingly, $R_L = 4\ \Omega$ is appropriate because the load current $I_L = 15$ to 18 A as shown in Fig. 4.2(c) and $V_L = I_L R_L = 60$ to 72 V in this case. Therefore, the current distribution in the channel is inhomogeneous for the suitable load factor in the conditions used in the calculations.

4.2.2 Influence of seed fraction[44]

In this subsection, influences of the seed fraction on the current distribution and the other performance characteristics of the generator are studied. For this purpose, at first, numerical calculation is performed for $\varepsilon = 5 \times 10^{-5}$. In the calculation, the load resistance $R_L = 4\ \Omega$ is assumed and all other conditions are chosen as same as used in the preceding subsection, because the optimum load resistance $R_L = 4\ \Omega$ is obtained by applying the linear perturbation theory[21] to the results obtained in the preceding subsection.

The figures corresponding to Figs. 4.2(a) to (c) for $\varepsilon = 2 \times 10^{-4}$ are shown in Figs. 4.5(a) to (c) for $\varepsilon = 5 \times 10^{-5}$, respectively. From Fig. 4.5(a), it is seen that the current distribution in the channel is inhomogeneous. As the electron density $n_e = 4.08 \times 10^{20}\ m^{-3}$ in the case of fully ionized seed, Figure 4.5(b) tells that the plasma in the streamers satisfies the

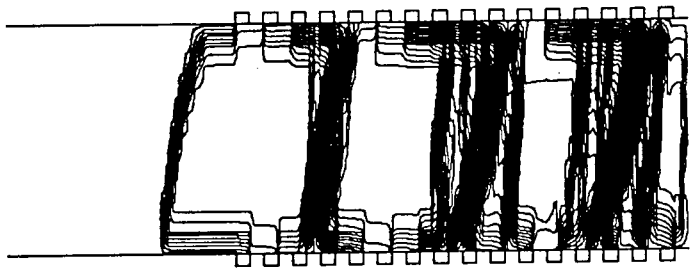

(a) Current distribution at t = 163.2 μs ($\Delta\Psi$ = 1 A).

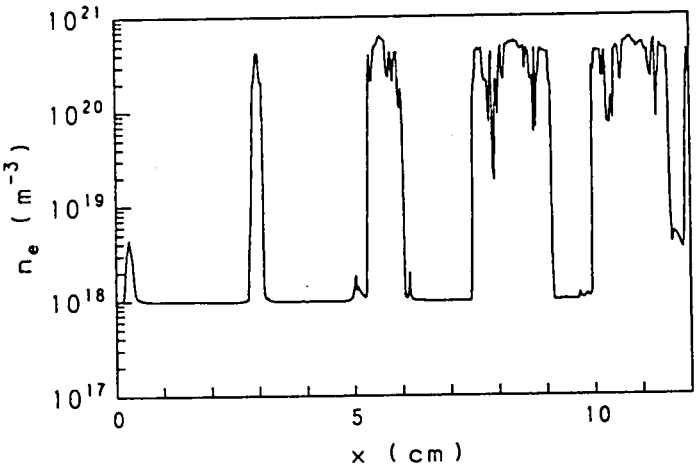

(b) Electron density distribution at t = 163.2 μs.

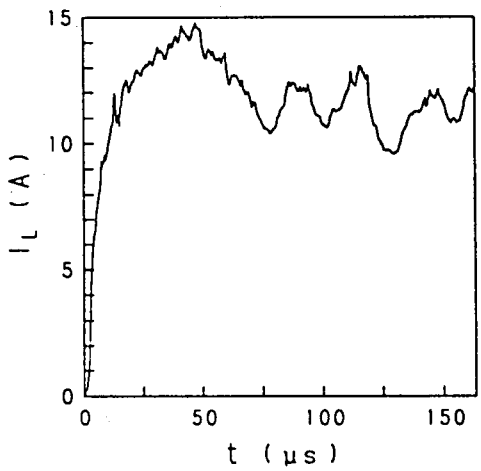

(c) Time dependence of 10th electrode current.

Fig. 4.5 Performance characteristics of generator using C_s-A_r for B = 3 T, ε = 5 × 10^{-5} and R_L = 4 Ω.

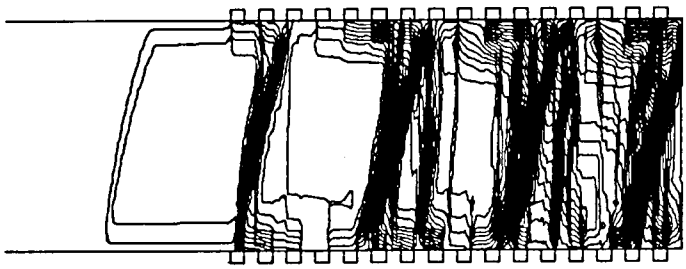

(a) Current distribution at t = 163.2 μs ($\Delta\Psi$ = 0.5 A).

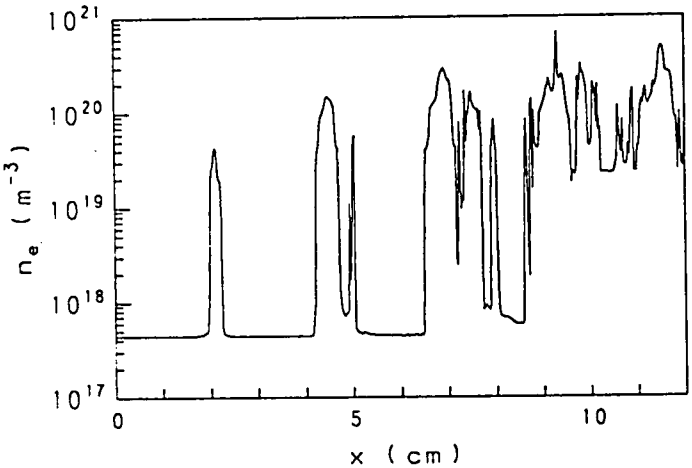

(b) Electron density distribution at t = 163.2 μs.

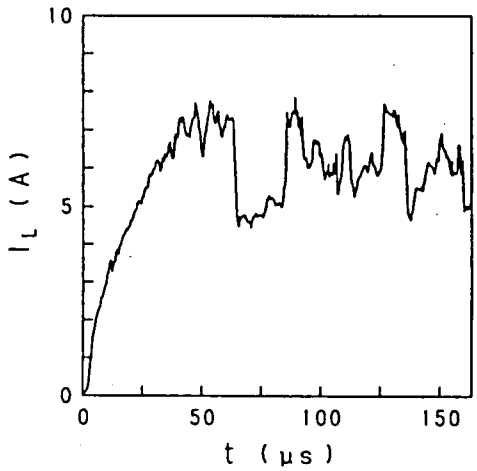

(c) Time dependence of 10th electrode current.

Fig. 4.6 Performance characteristics of generator using C_s-A_r for B = 3 T, ε = 10^{-5} and R_L = 4 Ω.

condition of fully ionized seed but in the channel there exists the region in which the seed is not fully ionized. Also, it is seen from Fig. 4.5(c) that the load current for $\varepsilon = 5 \times 10^{-5}$ is smaller than the one for $\varepsilon = 2 \times 10^{-4}$. Therefore, the inhomogeneous distribution of the current in Fig. 4.5(a) is due to the fact that the Joule heat required to realize the fully ionized seed becomes small as the seed fraction becomes small from $\varepsilon = 2 \times 10^{-4}$ to $\varepsilon = 5 \times 10^{-5}$ but the obtained Joule heat becomes also small and it is still insufficient.

Next, numerical calculation for still lower seed fraction $\varepsilon = 10^{-5}$ is carried out, where all other conditions are chosen as same as in the case of $\varepsilon = 2 \times 10^{-4}$ or $\varepsilon = 5 \times 10^{-5}$. The figures corresponding to Figs. 4.2(a) to (c) for $\varepsilon = 2 \times 10^{-4}$ are shown in Figs. 4.6(a) to (c) for $\varepsilon = 10^{-5}$, respectively. As the electron density $n_e = 8.16 \times 10^{19}$ m^{-3} in the case of fully ionized seed, it is seen from these figures that the current distribution is still inhomogeneous and the argon is ionized in the streamers, although the seed is not yet fully ionized outside the streamers. It is also seen that the load current for $\varepsilon = 10^{-5}$ is remarkably smaller than that for $\varepsilon = 5 \times 10^{-5}$ and it fluctuates more severely.

4.2.3 Influence of magnetic flux density

At last, the influences of the magnetic flux density on the current distribution in the channel are investigated. Since the case of $B = 3$ T, $\varepsilon = 2 \times 10^{-4}$ and $R_L = 4\ \Omega$ was already studied in Subsection 4.2.1, three cases of $B = 4$, 2 and 1 T, where $\varepsilon = 2 \times 10^{-4}$ and $R_L = 4\ \Omega$ are adopted, are studied in this subsection.

The figures corresponding to Figs. 4.2(a) to (c) for $B = 3$ T are shown in Figs. 4.7 to 4.9 for $B = 4$, 2 and 1 T, respectively. Figures 4.2 and 4.7 to 4.9 tell that the angle between the streamers and the y axis becomes large and the fluctuation of the load current becomes large as the magnetic flux density becomes

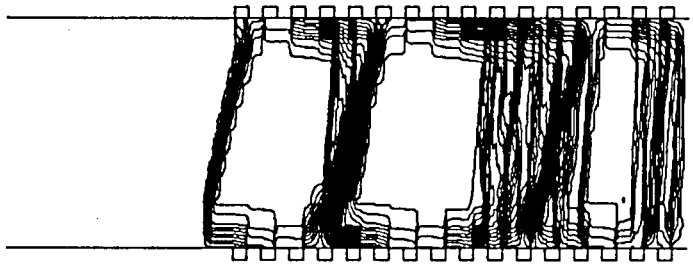

(a) Current distribution at t = 163.2 μs ($\Delta\Psi$ = 3 A).

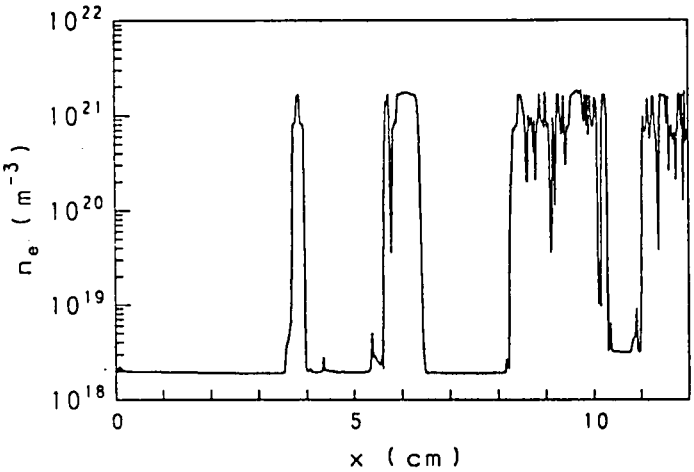

(b) Electron density distribution at t = 163.2 μs.

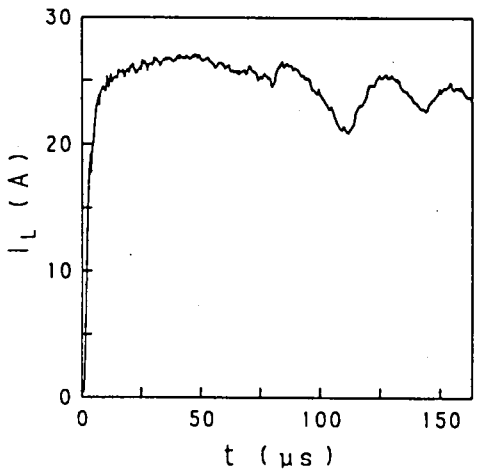

(c) Time dependence of 10th electrode current.

Fig. 4.7 Performance characteristics of generator using C_s-A_r for B = 4 T, $\varepsilon = 2 \times 10^{-4}$ and R_L = 4 Ω.

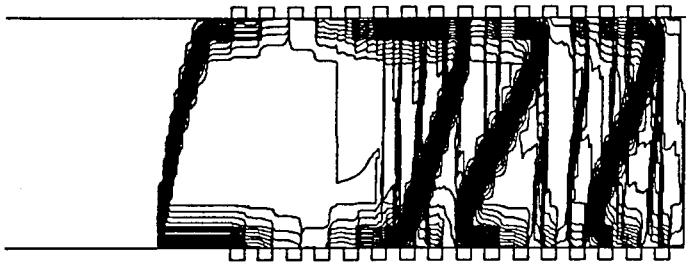

(a) Current distribution at t = 163.2 μs ($\Delta\Psi$ = 1 A).

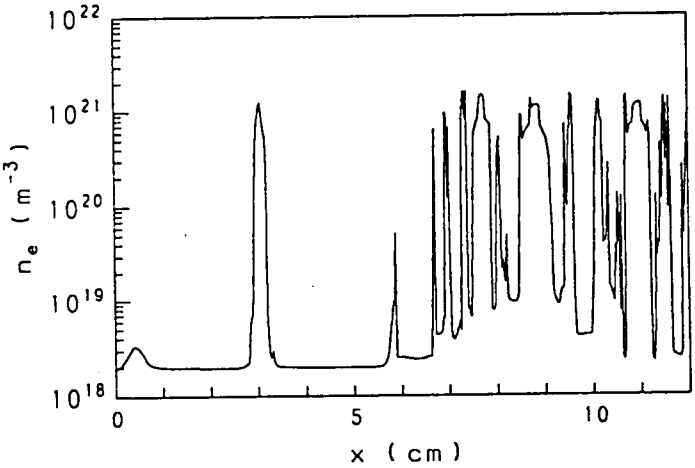

(b) Electron density distribution at t = 163.2 μs.

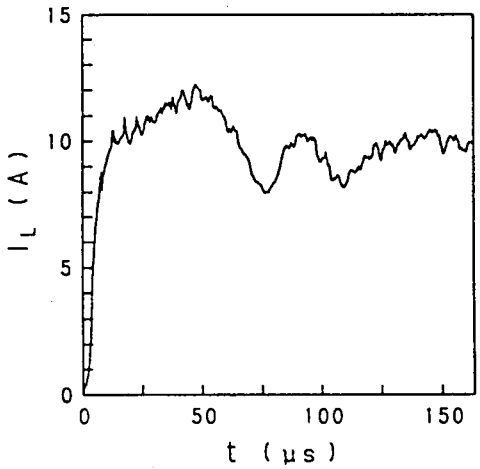

(c) Time dependence of 10th electrode current.

Fig. 4.8 Performance characteristics of generator using C_s-A_r for B = 2 T, ε = 2 × 10^{-4} and R_L = 4 Ω.

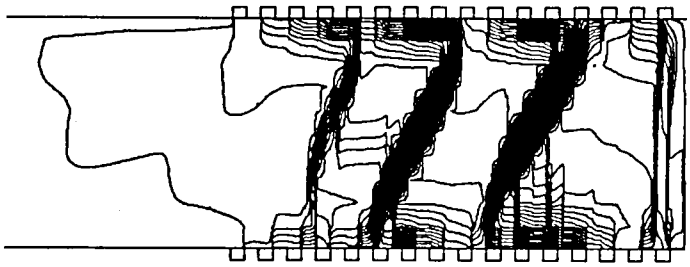

(a) Current distribution at t = 163.2 μs ($\Delta\Psi$ = 0.4 A).

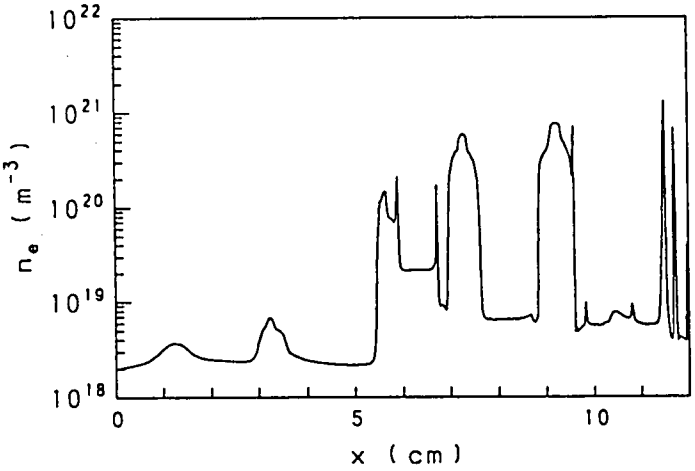

(b) Electron density distribution at t = 163.2 μs.

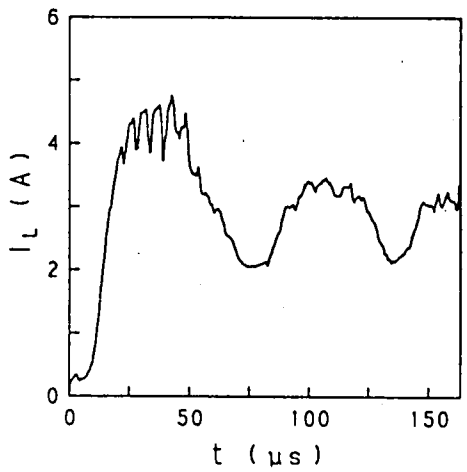

(c) Time dependence of 10th electrode current.

Fig. 4.9 Performance characteristics of generator using C_s-A_r for B = 1 T, ε = 2 × 10^{-4} and R_L = 4 Ω.

small. It is also seen from these figures that the seed in the streamers is not fully ionized at B = 1 T, though it is fully ionized at $B \geqq 2$ T.

4.3 Performance Characteristics of Faraday Generator Using Potassium Seeded Argon Plasma

In the preceding section, the current distribution and the other generator performances were made clear in the case cesium seeded argon plasma is used as the working plasma. However, in the experiments, not only the cesium seeded argon plasma but also the potassium seeded argon plasma are used. Therefore, in this section, the current distribution in the channel and the other generator performances using potassium seeded argon plasma are investigated. The differences between the performance characteristics of the generator using the cesium and the potassium seeded argon plasma are also investigated.

Here, the gasdynamic conditions are chosen as same as used in the preceding section because the quantities of the argon which are determined by those conditions must be same. Numerical analyses are performed for the following seven cases, namely (1) the magnetic flux density B = 3 T, the seed fraction $\varepsilon = 2 \times 10^{-4}$ and the load resistance R_L = 20 Ω, (2) B = 3 T, $\varepsilon = 2 \times 10^{-4}$ and R_L = 4 Ω, (3) B = 3 T, $\varepsilon = 2 \times 10^{-4}$ and R_L = 0.2 Ω, (4) B = 3 T, $\varepsilon = 10^{-5}$ and R_L = 4 Ω, (5) B = 4 T, $\varepsilon = 2 \times 10^{-4}$ and R_L = 4 Ω, (6) B = 2 T, $\varepsilon = 2 \times 10^{-4}$ and R_L = 4 Ω, (7) B = 1 T, $\varepsilon = 2 \times 10^{-4}$ and R_L = 4 Ω. The figures corresponding to Figs. 4.1(a) to (c) are shown in Figs. 4.10 to 4.16 for the above seven cases, respectively.

These figures tell that the current and the electron density distributions in the channel where the potassium seeded argon plasma is used are almost same as those in the one where the cesium seeded argon plasma is done for every condition. It is also seen

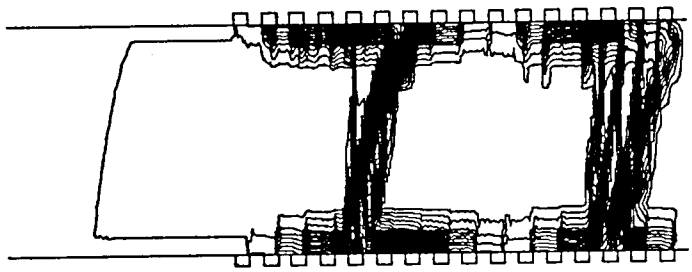

(a) Current distribution at t = 163.2 μs ($\Delta\Psi$ = 0.5 A).

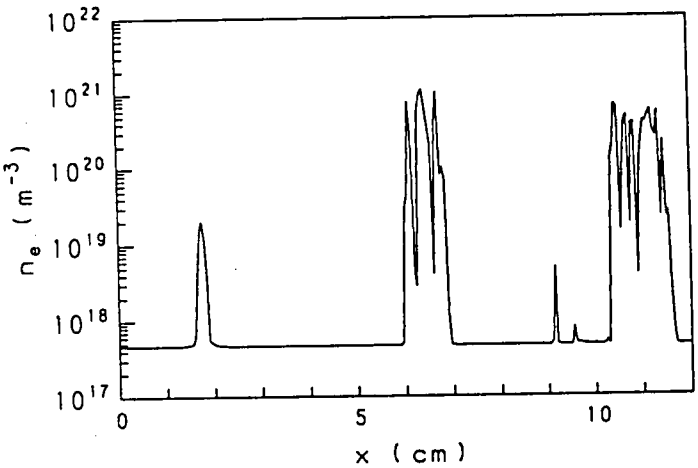

(b) Electron density distribution at t = 163.2 μs.

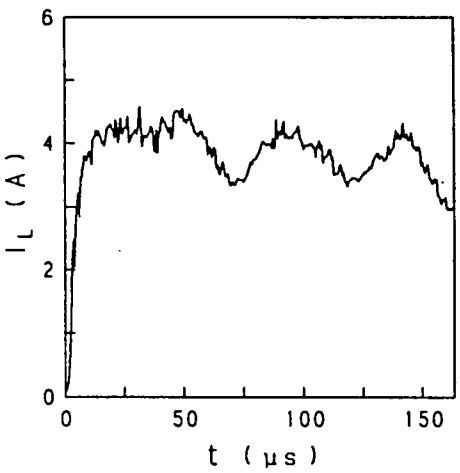

(c) Time dependence of 10th electrode current.

Fig. 4.10 Performance characteristics of generator using K-A_r for B = 3 T, $\varepsilon = 2 \times 10^{-4}$ and R_L = 20 Ω.

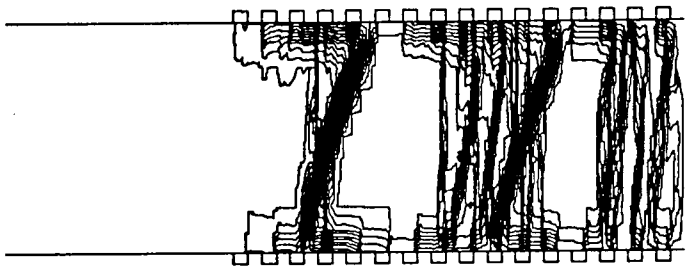

(a) Current distribution at t = 163.2 μs ($\Delta\Psi$ = 2 A).

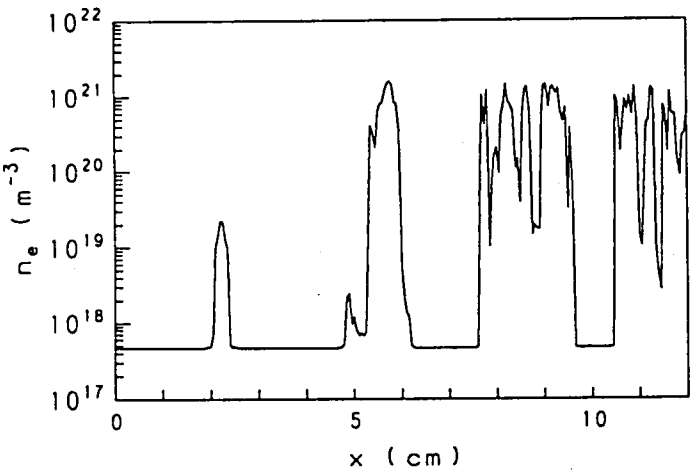

(b) Electron density distribution at t = 163.2 μs.

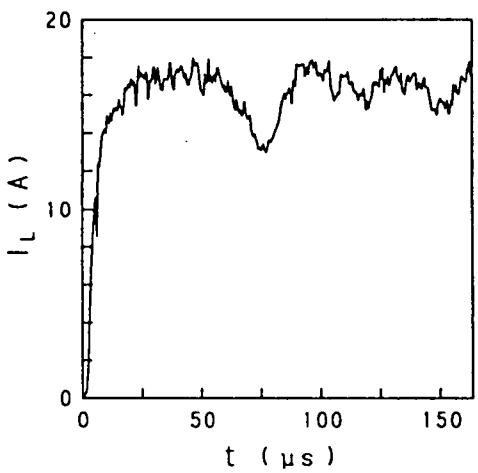

(c) Time dependence of 10th electrode current.

Fig. 4.11 Performance characteristics of generator using K-A_r for B = 3 T, $\varepsilon = 2 \times 10^{-4}$ and R_L = 4 Ω.

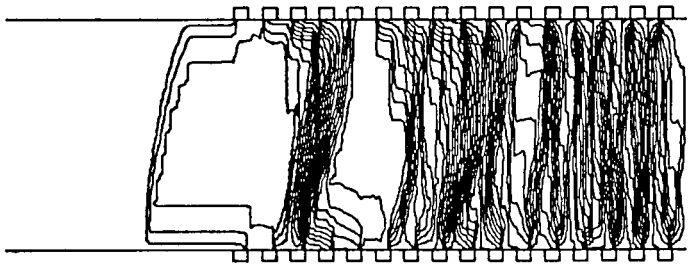

(a) Current distribution at t = 163.2 μs ($\Delta\Psi$ = 10 A).

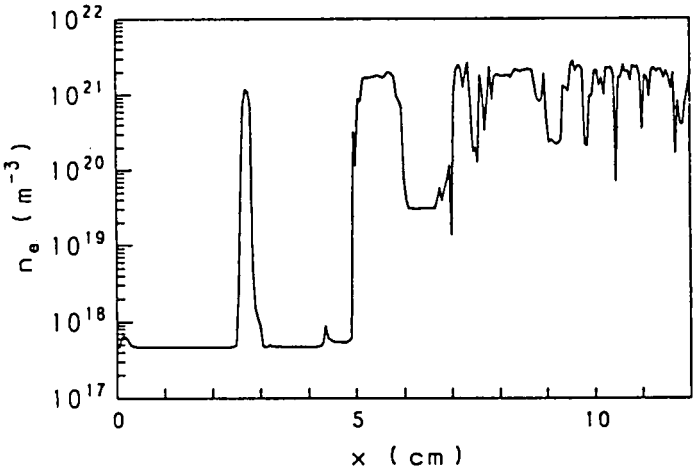

(b) Electron density distribution at t = 163.2 μs.

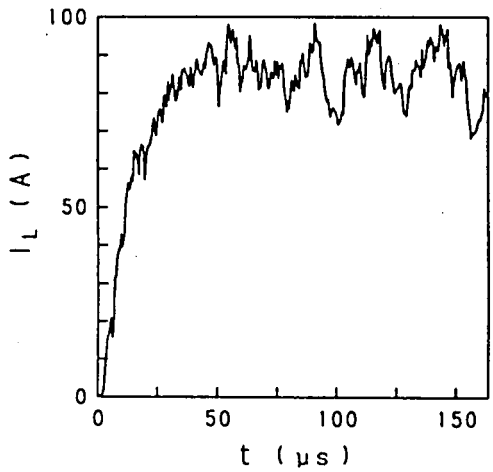

(c) Time dependence of 10th electrode current.

Fig. 4.12 Performance characteristics of generator using K-A_r for B = 3 T, $\varepsilon = 2 \times 10^{-4}$ and R_L = 0.2 Ω.

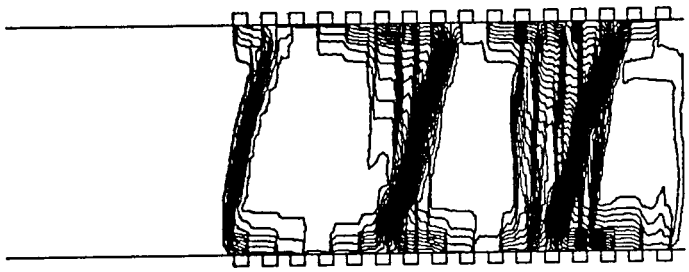

(a) Current distribution at t = 163.2 μs ($\Delta\Psi$ = 0.5 A).

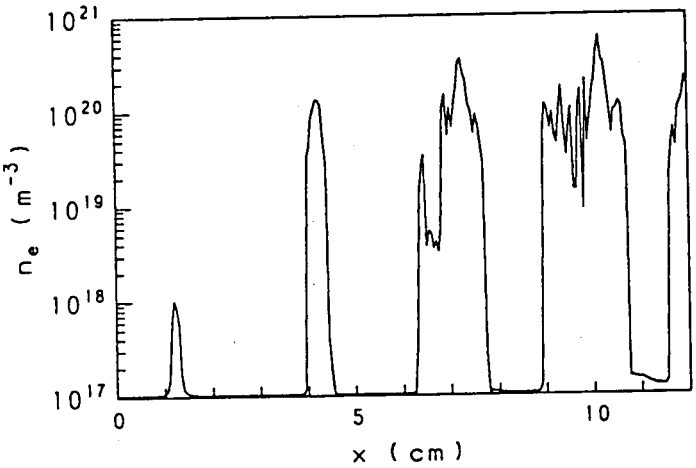

(b) Electron density distribution at t = 163.2 μs.

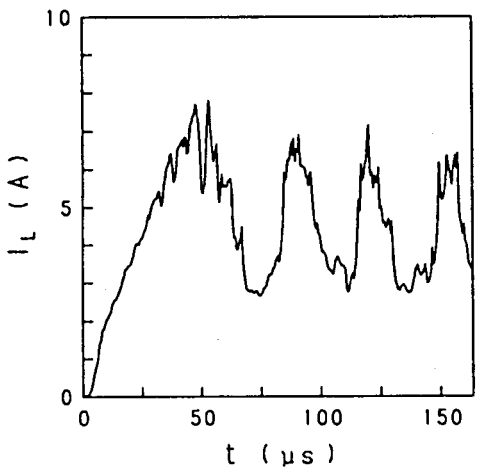

(c) Time dependence of 10th electrode current.

Fig. 4.13 Performance characteristics of generator using K-A_r for B = 3 T, $\varepsilon = 10^{-5}$ and R_L = 4 Ω .

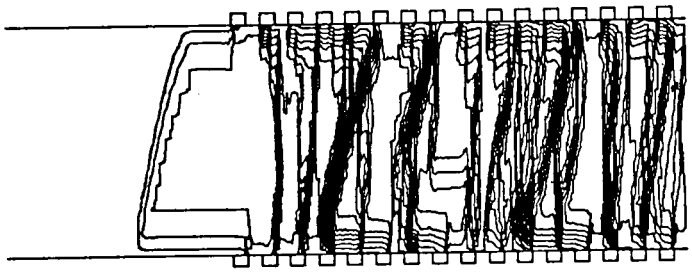

(a) Current distribution at t = 163.2 μs ($\Delta\Psi$ = 3 A).

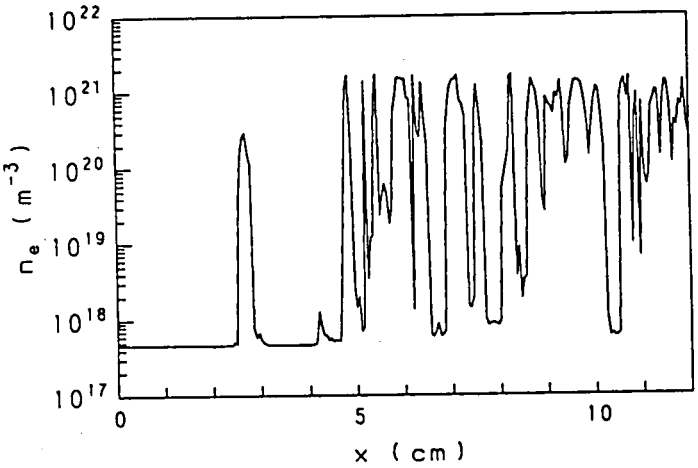

(b) Electron density distribution at t = 163.2 μs.

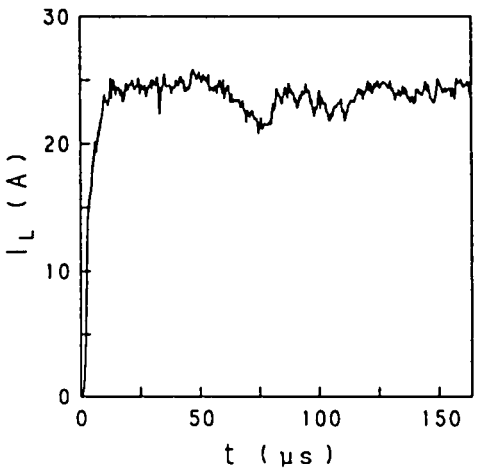

(c) Time dependence of 10th electrode current.

Fig. 4.14 Performance characteristics of generator using K-A_r for B = 4 T, ε = 2 × 10^{-4} and R_L = 4 Ω.

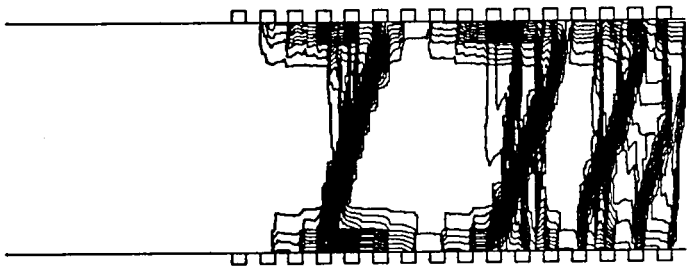

(a) Current distribution at t = 163.2 μs ($\Delta\Psi$ = 1 A).

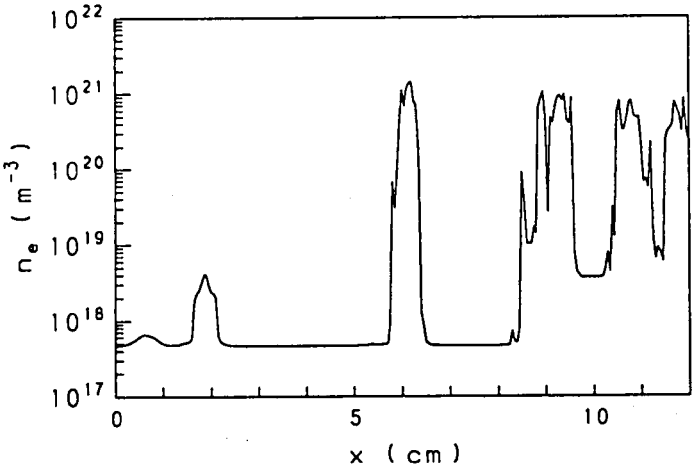

(b) Electron density distribution at t = 163.2 μs.

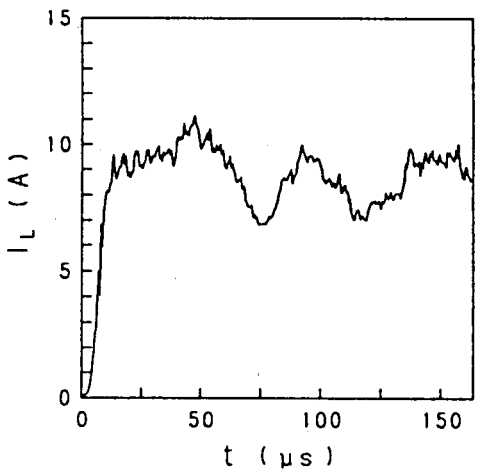

(c) Time dependence of 10th electrode current.

Fig. 4.15 Performance characteristics of generator using K-A_r for B = 2 T, ε = 2 × 10^{-4} and R_L = 4 Ω.

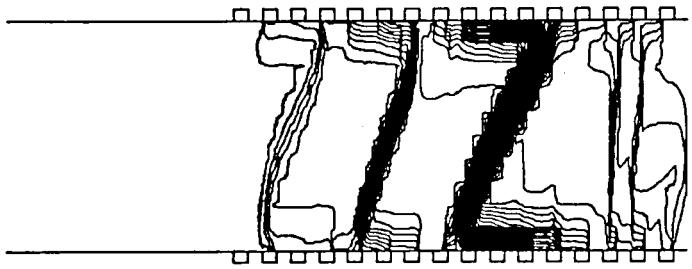

(a) Current distribution at t = 163.2 μs ($\Delta\Psi$ = 0.3 A).

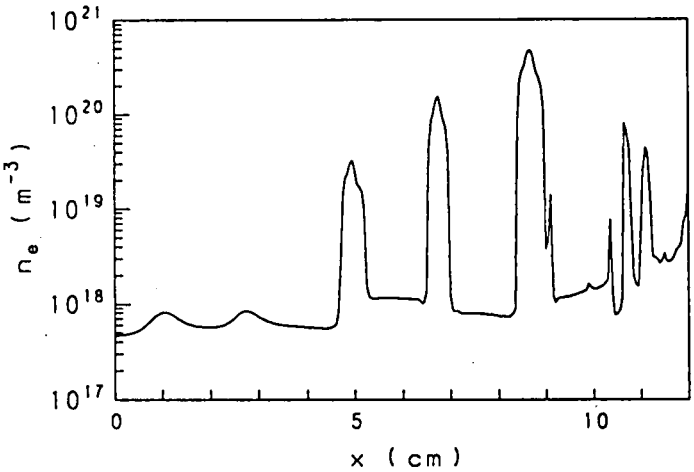

(b) Electron density distribution at t = 163.2 μs.

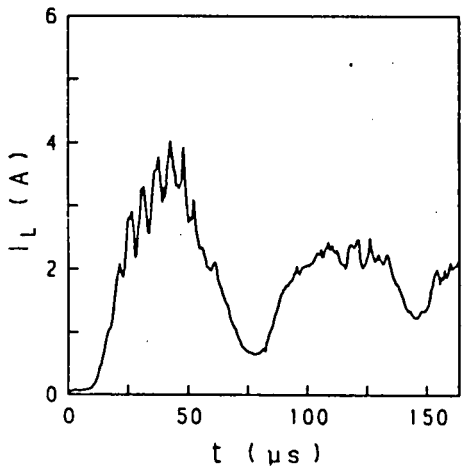

(c) Time dependence of 10th electrode current.

Fig. 4.16 Performance characteristics of generator using K-A_r for B = 1 T, ε = 2 × 10^{-4} and R_L = 4 Ω.

from those figures that the average load currents in the former are a little smaller than those in the latter. This is considered to be due to the fact that the ionization energy of the potassium is larger than that of the cesium. Moreover, the ratio of the average load current in the former to that in the latter becomes small as the load resistance, the seed fraction or the magnetic flux density lowers.

4.4 Concluding Remarks

In this chapter, the dependences of load resistance, seed fraction and magnetic flux density on the performance characteristics of the generator in which the cesium or the potassium seeded argon plasma is used as the working plasma were made clear.

At first, the following results were obtained in the former.

(1) The plasma is usually unstable and the current distribution in the channel is inhomogeneous except the case the load resistance is very small.

(2) The current distribution is inhomogeneous in the condition of low seed fraction because the load current decreases as the seed fraction becomes small.

(3) The angle between the streamers and the y axis becomes large and the fluctuation of the load current becomes large as the magnetic flux density becomes small.

Next, the following results were obtained in the latter.

(1) The current and the electron density distributions are almost same as those in the former for every condition.

(2) The ratio of the average load current in the channel where the potassium seeded argon plasma is used to that in the one where the cesium seeded argon plasma is used is always smaller than 1, and it becomes small as the load resistance, the seed fraction or the magnetic flux density lowers.

CHAPTER 5

NUMERICAL SOLUTION FOR OUTFLOW DISK GENERATOR

5.1 Introduction

In Chapters 2 to 4, the two-dimensional time-dependent solution for nonequilibrium linear Faraday generator was introduced and the current distributions in the channel are studied in detail. Also, it is made clear that in the linear Faraday generator, the plasma is unstable and the current distribution is inhomogeneous for the conditions usually used in the experiments. This is due to the fact that the Joule heating is not sufficient to fully ionize the seed in the channel.

Accordingly, to obtain a stable plasma, it is necessary to find out a way to heat efficiently the plasma in the channel. For this purpose, it is thought that a disk generator has an advantage over the linear Faraday generator, because the Faraday current is short-circuited and efficiently heats the plasma in the former channel. In fact, through the experiments by Shioda, et al., it was made clear that the seed can be fully ionized and the plasma can be stabilized fairly easily in the outflow disk generator[30],[31]. However, many important unknown items still remain about the distributions of the current, the electron temperature, the electron density, etc. in the disk generator.

The above-mentioned suggests that the numerical analyses of not only the linear generator but also the disk generator are needed. Therefore, in this chapter, the two-dimensional time-dependent numerical solution of the small-sized outflow disk generator is introduced[45]. First, the channel model of the disk

generator used in the numerical analysis and the basic equations which govern the partially ionized nonequilibrium plasma are introduced. Next, some inevitable assumptions are introduced and the basic equations are transformed into the simplified two-dimensional basic equations to be solved, and also the boundary conditions are presented. And the numerical solution for calculating the electric potential in the channel by applying the finite element method to the above two-dimensional basic equations and the boundary conditions is derived. Finally, the method to compute the current stream function by using the electric potential and the ones to evaluate the electron temperature and the electron density are shown.

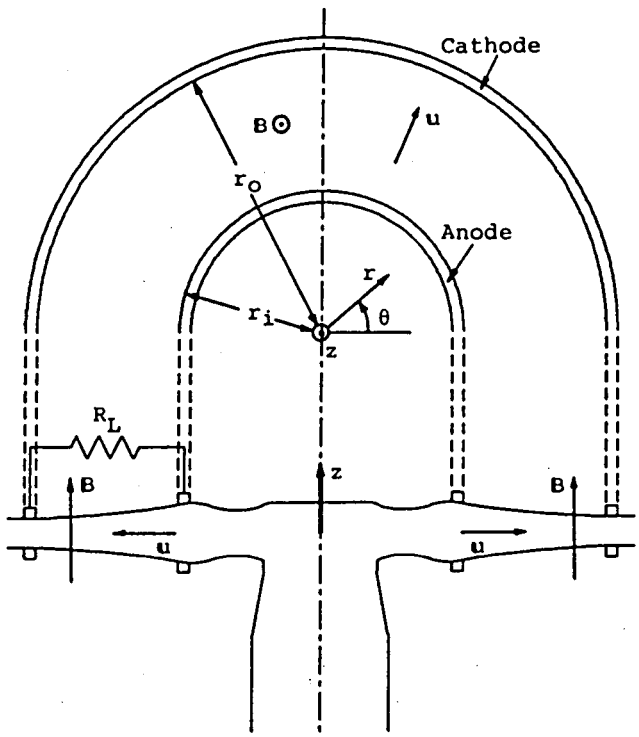

Fig. 5.1 Channel model of disk generator.

5.2 Channel Model

The schematic diagram of the disk generator channel model and the cylindrical coordinates (r,θ,z) used in this analysis are shown in Fig. 5.1, where r_i and r_o are the radii of the anode and the cathode, respectively. The two-dimensional numerical analyses are performed in the channel between the anode and the cathode. As the channels used in the experiments by Shioda and Yamasaki have constant cross sections[31], the channel model in this analysis is chosen to have the same configuration.

5.3 Basic Equations

In this analysis, cesium or potassium seeded argon plasma is considered as the working fluid in the generator channel. From the same reasons mentioned in Section 2.3, it is assumed that the interactions between the gasdynamic and the electrical quantities are negligible and the distributions of the gasdynamic quantities are constant in time. Accordingly, the same basic equations as well as in Section 2.3 can be adopted in this chapter. Namely, the basic equations are rearranged as follows:

$$J + \frac{\beta}{B}(J\times B) = \sigma(E^* + \frac{\nabla p_e}{en_e}) \tag{5.1}$$

$$\nabla\times E = 0 \tag{5.2}$$

$$\nabla\cdot J = 0 \tag{5.3}$$

$$\frac{\partial n_{ia}}{\partial t} + \nabla\cdot(n_{ia}u) = k_{fa}n_e n_a - k_{ra}n_e{}^2 n_{ia} \tag{5.4}$$

$$\frac{\partial n_{is}}{\partial t} + \nabla\cdot(n_{is}u) = k_{fs}n_e n_s - k_{rs}n_e{}^2 n_{is} \tag{5.5}$$

$$n_e = n_{ia} + n_{is} \tag{5.6}$$

$$\frac{\partial}{\partial t}\{n_{ia}(\frac{3}{2}kT_e + \varepsilon_{ia}) + n_{is}(\frac{3}{2}kT_e + \varepsilon_{is})\}$$

$$+ \nabla \cdot [\{n_{ia}(\frac{3}{2}kT_e + \varepsilon_{ia}) + n_{is}(\frac{3}{2}kT_e + \varepsilon_{is})\} u_e]$$

$$= J \cdot E^* - \nabla \cdot (p_e u_e) - \frac{3}{2}\delta n_e m_e k(T_e - T)$$

$$\times (\frac{\nu_a}{m_a} + \frac{\nu_s}{m_s} + \frac{\nu_{ia}}{m_a} + \frac{\nu_{is}}{m_s}) \qquad (5.7)$$

where

$$\sigma = \frac{e^2 n_e}{m_e \nu_e} \qquad (5.8)$$

$$\beta = \frac{eB}{m_e \nu_e}. \qquad (5.9)$$

5.4 Assumptions

5.4.1 Gasdynamic quantities and assumptions for them

For the numerical analysis of the current distribution in the disk generator channel, the distributions of the gasdynamic quantities in the channel must be given. Therefore, as well as in Subsection 2.4.1, let us find the distributions of them by the quasi-one-dimensional analysis without magnetic field in the steady state.

As mentioned in Subsection 2.4.1, the conservation laws of mass, momentum and energy of the working fluid are given by the following equations

$$\nabla \cdot (\rho u) = 0 \qquad (5.10)$$

$$\rho u \cdot \nabla u = -\nabla p \qquad (5.11)$$

$$\rho u \cdot \nabla (h + \frac{u^2}{2}) = 0 \qquad (5.12)$$

respectively, where

$$p = \rho RT \qquad (5.13)$$

$$h = c_p T. \tag{5.14}$$

Next, for simplifying the calculation, the following two assumptions are introduced.

(1) Gas velocity u has only r component u_r.

(2) All gasdynamic quantities change only in the r direction.

Under the above assumptions, Eqs. (5.10) to (5.12) are reduced into the following quasi-one-dimensional equations.

$$\frac{d}{dr}(\rho u_r A) = 0 \tag{5.15}$$

$$\rho u_r \frac{du_r}{dr} + \frac{dp}{dr} = 0 \tag{5.16}$$

$$\rho u_r \frac{d}{dr}(h + \frac{u_r^2}{2}) = 0 \tag{5.17}$$

By the similar process mentioned in Subsection 2.4.1, the following equations are obtained from the above equations.

$$\rho u_r = \text{const.} \tag{5.18}$$

$$c_p T + \frac{u_r^2}{2} = \text{const.} \tag{5.19}$$

$$\frac{\rho u_r}{\gamma}(1 - \frac{1}{M^2})\frac{du_r}{dr} = 0 \tag{5.20}$$

Eq. (5.20) tells that the gas velocity u_r is constant all over the channel except the case of $M = 1$. Therefore, the velocity of heavy particle is assumed to be constant all over the channel and has only r component u_r. Moreover, considering Eqs. (5.18) and (5.19), all the gasdynamic quantities take the constant values all over the channel in this analysis.

5.4.2 Other assumptions

To simplify the basic equations and obtain the two-dimensional basic equations, the following assumptions are introduced.

(1) The magnetic flux density is constant in space and time and

has the form

$$B = (0, 0, B). \tag{5.21}$$

(2) All quantities are constant in z direction, namely

$$\frac{\partial}{\partial z} = 0. \tag{5.22}$$

(3) The term $\nabla p_e/en_e$ in generalized Ohm's law is negligible.

5.5 Simplified Two-Dimensional Basic Equations

Considering the above assumptions, Eq. (5.1) is reduced to

$$J_r = \frac{\sigma}{1 + \beta^2}\{E_r - \beta(E_\theta - u_r B)\} \tag{5.23}$$

$$J_\theta = \frac{\sigma}{1 + \beta^2}\{\beta E_r + (E_\theta - u_r B)\} \tag{5.24}$$

where the suffixes r and θ show the r and θ components, respectively, of any vector quantity. Also, Eq. (5.2) and (5.3) are reduced to the following two-dimensional equations

$$\frac{1}{r}\frac{\partial}{\partial r}(rE_\theta) - \frac{1}{r}\frac{\partial}{\partial \theta}(E_r) = 0 \tag{5.25}$$

$$\frac{1}{r}\frac{\partial}{\partial r}(h_z r J_r) + \frac{1}{r}\frac{\partial}{\partial \theta}(h_z J_\theta) = 0 \tag{5.26}$$

where h_z is the height of the channel. Furthermore, to decrease the number of unknown variables, the electric potential φ defined by

$$E_r = -\frac{\partial \varphi}{\partial r}, \qquad E_\theta = -\frac{1}{r}\frac{\partial \varphi}{\partial \theta} \tag{5.27}$$

is introduced. Eq. (5.25) is satisfied always by Eq. (5.27) and by using Eqs. (5.23), (5.24) and (5.27), Eq. (5.26) is transformed into the following equation

$$\frac{1}{r}\frac{\partial}{\partial r}\{h_z r \frac{\sigma}{1 + \beta^2}(-\frac{\partial \varphi}{\partial r} + \beta\frac{1}{r}\frac{\partial \varphi}{\partial \theta} + \beta u_r B)\}$$

$$+ \frac{1}{r}\frac{\partial}{\partial \theta}\{h_z \frac{\sigma}{1 + \beta^2}(-\beta\frac{\partial \varphi}{\partial r} - \frac{1}{r}\frac{\partial \varphi}{\partial \theta} - u_r B)\}$$

$$= 0. \tag{5.28}$$

Next, using the assumptions mentioned in Subsection 5.4.1, Eqs. (5.4) and (5.5) are reduced to

$$\frac{\partial n_{ia}}{\partial t} = \dot{n}_{ia} - u_r \frac{\partial n_{ia}}{\partial r} \tag{5.29}$$

$$\frac{\partial n_{is}}{\partial t} = \dot{n}_{is} - u_r \frac{\partial n_{is}}{\partial r} \tag{5.30}$$

where $\dot{n}_{ia}$ and $\dot{n}_{is}$ are defined as follows:

$$\dot{n}_{ia} = k_{fa} n_e n_a - k_{ra} n_e^2 n_{ia} \tag{5.31}$$

$$\dot{n}_{is} = k_{fs} n_e n_s - k_{rs} n_e^2 n_{is}. \tag{5.32}$$

Moreover, through the processes by which Eq. (2.60) was derived from Eq. (2.29), the following equation is derived from Eq. (5.7)

$$\frac{\partial T_e}{\partial t} = \frac{2}{3kn_e} \frac{J_r^2 + J_\theta^2}{\sigma} - \delta m_e (T_e - T)\left(\frac{\nu_a}{m_a} + \frac{\nu_s}{m_s} + \frac{\nu_{ia}}{m_a} + \frac{\nu_{is}}{m_s}\right)$$

$$-\left(T_e + \frac{2\varepsilon_{ia}}{3k}\right)\frac{\dot{n}_{ia}}{n_e} - \left(T_e + \frac{2\varepsilon_{is}}{3k}\right)\frac{\dot{n}_{is}}{n_e}. \tag{5.33}$$

By the above-mentioned, Eqs. (5.6), (5.23), (5.24), (5.27) to (5.30) and (5.33) are the basic equations to be solved.

5.6 Boundary Conditions

In this section, the boundary conditions used in this numerical analysis are presented. In the disk generator shown in Fig. 5.1, there exist two boundaries, namely the anode and the cathode. These electrodes have three-dimensional configurations. But, as the numerical analysis is performed in the two-dimensional r-θ plane, it is assumed that the anode and the cathode consist of perfect conductor which have no width and exist at $r = r_i$ and $r = r_o$ in Fig. 5.1, respectively. Therefore, the boundary conditions are as follows:

$$\varphi = 0 \qquad \text{at} \quad r = r_i \tag{5.34}$$

$$\varphi = V_L = R_L I_L \qquad \text{at} \quad r = r_o \tag{5.35}$$

where R_L, V_L and I_L are the load resistance connected between the electrodes, the load voltage and the load current, respectively.

5.7 Numerical Solution of Two-Dimensional Basic Equations

The numerical solutions used in this analysis are almost similar to those used in Chapter 2. In this connection, as there exist several differences between the equations in Chapter 2 and this chapter, brief explanations about them are given in this section.

5.7.1 Calculation of electric potential

At first, in order to obtain the electric potential φ by solving the partial differential equation (5.28), the finite element method availing the bilinear element in the r-θ plane, which has the widths Δr and $\Delta\theta$, respectively, in the r and θ directions as shown in Fig. 5.2, is used. Then, the potential $\varphi = \varphi(r,\theta)$ at any point $P = P(r,\theta)$ in the element is given by φ_1, φ_2, φ_3 and φ_4, which are the values of φ's at the nodes $1 = 1(r_2,\theta_1)$, $2 = 2(r_2,\theta_2)$, $3 = 3(r_1,\theta_1)$ and $4 = 4(r_1,\theta_2)$ in Fig. 5.2, as follows:

$$\varphi(r,\theta) = \{N(r,\theta)\}^T \{\varphi^e\} \tag{5.36}$$

where

$$\{N(x,y)\} = \{N_1(x,y)\ N_2(x,y)\ N_3(r,\theta)\ N_4(r,\theta)\}^T$$

$$= \frac{1}{S_e}\begin{Bmatrix} -(r - r_1)(\theta - \theta_2) \\ (r - r_1)(\theta - \theta_1) \\ (r - r_2)(\theta - \theta_2) \\ -(r - r_2)(\theta - \theta_1) \end{Bmatrix} \tag{5.37}$$

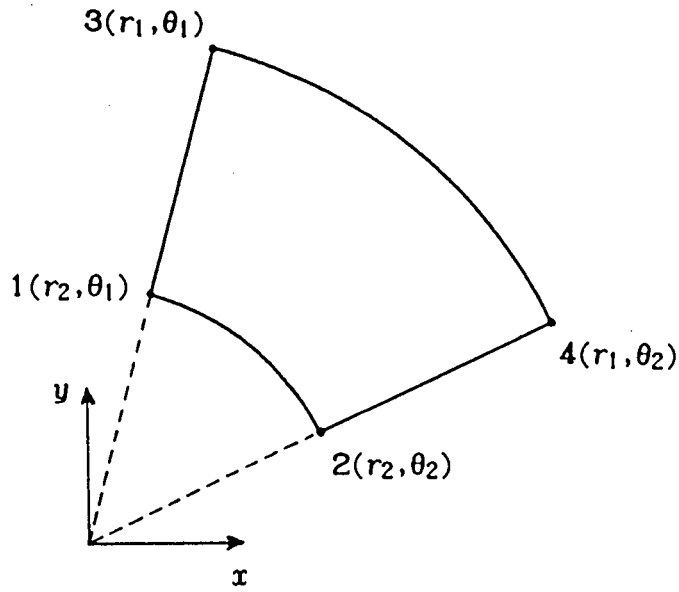

Fig. 5.2 Bilinear element in r-θ plane.

$$S_e = (r_1 - r_2)(\theta_1 - \theta_2) = \Delta r \Delta\theta \tag{5.38}$$

and

$$\{\varphi^e\} = \{\varphi_1 \ \varphi_2 \ \varphi_3 \ \varphi_4\}^T \tag{5.39}$$

in which $N_1(r,\theta)$ to $N_4(r,\theta)$ are the so-called interpolation functions at the nodes 1 to 4, respectively.

Next, as well as in Subsection 2.7.1, the Galerkin process is used for solving Eq. (5.28). Then, the following equation similar to Eq. (2.71) is obtained

$$\iint_S N_i \left[\frac{1}{r}\frac{\partial}{\partial r}\left\{ h_z r \frac{\sigma}{1+\beta^2}\left(-\frac{\partial\varphi}{\partial r} + \beta\frac{1}{r}\frac{\partial\varphi}{\partial\theta} + \beta u_r B\right)\right\} \right.$$

$$\left. + \frac{1}{r}\frac{\partial}{\partial\theta}\left\{ h_z \frac{\sigma}{1+\beta^2}\left(-\beta\frac{\partial\varphi}{\partial r} - \frac{1}{r}\frac{\partial\varphi}{\partial\theta} - u_r B\right)\right\} \right] r dr d\theta$$

$$= 0. \tag{5.40}$$

Applying the integration by parts to the above equation, it is transformed into the following form

$$\iint_S \{h_z \frac{\sigma}{1+\beta^2}\frac{\partial N_i}{\partial r}(-\frac{\partial \varphi}{\partial r} + \beta\frac{1}{r}\frac{\partial \varphi}{\partial \theta} + \beta u_r B)$$

$$+ h_z \frac{\sigma}{1+\beta^2}\frac{1}{r}\frac{\partial N_i}{\partial \theta}(-\beta\frac{\partial \varphi}{\partial r} - \frac{1}{r}\frac{\partial \varphi}{\partial \theta} - u_r B)\} \, r dr d\theta$$

$$- \iint_S [\frac{1}{r}\frac{\partial}{\partial r}\{h_z r \frac{\sigma}{1+\beta^2} N_i(-\frac{\partial \varphi}{\partial r} + \beta\frac{1}{r}\frac{\partial \varphi}{\partial \theta} + \beta u_r B)\}$$

$$+ \frac{1}{r}\frac{\partial}{\partial \theta}\{h_z \frac{\sigma}{1+\beta^2} N_i(-\beta\frac{\partial \varphi}{\partial r} - \frac{1}{r}\frac{\partial \varphi}{\partial \theta} - u_r B)\}] r dr d\theta$$

$$= 0. \qquad (5.41)$$

Furthermore, applying the Gauss' theorem to Eq. (5.41), it becomes

$$\iint_S \{h_z \frac{\sigma}{1+\beta^2}\frac{\partial N_i}{\partial r}(-\frac{\partial \varphi}{\partial r} + \beta\frac{1}{r}\frac{\partial \varphi}{\partial \theta} + \beta u_r B)$$

$$+ h_z \frac{\sigma}{1+\beta^2}\frac{1}{r}\frac{\partial N_i}{\partial \theta}(-\beta\frac{\partial \varphi}{\partial r} - \frac{1}{r}\frac{\partial \varphi}{\partial \theta} - u_r B)\} \, r dr d\theta$$

$$- \oint_C (h_z N_i J_\theta dr + h_z N_i J_r r d\theta) = 0. \qquad (5.42)$$

By setting up the above equation for all nodes in the analytical region S and summing up these equations, the following equation is obtained by the derivation quite similar to that of Eq. (2.75)

$$\sum_e (-\iint_{S^e} h_z \frac{\sigma}{1+\beta^2}[\{N_r\}\{N_r\}^T + \frac{1}{r^2}\{N_\theta\}\{N_\theta\}^T$$

$$- \beta\frac{1}{r}\{N_r\}\{N_\theta\}^T + \beta\frac{1}{r}\{N_\theta\}\{N_r\}^T] r dr d\theta \cdot \{\varphi^e\}$$

$$+ \iint_{S^e} h_z \frac{\sigma}{1+\beta^2} u_r B[\beta\{N_r\} - \frac{1}{r}\{N_\theta\}] \, r dr d\theta$$

$$- \oint_{C^e} (h_z \{N\} J_\theta dr + h_z \{N\} J_r r d\theta) = 0 \qquad (5.43)$$

where $\{N_r\}$, $\{N_\theta\}$ represent

$$\{N_r\} = \{\frac{\partial N}{\partial r}\} = \frac{1}{S_e}\begin{Bmatrix} -(\theta - \theta_2) \\ (\theta - \theta_1) \\ (\theta - \theta_2) \\ -(\theta - \theta_1) \end{Bmatrix} \tag{5.44}$$

$$\{N_\theta\} = \{\frac{\partial N}{\partial \theta}\} = \frac{1}{S_e}\begin{Bmatrix} -(r - r_1) \\ (r - r_1) \\ (r - r_2) \\ -(r - r_2) \end{Bmatrix} \tag{5.45}$$

respectively.

From Eq. (5.43), the following set of simultaneous equations can be derived

$$\sum_e ([K^e]\ \{\varphi^e\} - \{F_1{}^e\} - \{F_2{}^e\}) = 0 \tag{5.46}$$

where

$$[K^e] = -\int\int_{S^e} h_z \frac{\sigma}{1 + \beta^2} [\ \{N_r\}\ \{N_r\}^T + \frac{1}{r^2}\{N_\theta\}\ \{N_\theta\}^T$$

$$- \beta\frac{1}{r}\{N_r\}\ \{N_\theta\}^T + \beta\frac{1}{r}\{N_\theta\}\ \{N_r\}^T] r dr d\theta \tag{5.47}$$

$$\{F_1{}^e\} = -\int\int_{S^e} h_z \frac{\sigma}{1 + \beta^2} u_r B[\beta\{N_r\} - \frac{1}{r}\{N_\theta\}]\ r dr d\theta \tag{5.48}$$

$$\{F_2{}^e\} = \oint_{C^e} (h_z\{N\}\ J_\theta dr + h_z\{N\}\ J_r r d\theta). \tag{5.49}$$

Accordingly, by solving the above set of simultaneous equations, the electrical potential φ at every node is obtained.

In this analysis, dimensions of an element is chosen as Δr = 0.5 mm, $\Delta\theta = \pi/20$ and Eq. (5.46) is solved by Gaussian elimination.

5.7.2 Calculation of ion and electron densities

The argon, the seed and the electron densities n_{ia}, n_{is} and n_e, respectively, are obtained by solving Eqs. (5.6), (5.29) and (5.30). On the characteristic curves given by the following equations

$$\frac{dr}{dt} = u_r \tag{5.50}$$

$$\frac{d\theta}{dt} = 0 \tag{5.51}$$

Eqs. (5.29) and (5.30) have the following forms

$$\frac{dn_{ia}}{dt} = \dot{n}_{ia} \tag{5.52}$$

$$\frac{dn_{is}}{dt} = \dot{n}_{is} \tag{5.53}$$

respectively. These equations can be solved by the Runge-Kutta method.

5.7.3 Calculation of electron temperature

The electron temperature T_e is obtained by numerically solving Eq. (5.33). By the similar process mentioned in Subsection 2.7.3, Eq. (5.33) is reduced to the following form

$$\frac{2}{3kn_e}\frac{J_r^2 + J_\theta^2}{\sigma} - \delta m_e(T_e - T)\left(\frac{\nu_a}{m_a} + \frac{\nu_s}{m_s} + \frac{\nu_{ia}}{m_a} + \frac{\nu_{is}}{m_s}\right)$$

$$-\left(T_e + \frac{2\varepsilon_{ia}}{3k}\right)\frac{\dot{n}_{ia}}{n_e} - \left(T_e + \frac{2\varepsilon_{is}}{3k}\right)\frac{\dot{n}_{is}}{n_e} = 0. \tag{5.54}$$

From this equation, T_e can be obtained by the Newton-Raphson method. In this connection, the time step $\Delta t = 0.25\ \mu s$ is chosen for the numerical calculation by the Runge-Kutta method.

5.7.4 Calculation of current stream function

To study the current distribution in the channel, the current stream function Ψ is useful. In this analysis, considering the channel height h_z, it is defined as

$$J_r = \frac{1}{h_z}\frac{1}{r}\frac{\partial \Psi}{\partial \theta} \tag{5.55}$$

$$J_\theta = -\frac{1}{h_z}\frac{\partial \Psi}{\partial r} \tag{5.56}$$

which satisfy Eq. (5.26). By integrating Eqs. (5.55) and (5.56), Ψ

can be obtained.

5.7.5 Flow chart

In this calculation, the same flow chart shown in Fig. 2.3 is used. The calculation processes are as follows:

(1) The channel size, the load resistance, the magnetic flux density, the gasdynamic conditions and the initial value of electron density are provided.

(2) The conductivity σ and the Hall parameter β in each element are calculated by Eqs. (5.8) and (5.9).

(3) By using the finite element method, the electric potential φ on each node is calculated.

(4) The electric fields E_r and E_θ in each element are calculated by Eq. (5.27).

(5) The current densities J_r and J_θ in each element are calculated by Eqs. (5.23) and (5.24).

(6) By using Newton-Raphson method, the electron temperature T_e in each element is calculated by Eq. (5.54).

(7) The processes (2) to (6) are iterated till T_e in all elements are converged.

(8) The current stream function Ψ on each node is calculated by Eqs. (5.55) and (5.56).

(9) By Runge-Kutta method, the electron density n_e in each element at the next time step $t = t + \Delta t$ is calculated by Eqs. (5.6), (5.52) and (5.53).

(10) The processes (2) to (9) are iterated till $t = t_{max}$, where t_{max} is the calculation interval needed to investigate the transient response of the current distribution in the channel.

5.8 Concluding Remarks

The main conclusions obtained in this chapter are as follows:

(1) A two-dimensional model of the disk generator channel was

introduced.

(2) Using some inevitable assumptions, the two-dimensional basic equations, by which the electric potential, the electron temperature and the electron density in the channel can be numerically calculated, were derived from the basic equations.

(3) To calculate the electric potential on each node, the finite element method was introduced.

(4) The methods to calculate the electron temperature, the electron density and the current stream function were shown.

(5) The flow chart for solving the above two-dimensional basic equations was shown.

CHAPTER 6

CURRENT DISTRIBUTION IN OUTFLOW DISK GENERATOR

6.1 Introduction

As described in the preceding chapter, by the experimental results by Shioda, et al., it was confirmed that the outflow disk generator has an advantage in stabilizing the plasma over the linear Faraday generator. However, many important unsolved problems still remain about the current distribution in the disk generator because of difficulty of observing it in experiments. Therefore, in this chapter, the transient formation process and the steady state of the current distributions in the disk generator are investigated by using the numerical method introduced in the preceding chapter[45)-(47)].

At first, in this chapter, the transient and the steady current distributions in the disk generator using the cesium seeded argon plasma are studied by the numerical solution obtained in the preceding chapter. The transient formation process of inhomogeneous current distribution is made clear. Also, the features of the distributions of the current, the electron temperature, the electron density, the conductivity and the electric potential in the steady state are clarified. Next, influence of the magnetic flux density on the current distribution is studied. Also, the advantage of the disk generator in stabilizing the plasma in comparison with the linear Faraday generator, which has been known by the previous experiments, is theoretically confirmed by the present analysis.

6.2 Numerical Conditions

In this chapter, the cesium seeded argon plasma is considered as the working plasma. The values of the anode and cathode radius r_i and r_o, the channel cross section A, the channel width at the anode h_i, the stagnation and static temperatures of the gas T_s and T, the stagnation and static pressures p_s and p, the Mach number M,

Table 6.1 Numerical conditions used in calculations.

Anode radius	r_i	40 mm
Cathode radius	r_o	80 mm
Channel cross section	A	2513 mm^2
Channel height at anode	h_i	10 mm
Stagnation temperature	T_s	2000 K
Static temperature	T	1040 K
Stagnation pressure	p_s	6.2 atm
Static pressure	p	1.2 atm
Mach number	M	1.6644
Gas velocity	u_r	1000 m/s
Argon number density	n_{a0}	8.47×10^{24} m^{-3}
Magnetic flux density	B	3 T, 2 T, 1 T
Seed fraction	ε	2×10^{-4}, 10^{-4}, 5×10^{-5}
Load resistance	R_L	2 Ω
Dimension of element	Δr	0.5 mm
Dimension of element	$\Delta\theta$	$\pi/20$
Time step	Δt	0.25 μs

the gas velocity u_r, the argon number density n_{a0}, the magnetic flux density B, the seed fraction ε, the load resistance R_L, the dimensions of one element Δr and $\Delta\theta$, the time step Δt used in this and the next chapters are shown in Table 6.1.

6.3 Transient Formation Process and Steady State of Inhomogeneous Current Distribution[48]

Numerical analysis is performed to clarify the transient formation process and the steady state of the inhomogeneous current distribution. In the analysis in this section, the magnetic flux density B = 1 T, the seed fraction $\varepsilon = 2 \times 10^{-4}$ and the load resistance R_L = 2 Ω in Table 6.1 are chosen. Here, the initial condition is assumed that for $t<0$ only the argon is supplied in the channel and for $t \geqq 0$ the cesium seeded argon plasma is done.

First, the calculated transient current distributions in the channel from t = 5 μs to 80 μs are shown in Figs. 6.1(a) and (b), where $\Delta\Psi$ represents the contour interval of the current streamlines. The figures show that a region of the very high current density is formed around the anode and it moves downstream at the speed equal to that of the working plasma. At $t \fallingdotseq 40$ μs the region arrives at the cathode. The figures at t = 30 to 80 μs denote that inside the region, spiral shaped streamers are developed and the current distribution is very inhomogeneous. Also at t = 70 to 80 μs, the region of the high current density flows out from the cathode, and then the current distribution in the channel attains to a steady state.

The above results tell that the streamers in the channel move at the speed equal to the one of the plasma in not only the linear Faraday generator channel but also the disk generator channel. These calculated results agree with the experimental ones[49]. The above results tell that the origin of the inhomogeneous current distribution in the channel is the ionization instability of the

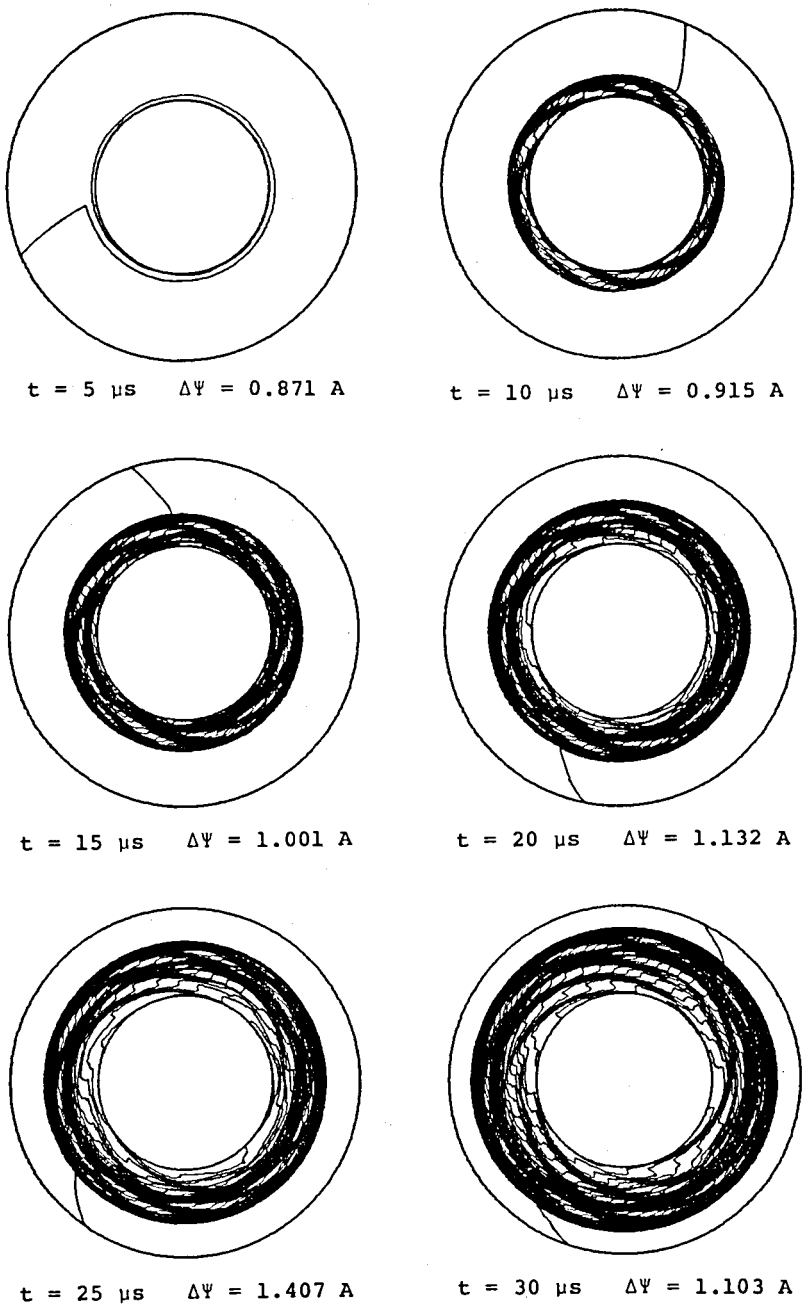

Fig. 6.1(a) Transient current distributions for $B = 1$ T, $\varepsilon = 2 \times 10^{-4}$ and $R_L = 2\ \Omega$.

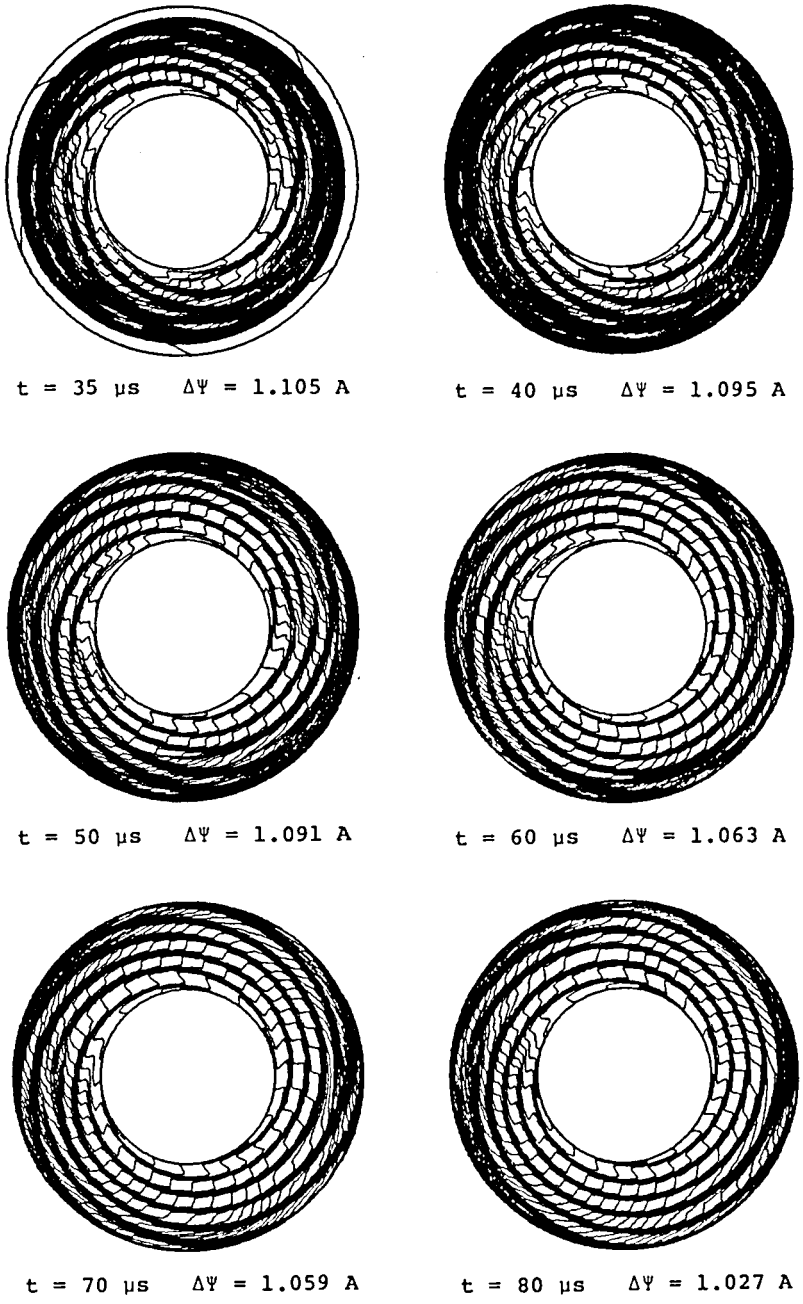

Fig. 6.1(b) Transient current distributions for $B = 1$ T, $\varepsilon = 2 \times 10^{-4}$ and $R_L = 2\ \Omega$.

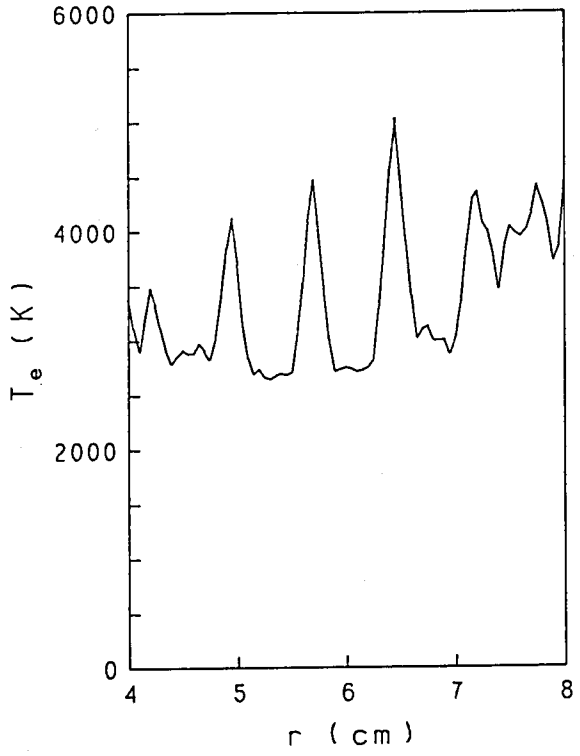

Fig. 6.2 Electron temperature distribution in r direction at t = 80 μs for B = 1 T, $\varepsilon = 2 \times 10^{-4}$ and R_L = 2 Ω.

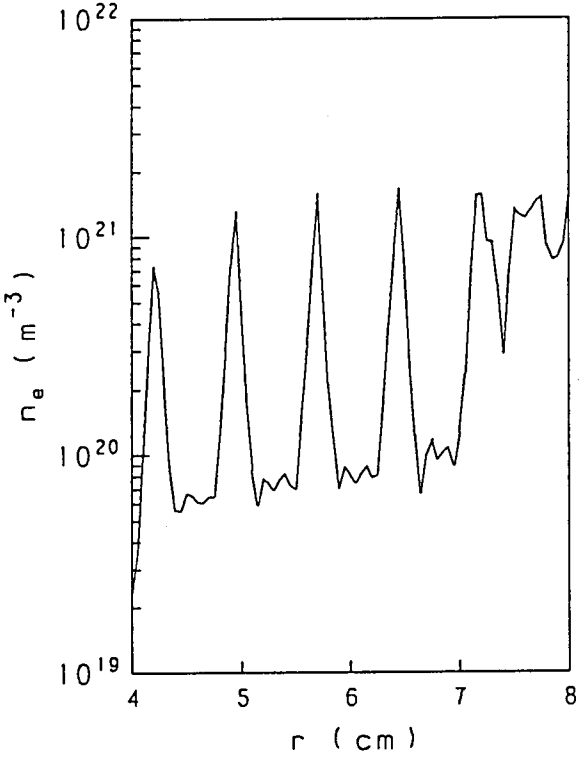

Fig. 6.3 Electron density distribution in r direction at t = 80 μs for B = 1 T, $\varepsilon = 2 \times 10^{-4}$ and R_L = 2 Ω.

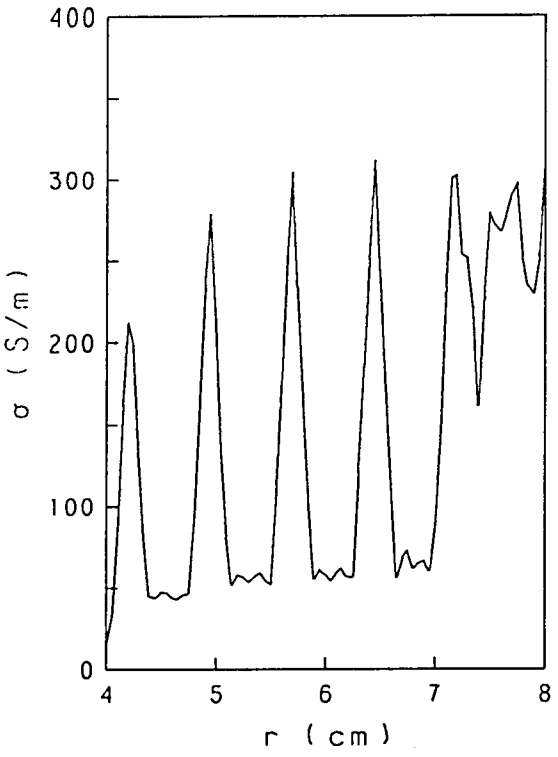

Fig. 6.4 Conductivity distribution in r direction at t = 80 μs for B = 1 T, $\varepsilon = 2 \times 10^{-4}$ and R_L = 2 Ω.

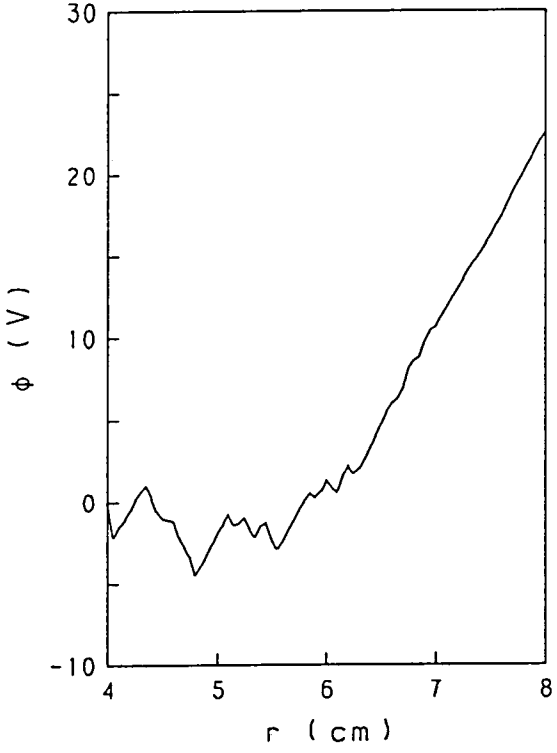

Fig. 6.5 Electric potential distribution in r direction at t = 80 μs for B = 1 T, $\varepsilon = 2 \times 10^{-4}$ and R_L = 2 Ω.

plasma and another main factor which determines the current one in the steady state is the convection effect of the plasma in not only the linear channel but also the disk channel.

Next, Figures 6.2 to 6.5 show the steady distributions of the electron temperature T_e, the electron density n_e, the conductivity σ and the electric potential φ in the radial direction on $\theta = 0$ at $t = 80$ μs, respectively. Figures 6.2 to 6.4 tell that T_e, n_e and σ take high values in the streamers, in which $T_e \fallingdotseq 4000$ K and $n_e > 10^{21}$ m^{-3}. As 4000 K $< T_e <$ 6500 K and $n_e \fallingdotseq 1.7 \times 10^{21}$ m^{-3} in the case of fully ionized seed for the present plasma, it is seen that the seed is fully ionized in the streamers. Figure 6.5 denotes that the first half of the channel is the inlet relaxation region and almost all power is generated in the latter half of the channel. Accordingly, the inlet relaxation region influences considerably on the output power of the generator.

6.4 Influence of Magnetic Flux Density on Current Distribution

In order to clarify the influences of the magnetic flux density on the current distribution, numerical calculations are performed for five different magnetic flux densities, namely $B = 1.5$, 2, 2.5, 3 and 4 T, where the seed fraction $\varepsilon = 2 \times 10^{-4}$ and the load resistance $R_L = 2$ Ω are adopted. First, Figure 6.6 shows the current distributions in the steady state, where $t = 80$ μs, for each magnetic flux density. In the figure, the current distribution for $B = 1$ T, which was discussed in the preceding section, is presented again for comparison. From Fig. 6.6, it is made clear that the current distribution is inhomogeneous at $B = 1$ T, but the inhomogeneity disappears with increasing the magnetic flux density and the distribution becomes almost homogeneous at $B = 2$ to 2.5 T. However, it becomes inhomogeneous again at $B = 3$ to 4 T. Now, the above results are considered to indicate that the current distribution in the channel

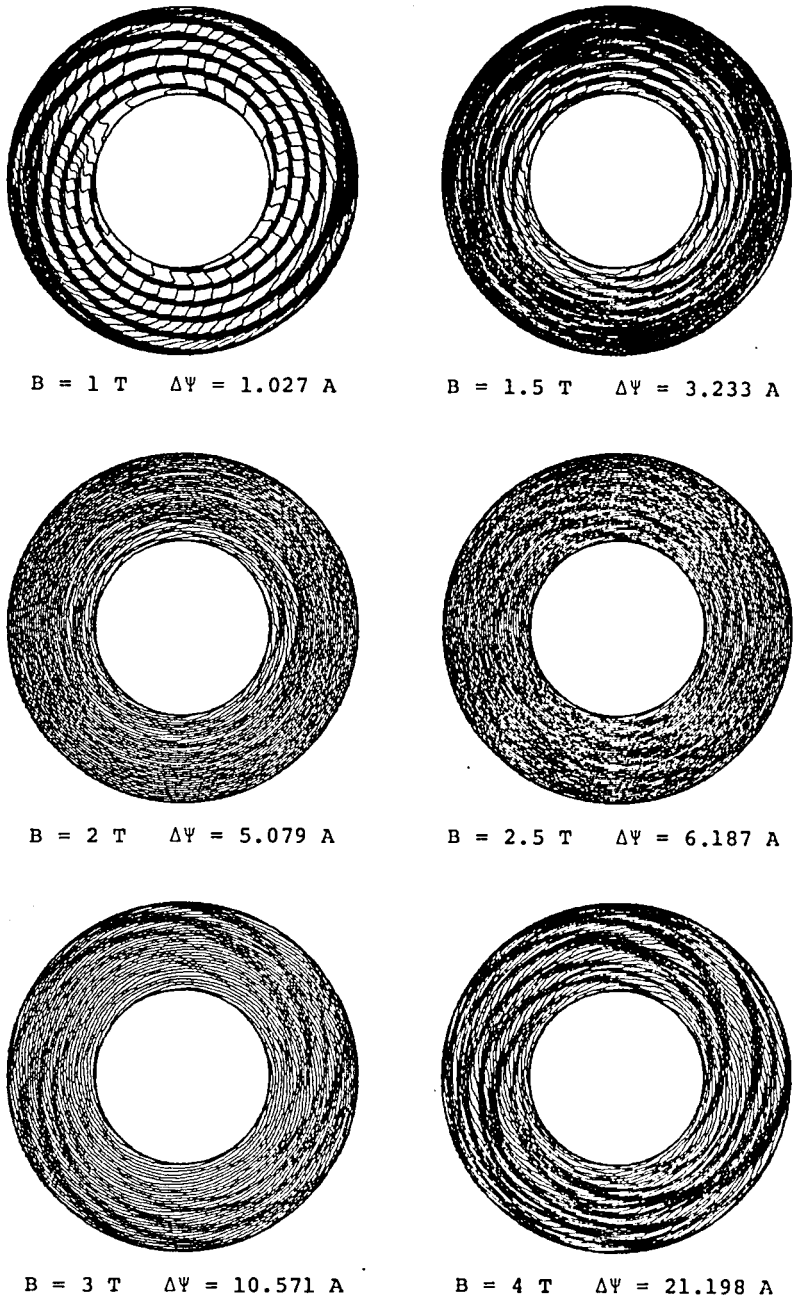

Fig. 6.6 Current distributions at t = 80 μs for various magnetic flux densities for $\varepsilon = 2 \times 10^{-4}$ and R_L = 2 Ω.

at B = 1 to 1.5 T is made inhomogeneous by the ionizaton instability of the plasma, because the cesium is not fully ionized. It becomes homogeneous at B = 2 to 2.5 T because the cesium is fully ionized and so the plasma becomes stable. Furthermore, at B = 3 to 4 T, since the ionization of the argon gas begins to occur in some parts of the channel and so the plasma becomes unstable, the current distribution becomes again inhomogeneous.

In order to confirm the above consideration, let us investigate the distributions of the electron temperature T_e and the electron density n_e in the channel. Figures 6.7 and 6.8 show the distributions of T_e and n_e, respectively, in the radial direction at θ = 0 and t = 80 μs in the cases of B = 1, 2 and 4 T. From the figures, it is made clear that the electron temperature and the electron density increase as the magnetic flux density increases. Although T_e and n_e fluctuate considerably at B = 1 and 4 T, they are almost constant except the region near the channel inlet for B = 2 T. Furthermore, Figure 6.8 tells that the seed is not fully ionized at B = 1 T, it is fully ionized at B = 2 T and the ionization of argon begins at B = 4 T. These indicate the validity of the above consideration.

As already clarified in Chapter 3, the seed is not yet fully ionized at B = 3 T in the linear Faraday generator channel under the similar numerical conditions. This indicates that the seed can be fully ionized and the plasma can be stabilized easily at rather low magnetic flux density in the disk generator. Thus, this numerical analysis could well explain the experimental results[30],[31] that the disk generator possesses an advantage over the linear Faraday generator in stabilizing the plasma in the channel.

6.5 Concluding Remarks

In this chapter, there were performed the two-dimensional

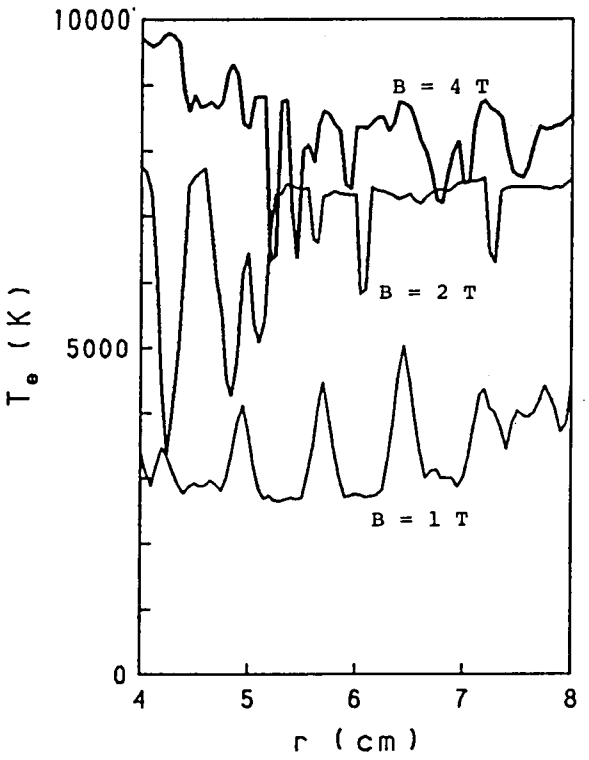

Fig. 6.7 Electron temperature distributions at t = 80 μs for various magnetic flux densities, $\varepsilon = 2 \times 10^{-4}$ and R_L = 2 Ω.

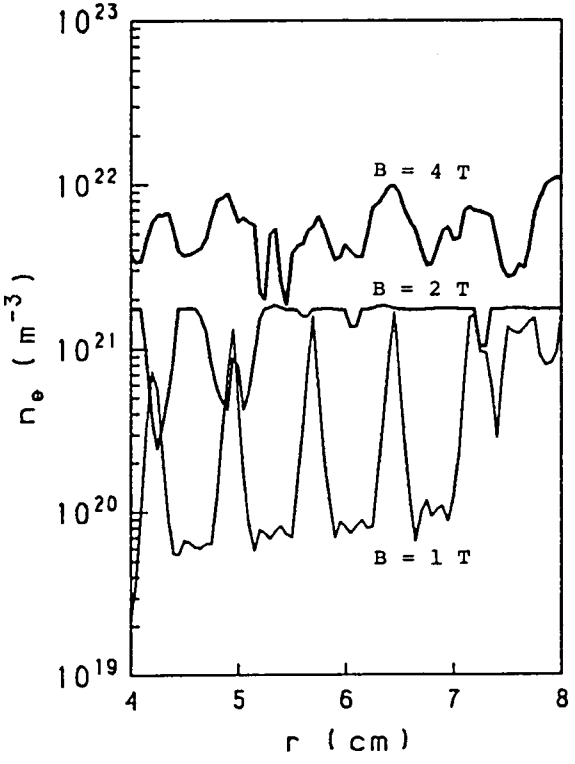

Fig. 6.8 Electron density distributions at t = 80 μs for various magnetic flux densities, $\varepsilon = 2 \times 10^{-4}$ and R_L = 2 Ω.

time-dependent numerical calculations of the current distributions in the disk generator channel by the numerical solution introduced in the preceding chapter and the following results were obtained.

(1) In the transient state, at first, a region of very high current density is formed around the anode and it moves downstream at the speed equal to that of the working plasma. As time goes on, the region of high current density flows out from the cathode, and then the current distribution in the channel attains to a steady state.

(2) In the steady state, the spiral shaped streamers are formed in the disk generator.

(3) The origin of the inhomogeneous current distribution in the channel is the ionization instability of the plasma and another main factor which determines the current one in the steady state is the convection effect of the plasma in not only the linear channel but also the disk channel.

(4) The steady current distribution for low magnetic flux density is inhomogeneous by the ionization instability of the plasma because the seed is not fully ionized. It becomes homogeneous as the magnetic flux density increases, because the seed is fully ionized and the plasma becomes stable. However, increasing the magnetic flux density still more, it becomes again inhomogeneous, because the argon begins to be ionized in some parts of the channel and the plasma becomes unstable.

(5) This numerical analysis could well explain the experimental results that the disk generator possesses an advantage over the linear Faraday generator in stabilizing the plasma in the channel.

CHAPTER 7

PERFORMANCE CHARACTERISTICS OF OUTFLOW DISK GENERATOR

7.1 Introduction

In the preceding chapter, the two-dimensional transient and steady current distributions in the outflow disk generator were made clear. Moreover, it was theoretically clarified that the disk generator has an advantage over the linear Faraday generator in stabilizing the working plasma. On the other hand, it was shown through the experiments[11],[31] that the output voltage of disk generator does not always decrease monotonously as its output current increases and its voltage-current curve often has a peak at a certain value of the load resistance. This is considered to be due to the reason that when all other conditions are fixed and only the load resistance is varied, the plasma in the channel is not always stable for every load resistance. Therefore, in this chapter, the voltage-current characteristics of the disk generator and its other performances concerned with those are studied in detail by using the numerical method mentioned in Chapter 5 and the above consideration is confirmed[47],[50],[51].

At first, the voltage-current curve of the generator using cesium seeded argon plasma (C_s-A_r) is calculated under the typical conditions and the relations between this curve and the average electron density, the current distribution and the other quantities are studied. The influences of the seed fraction and the magnetic flux density on the generator performances are also investigated in detail.

Next, the same performance characteristics of the generator

using potassium seeded argon plasma (K-A_r) are researched, and the differences between the former and the latter performance characteristics are made clear.

7.2 Performance Characteristics of Disk Generator Using Cesium Seeded Argon Plasma

For the numerical calculations in this chapter, the numerical conditions which were shown in Table 6.1 are used.

7.2.1 Generator performances in typical case[52]

At first, to obtain the voltage-current curve for the typical conditions in the case where the cesium seeded argon plasma is used as the working plasma, numerical analyses are performed for various load resistances, where the magnetic flux density B = 3 T and the seed fraction $\varepsilon = 5 \times 10^{-5}$ are adopted. The voltage-current curve by these numerical analyses is shown in Fig. 7.1(a). Since the current distribution in the channel becomes steady by t = 80 μs as mentioned in the preceding chapter, the load voltage and current V_L and I_L at t = 80 μs are adopted to plot the voltage-current curve. The figure shows that, although the load current I_L increases monotonously as the load resistance decreases, the load voltage V_L increases for the load resistance $R_L > 4\ \Omega$ and V_L decreases for $R_L < 4\ \Omega$. It also shows that for $R_L < 1\ \Omega$ V_L decreases rapidly as R_L decreases. This indicates that for $4\ \Omega > R_L > 1\ \Omega$ good generator characteristic is obtained but it is remarkably poor for both $R_L > 4\ \Omega$ and $R_L < 1\ \Omega$.

To make clear the reason for the above deterioration of the generator characteristics, the relation between the load resistance R_L and the average electron density $\bar{n}_e = (\sum_{i=1}^{N} n_{ei})/N$ in the steady state, where t = 80 μs, n_{ei} is the electron density in i-th element and N the number of elements, is shown in Fig. 7.1(b), the electron temperature T_e and the electron density n_e distributions in the

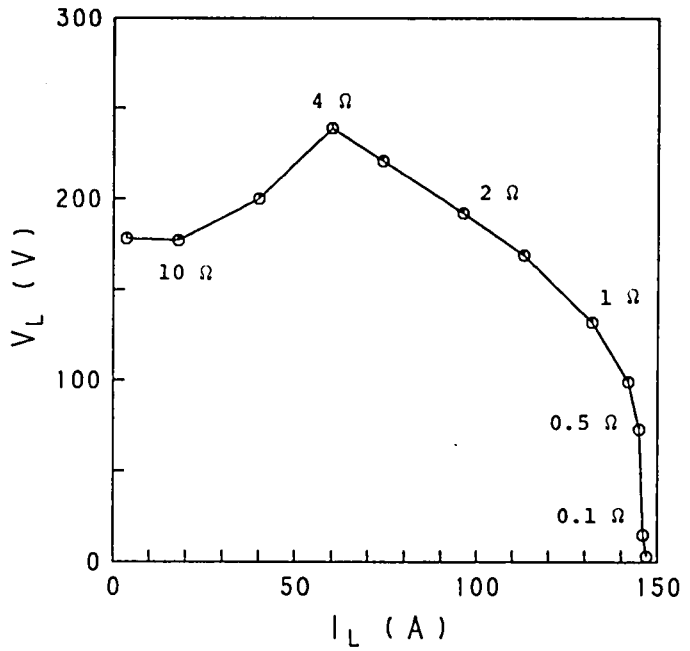

(a) Voltage-current curve.

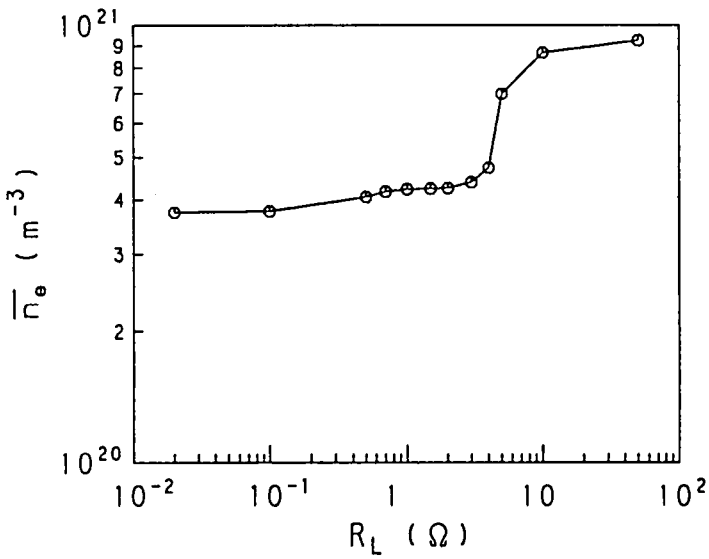

(b) Relation between load resistance and average electron density.

Fig. 7.1 Performance characteristics of generator using C_s-A_r in steady state for B = 3 T and $\varepsilon = 5 \times 10^{-5}$.

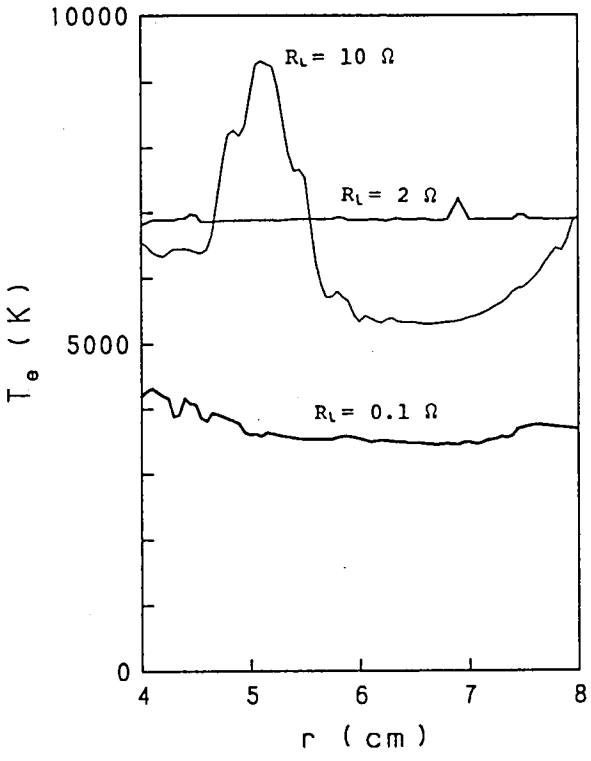

(c) Electron temperature distribution in r direction for various load resistances.

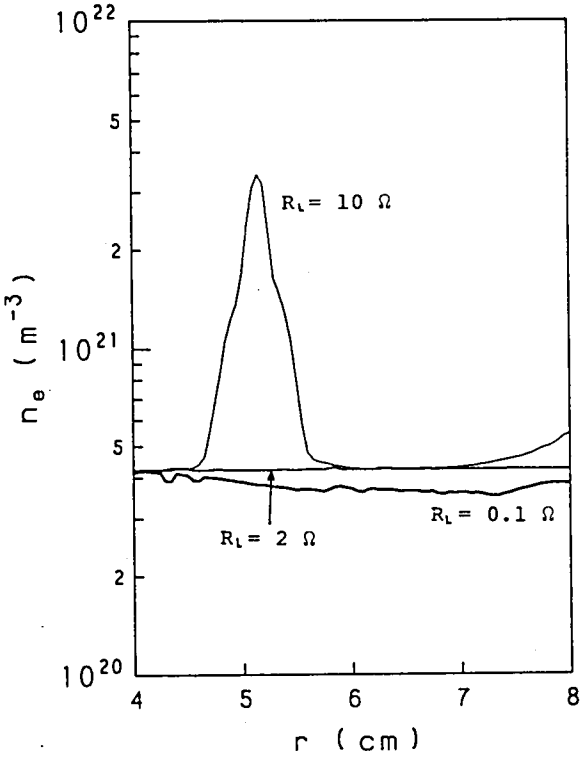

(d) Electron density distribution in r direction for various load resistances.

Fig. 7.1 Performance characteristics of generator using C_s-A_r in steady state for B = 3 T and $\varepsilon = 5 \times 10^{-5}$.

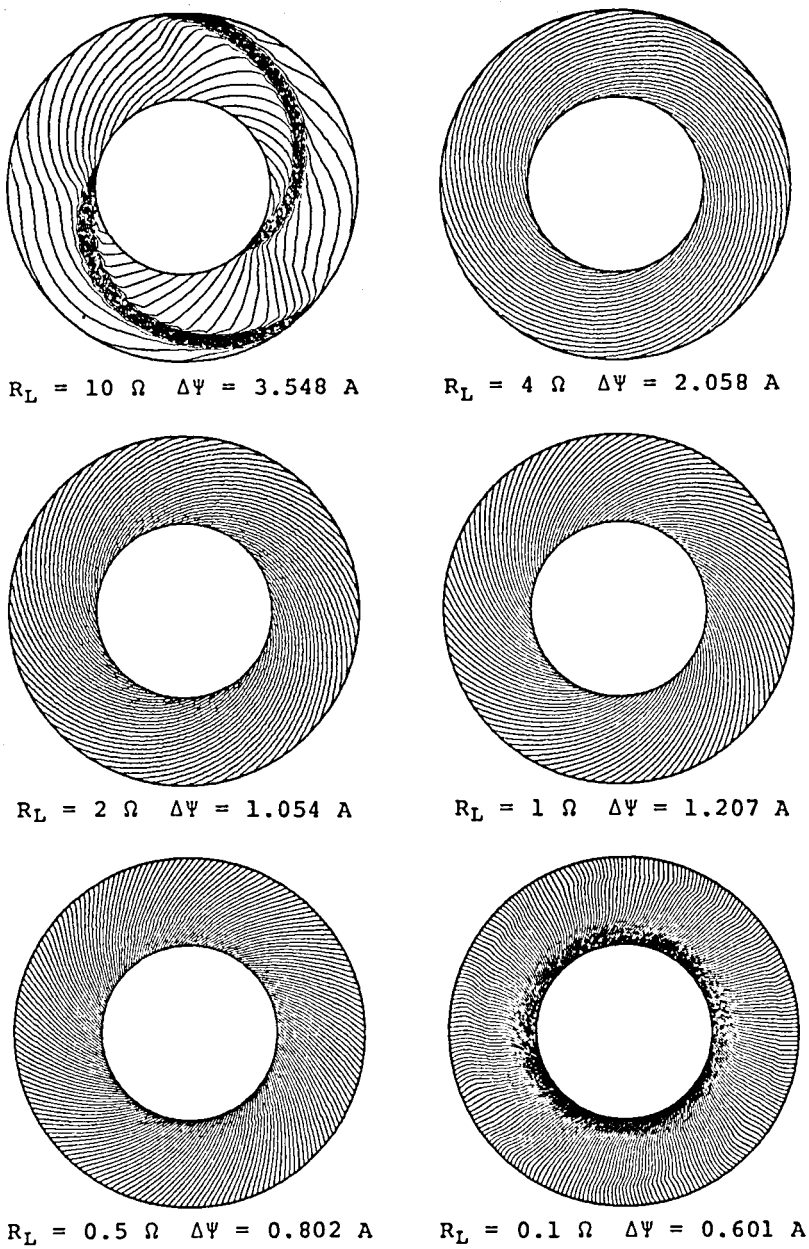

(e) Current distributions for various load resistances.

Fig. 7.1 Performance characteristics of generator using C_s-A_r in steady state for B = 3 T and $\varepsilon = 5 \times 10^{-5}$.

radial direction at t = 80 μs and θ = 0 in the case of R_L = 10, 2 and 0.1 Ω are shown in Figs. 7.1(c) and (d), respectively. The current distributions in the channel at t = 80 μs for R_L = 10, 4, 2, 1, 0.5 and 0.1 Ω are also shown in Fig. 7.1(e). Since the electron density is about 4.24 $\times$ 10^{20} m^{-3} in the case of fully ionized seed for this seed fraction, the figures indicate that the low generator performance for $R_L > 4\ \Omega$ is due to the inhomogeneous current distribution in the channel which is caused by the ionization instability of partially ionized argon. The figures also denote that the current distribution is homogeneous and so the generator performance good for $4\ \Omega > R_L > 1\ \Omega$ because the seed is fully ionized and the plasma in the channel is stable, and the poor generator performance for $R_L < 1\ \Omega$ is due to the inhomogeneous current distribution in the channel which is caused by the ionization instability of partially ionized seed.

The above results can qualitatively well explain the experimental results[11],[31], which could not be explained by the previous researches. Moreover, this numerical analysis makes clear the relation between the current distribution in the channel and the voltage-current characteristics for the first time.

7.2.2 Influence of seed fraction on performance characteristics

In this subsection, to make clear the influences of the seed fraction on the voltage-current characteristics in the steady state, let us study on the cases of two seed fractions $\varepsilon = 10^{-4}$ and 2×10^{-4} in addition to the above case of $\varepsilon = 5 \times 10^{-5}$, where t = 80 μs and the magnetic flux density B = 3 T.

First, in Figs. 7.2(a) to (c), there are shown the voltage-current curve, the relation between the load resistance R_L and the average electron density $\bar{n}_e$ and the current distributions in the channel for R_L = 10, 5, 1, 0.5, 0.1 and 0.05 Ω, respectively, in the case of $\varepsilon = 10^{-4}$. Next, in

Figs. 7.3(a) to (c), there are shown the voltage-current curve, the relation between R_L and $\bar{n}_e$ and the current distributions in the channel for R_L = 10, 2, 1, 0.5, 0.1 and 0.05 Ω, respectively, in the case of $\varepsilon = 2 \times 10^{-4}$. Since the electron density is $n_e \fallingdotseq 8.47 \times 10^{20}$ m^{-3} and $n_e \fallingdotseq 1.69 \times 10^{21}$ m^{-3} for $\varepsilon = 10^{-4}$ and $\varepsilon = 2 \times 10^{-4}$, respectively, in the case of fully ionized seed, Figures 7.2 and 7.3 tell that the plasma in the channel becomes unstable by the ionization instability in both regions of high and low load resistances as same as in the case of $\varepsilon = 5 \times 10^{-5}$. However, the influences of the ionization instability on the voltage-current characteristics of the generator become small as the seed fraction becomes large, and the load voltage decreases monotonously as the load current increases in the case of $\varepsilon = 2 \times 10^{-4}$.

7.2.3 Influence of magnetic flux density on performance characteristics

Here, to make clear the influence of the magnetic flux density on the voltage-current characteristics, let us analyze the case of B = 2 T and $\varepsilon = 5 \times 10^{-5}$. The calculated voltage-current curve is shown in Fig. 7.4(a). This figure show that the generator performance deteriorates for low load resistance but does not deteriorates for high load resistance. It also shows that both the load voltage V_L and so the load current I_L become small and the generator performance extremely worsens near R_L = 2 Ω.

To clarify the reasons for the above deteriorations of the generator performance, the relation between the load resistance R_L and the average electron density $\bar{n}_e$, the electron temperature T_e and the electron density n_e distributions in the radial direction at θ = 0 for R_L = 50, 2 and 0.5 Ω and the current distributions in the channel for R_L = 50, 10, 2, 1, 0.5 and 0.02 Ω in the steady state, where t = 80 μs, are shown in Figs. 7.4(b) to (e), respectively. These figures indicate that the no deterioration of

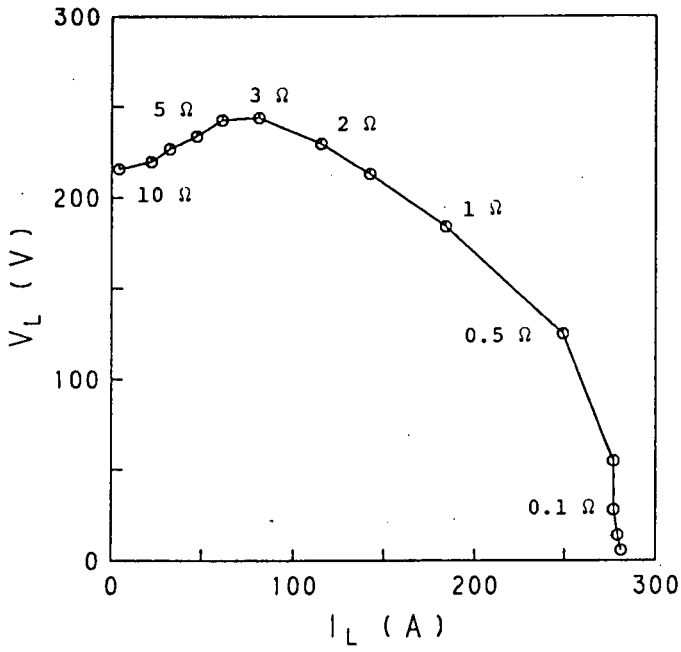

(a) Voltage-current curve.

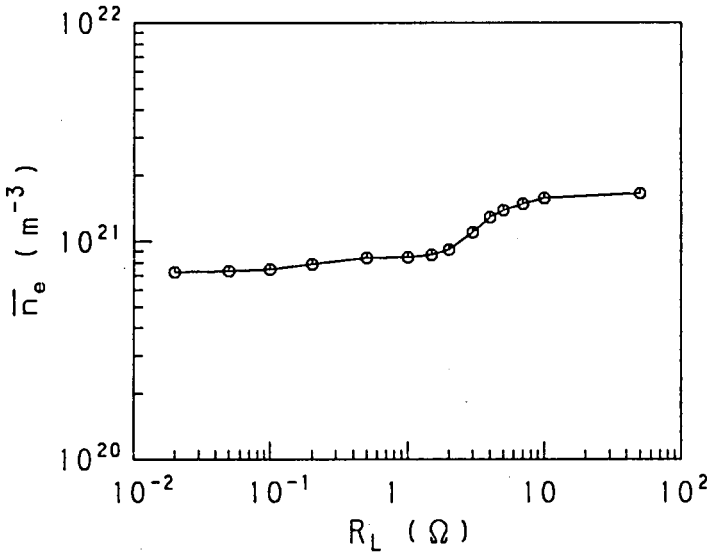

(b) Relation between load resistance and average electron density.

Fig. 7.2 Performance characteristics of generator using C_s-A_r in steady state for B = 3 T and $\varepsilon = 10^{-4}$.

R_L = 10 Ω ΔΨ = 7.310 A

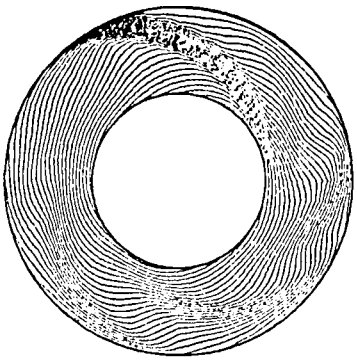

R_L = 5 Ω ΔΨ = 5.207 A

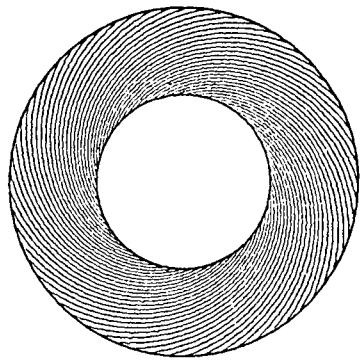

R_L = 1 Ω ΔΨ = 3.017 A

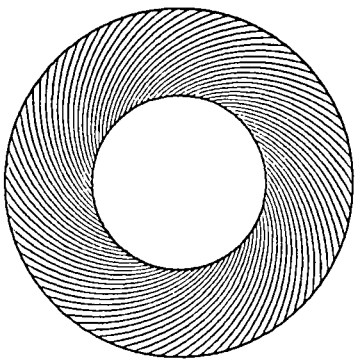

R_L = 0.5 Ω ΔΨ = 3.002 A

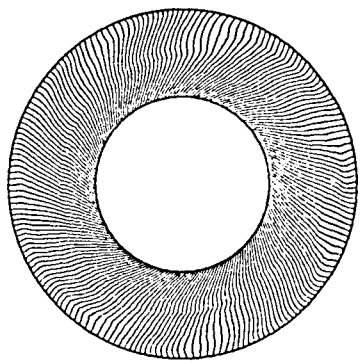

R_L = 0.1 Ω ΔΨ = 1.506 A

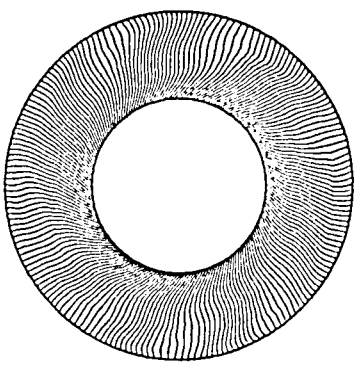

R_L = 0.05 Ω ΔΨ = 1.500 A

(c) Current distributions for various load resistances.

Fig. 7.2 Performance characteristics of generator using C_s-A_r in steady state for B = 3 T and $\varepsilon = 10^{-4}$.

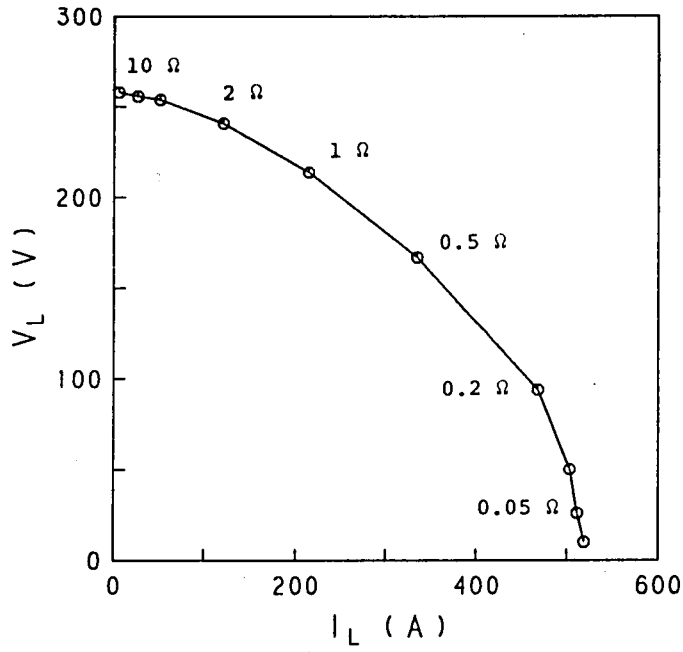

(a) Voltage-current curve.

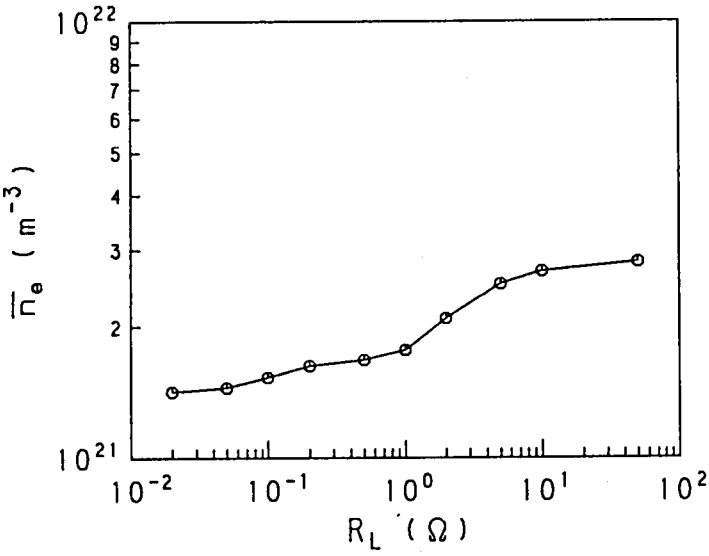

(b) Relation between load resistance and average electron density.

Fig. 7.3 Performance characteristics of generator using C_s-A_r in steady state for B = 3 T and $\varepsilon = 2 \times 10^{-4}$.

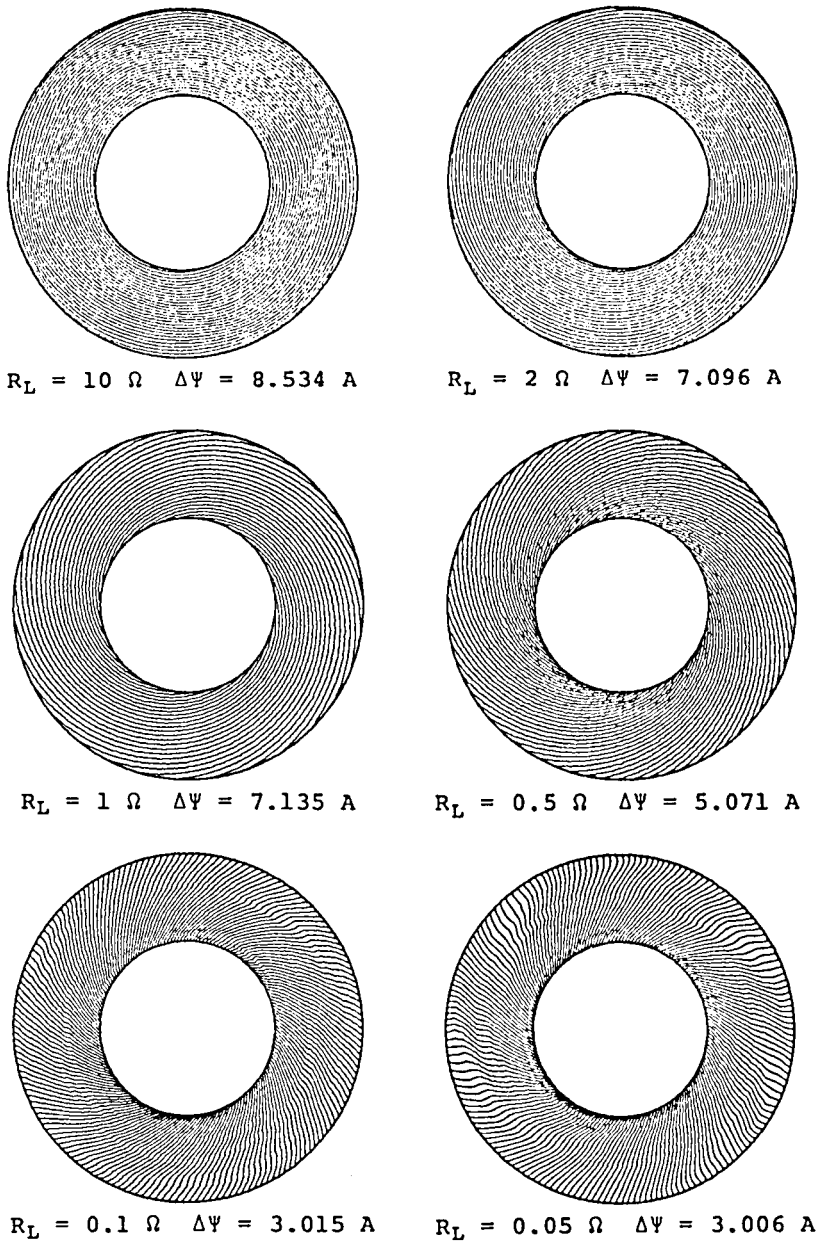

(c) Current distributions for various load resistances.

Fig. 7.3 Performance characteristics of generator using C_s-A_r in steady state for B = 3 T and $\varepsilon = 2 \times 10^{-4}$.

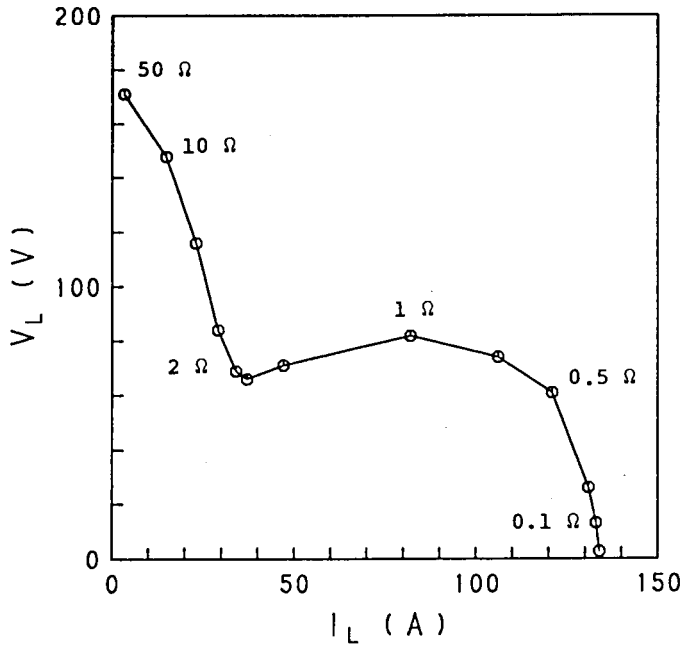

(a) Voltage-current curve.

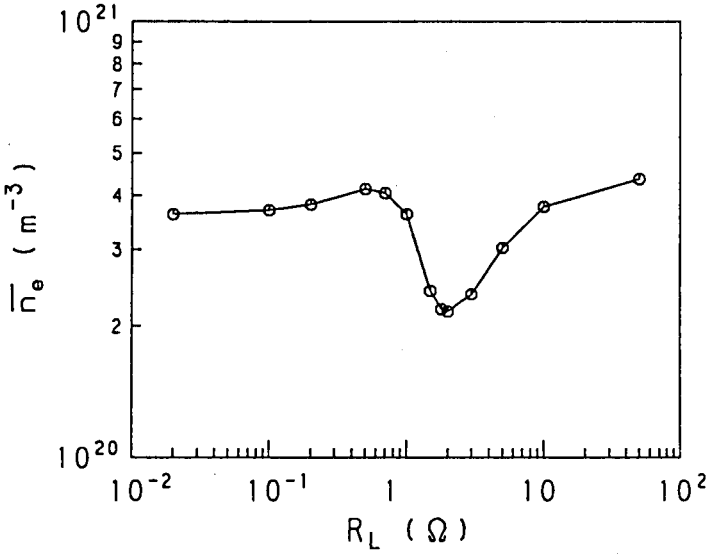

(b) Relation between load resistance and average electron density.

Fig. 7.4 Performance characteristics of generator using C_s-A_r in steady state for B = 2 T and $\varepsilon = 5 \times 10^{-5}$.

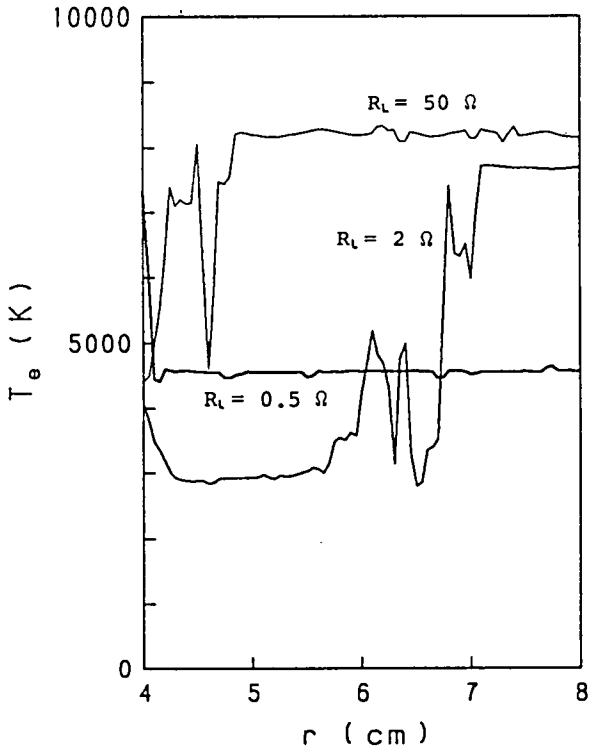

(c) Electron temperature distribution in r direction for various load resistances.

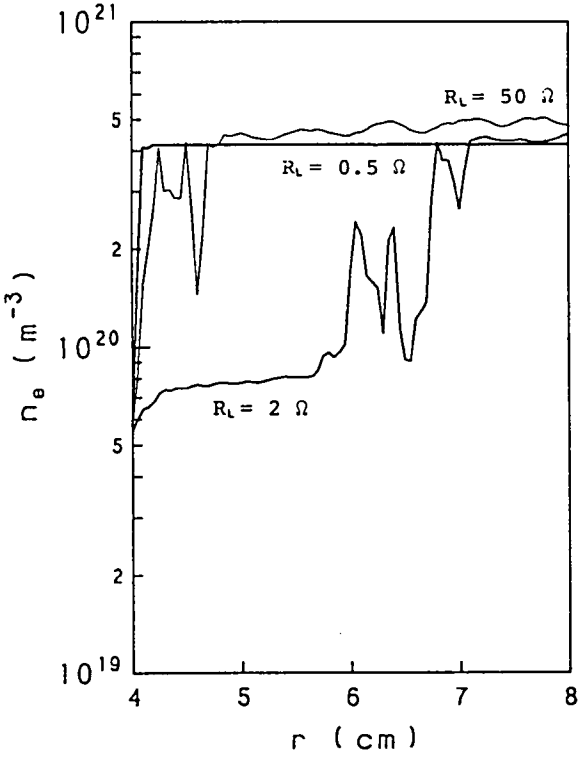

(d) Electron density distribution in r direction for various load resistances.

Fig. 7.4 Performance characteristics of generator using C_s-A_r in steady state for B = 2 T and $\varepsilon = 5 \times 10^{-5}$.

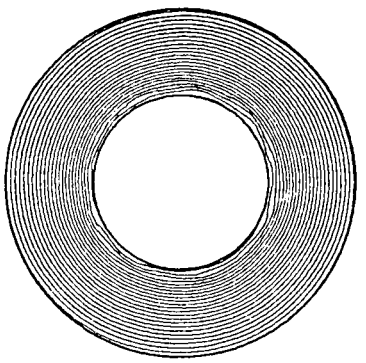

R_L = 50 Ω ΔΨ = 1.707 A

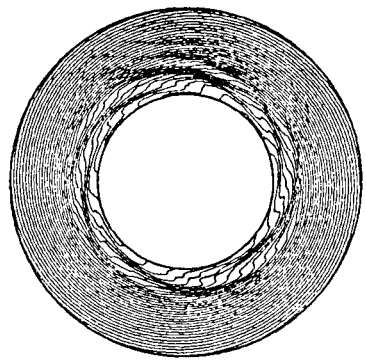

R_L = 10 Ω ΔΨ = 1.059 A

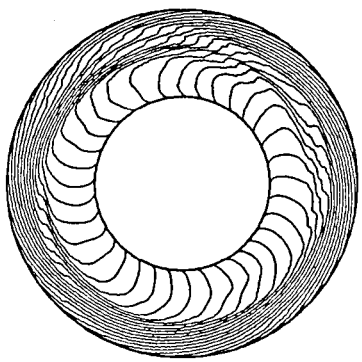

R_L = 2 Ω ΔΨ = 1.010 A

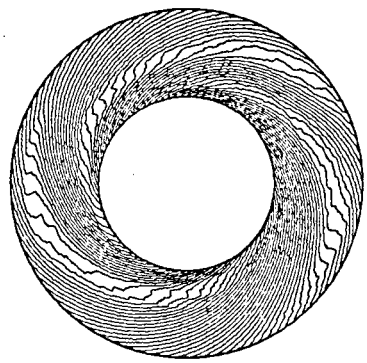

R_L = 1 Ω ΔΨ = 1.008 A

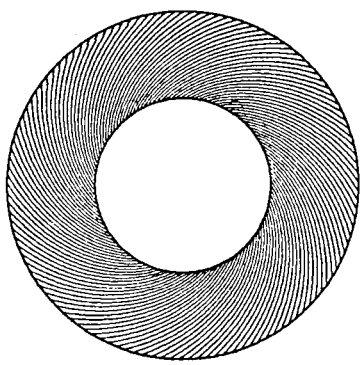

R_L = 0.5 Ω ΔΨ = 1.004 A

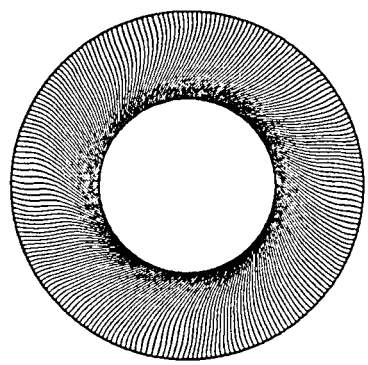

R_L = 0.02 Ω ΔΨ = 0.601 A

(e) Current distributions for various load resistances.

Fig. 7.4 Performance characteristics of generator using C_s-A_r in steady state for B = 2 T and $\varepsilon = 5 \times 10^{-5}$.

the generator performance for high load resistance is due to the fact that the argon does not ionized in the channel because the magnetic flux density is small. The figures also show that the electron temperature, the electron density and the current density in the first half of the channel are much lower than those in the latter half at $R_L = 2\ \Omega$. This means that the inlet relaxation region extends and reaches to the center of the channel at $R_L = 2\ \Omega$. Therefore, the deterioration of the generator performance near $R_L = 2\ \Omega$ is considered to be due to extention of the inlet relaxation region.

As above-mentioned, the main factor which lowers the generator performance is the ionization instability of the plasma when the magnetic flux density B is large, but the length of the inlet relaxation region much influences the generator performance when B is small.

7.3 Performance Characteristics of Disk Type Generator Using Potassium Seeded Argon Plasma

In this section, numerical analysis is performed for the case where the potassium seeded argon plasma is used, and the performance characteristics of the generator using the cesium seeded argon plasma described in the preceding section and those of the generator using the potassium seeded argon plasma are compared. For this purpose, the magnetic flux density is chosen as $B = 3$ T and calculations are carried out for three different seed fractions of potassium, namely $\varepsilon = 5 \times 10^{-5}$, 10^{-4} and 2×10^{-4}. In the calculations, all other conditions are chosen as same as used in the preceding section.

The voltage-current curves, the relations between the load resistance R_L and the average electron density $\bar{n}_e$ and the current distributions for six different load resistances in the steady state, where $t = 80\ \mu$s, are shown in Figs. 7.5 (a) to (c),

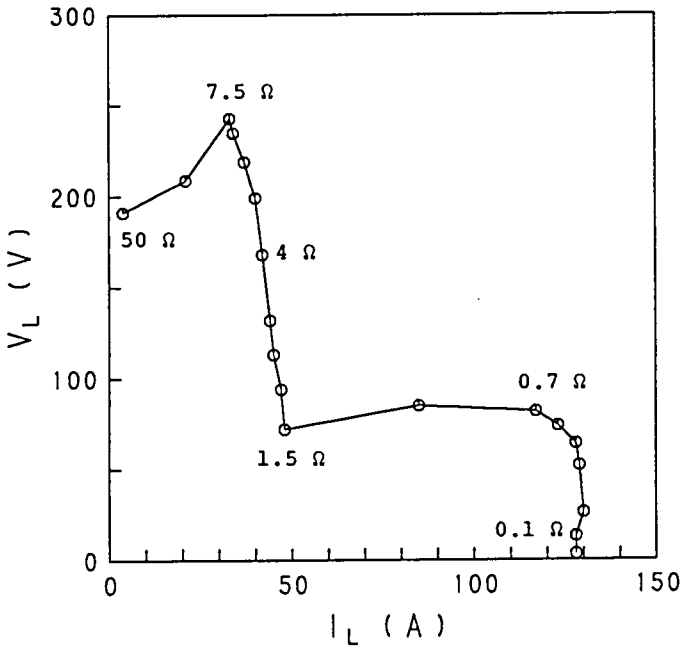

(a) Voltage-current curve.

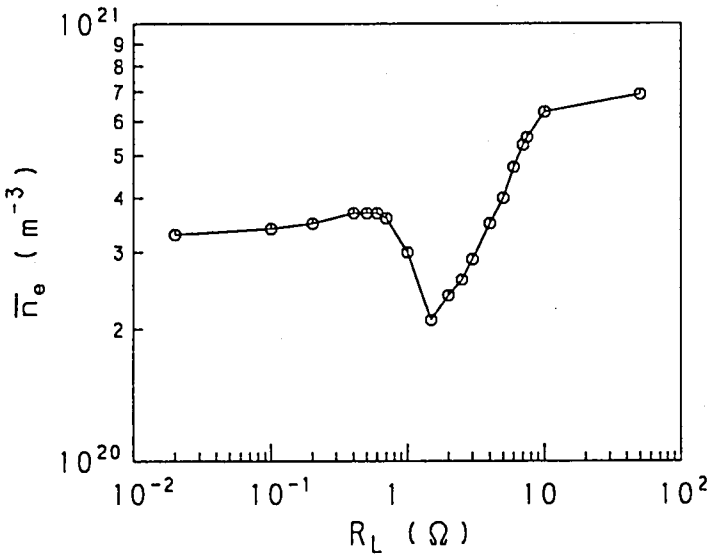

(b) Relation between load resistance and average electron density.

Fig. 7.5 Performance characteristics of generator using K-A_r in steady state for B = 3 T and $\varepsilon = 5 \times 10^{-5}$.

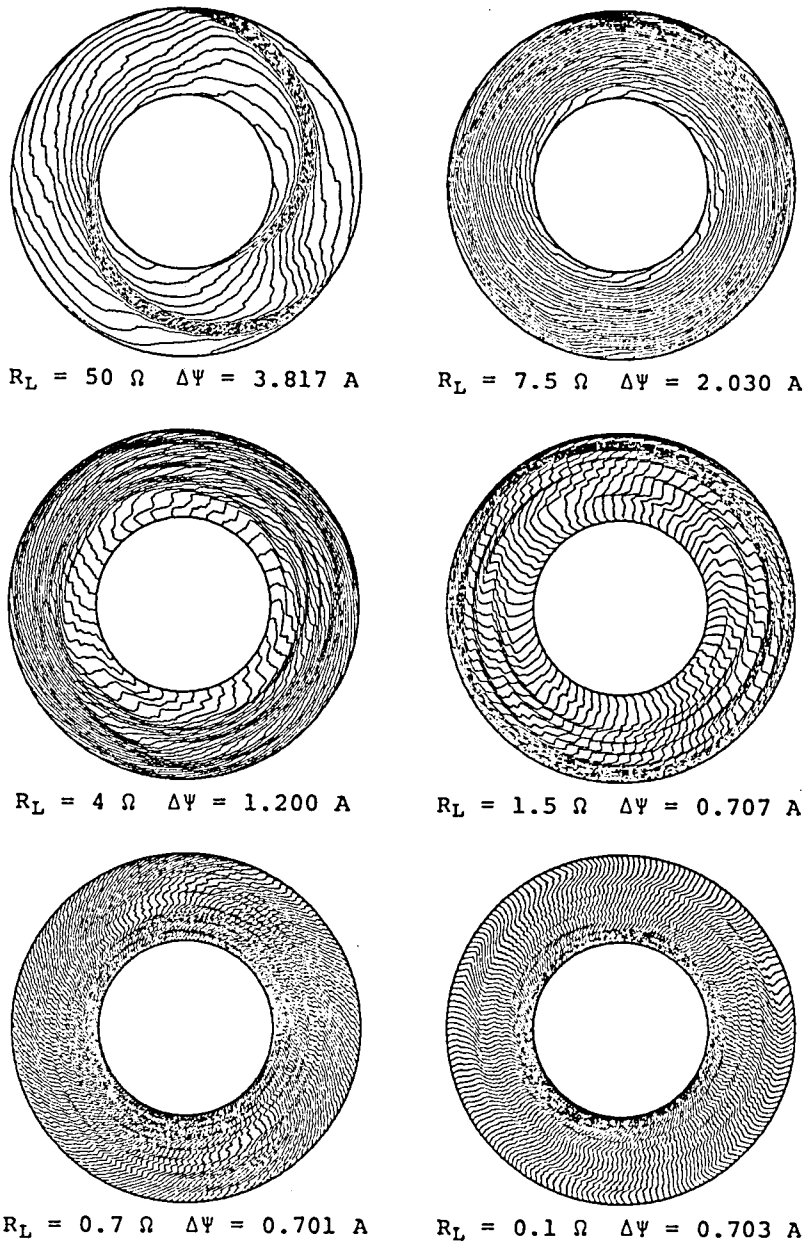

(c) Current distributions for various load resistances.

Fig. 7.5 Performance characteristics of generator using K-A_r in steady state for B = 3 T and $\varepsilon = 5 \times 10^{-5}$.

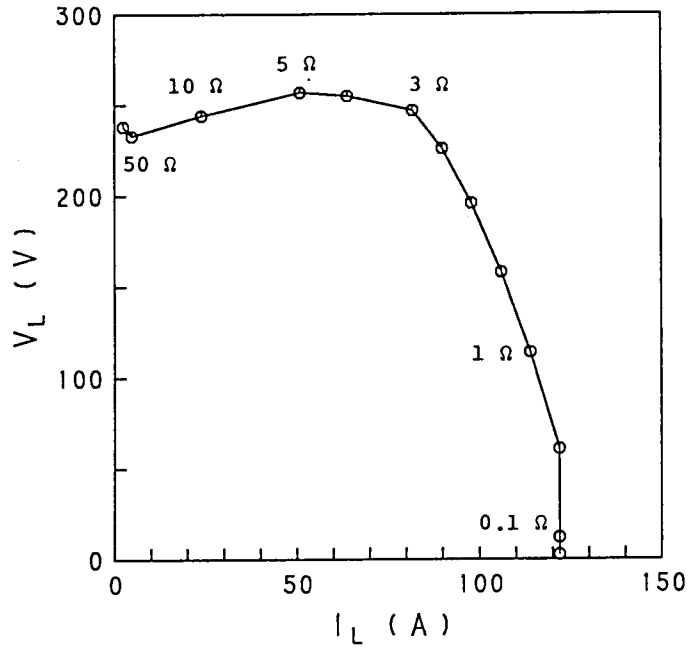

(a) Voltage-current curve.

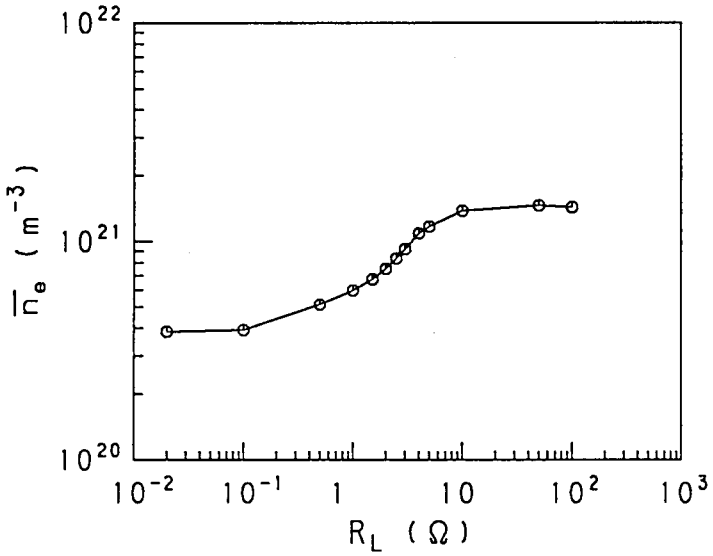

(b) Relation between load resistance and average electron density.

Fig. 7.6 Performance characteristics of generator using K-A_r in steady state for B = 3 T and $\varepsilon = 10^{-4}$.

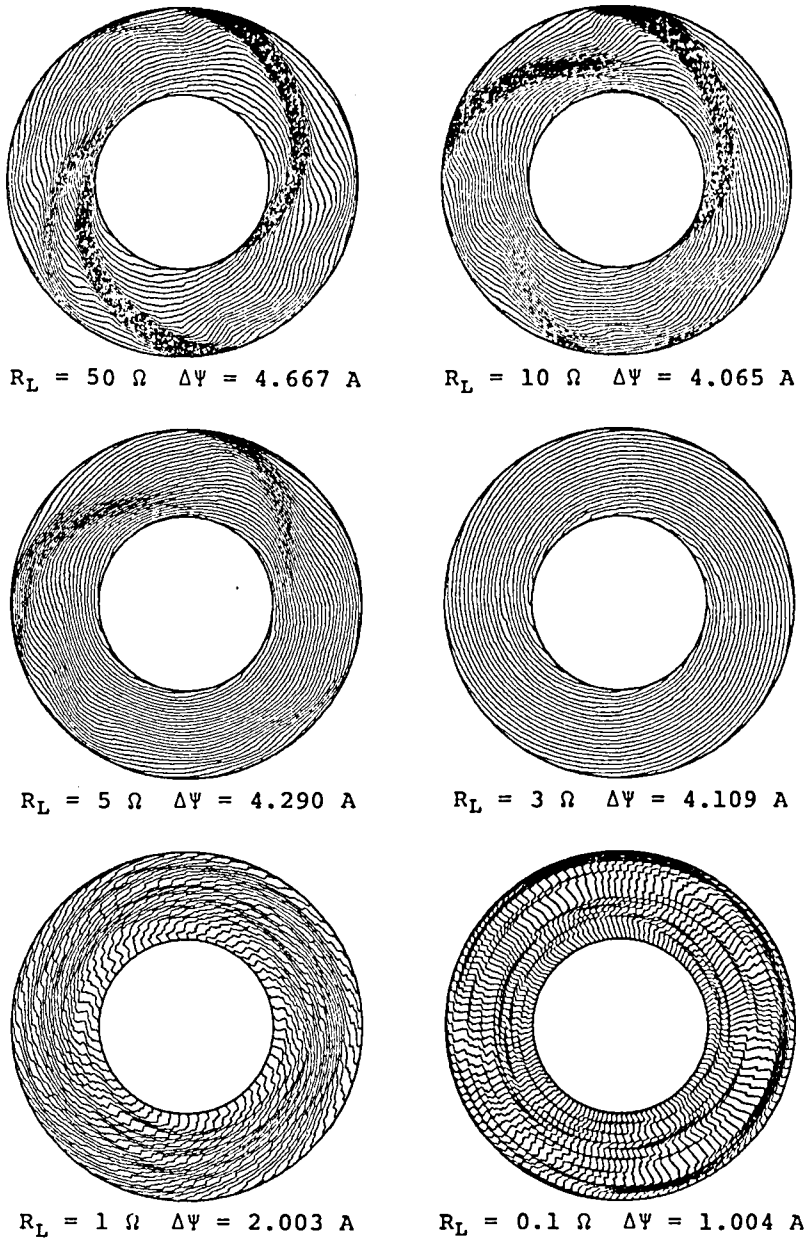

(c) Current distributions for various load resistances.

Fig. 7.6 Performance characteristics of generator using K-A_r in steady state for B = 3 T and $\varepsilon = 10^{-4}$.

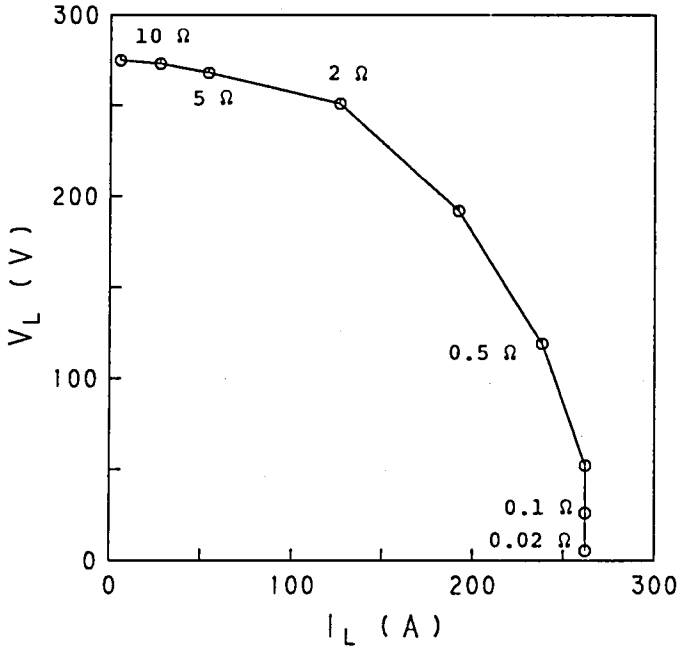

(a) Voltage-current curve.

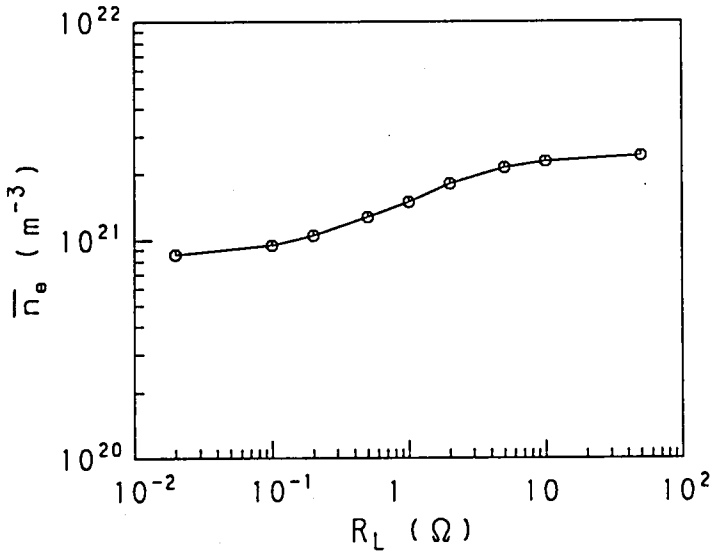

(b) Relation between load resistance and average electron density.

Fig. 7.7 Performance characteristics of generator using K-A_r in steady state for B = 3 T and $\varepsilon = 2 \times 10^{-4}$.

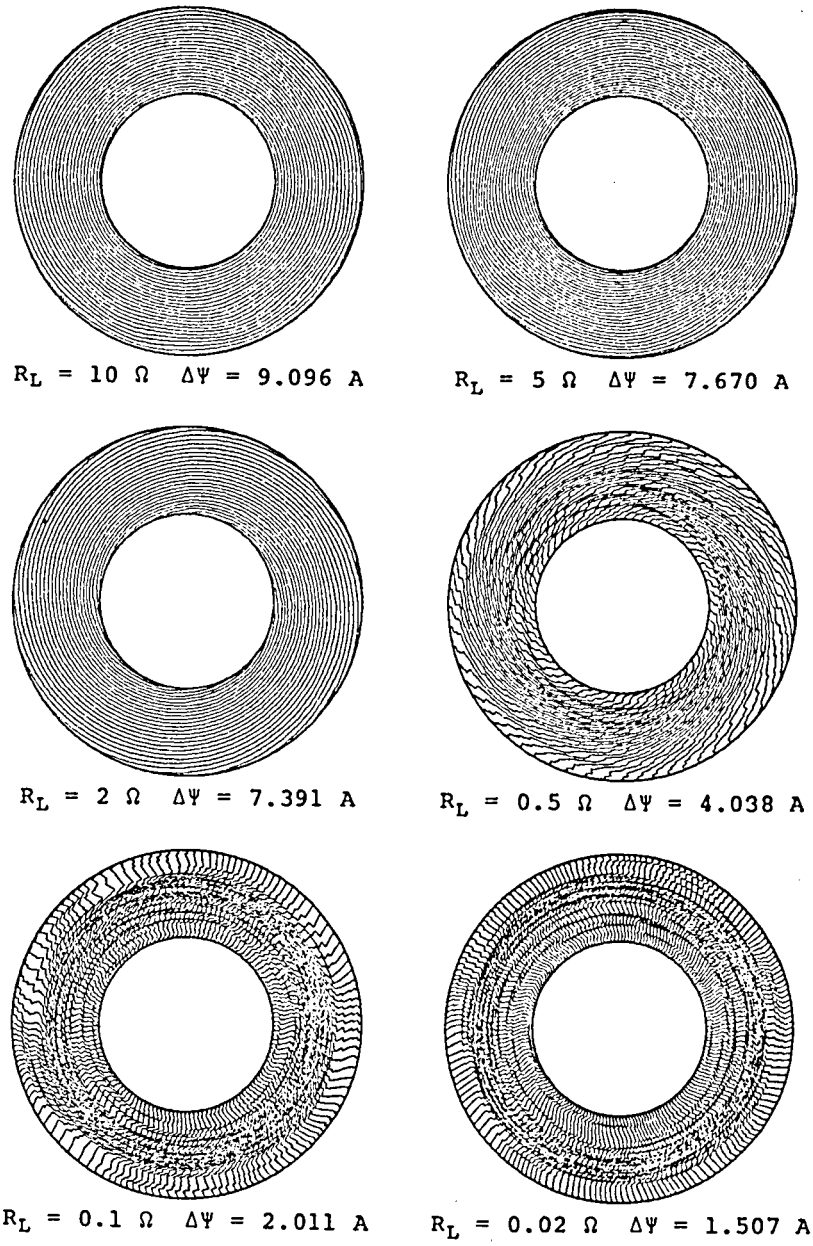

(c) Current distributions for various load resistances.

Fig. 7.7 Performance characteristics of generator using K-A_r in steady state for B = 3 T and $\varepsilon = 2 \times 10^{-4}$.

Figs. 7.6(a) to (c) and Figs. 7.7 (a) to (c) for $\varepsilon = 5 \times 10^{-5}$, 10^{-4} and 2×10^{-4} , respectively. Figures 7.6 and 7.7 tell that, as same as in the case where the cesium seeded argon plasma was used, the influences of the ionization instability on the voltage-current curves decrease as the seed fraction increases. Those figures also denote that, although the generator performance for the high load resistance is almost as same as in the case where the cesium seeded argon plasma is used, the region of the load resistance where the seed is fully ionized is very narrow and the average electron density $\bar{n}_e$ decreases rapidly as the load resistance becomes low. Consequently, the region of the load resistance where the seed is not fully ionized becomes wide and the load current in the region of small load resistance is considerably small in comparison with the case using the cesium seeded argon plasma.

Figures 7.5(a) to (c) show that the length of the inlet relaxation region has great influence on the generator performances in the case of $B = 3$ T and $\varepsilon = 5 \times 10^{-5}$. The voltage-current curve as shown in Fig. 7.5(a) is not obtained for $B = 3$ T but obtained for $B = 2$ T when the cesium seeded argon plasma is used. The above differences of the performance characteristics between the generators using the cesium seeded argon plasma and the potassium seeded argon one are considered to be originated from the fact that the ionization energy of the potassium is larger than that of the cesium.

7.4 Concluding Remarks

In this chapter, performance characteristics of the disk generator using the cesium or the potassium seeded argon plasma were studied by the numerical solution introduced in Chapter 5.

(1) The main results which were obtained for the generator using the cesium seeded argon plasma are as follows:

(a) When the magnetic flux density $B = 3$ T and the seed fraction

$\varepsilon = 5 \times 10^{-5}$, the output power is decreased remarkably by the ionization instability of the working plasma in the channel in the region of both high and low load resistances. Consequently, the load voltage does not decrease monotonously as the load current increases and the voltage-current curve of the generator has a peak at $R_L = 4\ \Omega$.

(b) The above results can qualitatively well explain the experimental results, which could not be explained by the previous researches.

(c) The relation between the current distribution in the channel and the voltage-current characteristics is made clear.

(d) The influence of the ionization instability on the voltage-current characteristics of the generator becomes small as the seed fraction becomes large, and the load voltage decreases monotonously as the load current increases for $\varepsilon = 2\times 10^{-4}$.

(e) When the magnetic flux density B is large, the main factor which deteriorates the generator performance is the ionization instability of the plasma. On the other hand, when B is small, the length of the inlet relaxation region has large influence on the generator performance.

(2) The main results which were obtained for the generator using the potassium seeded argon plasma are as follows:

(a) Although the generator performance in the region of high load resistance is almost the same as the generator using the cesium seeded argon plasma, the region of the load resistance in which the seed is fully ionized is very narrow and the load current in the region of low load resistance is considerably small in comparison with the case using the cesium seeded argon plasma. These are considered to be due to the fact that the ionization energy of the potassium is larger than that of the cesium.

(b) Even in the high magnetic flux density region, the length of the inlet relaxation region influences on the voltage-current characteristics.

CHAPTER 8

PERFORMANCE CHARACTERISTICS OF OUTFLOW DISK GENERATOR USING HELIUM GAS

8.1 Introduction

In Chapter 2 to 7, the generator using the cesium or the potassium seeded argon plasma was investigated, because such plasma is usually used in the experiments. However, recent experiments show that the output power density and the enthaply extraction ratio of the generator using helium gas are much higher than those of the one using argon gas[32]. This is due to the fact that the helium gas velocity becomes about 3 times as high as the argon gas one for a same Mach number, stagnation temperature and static pressure, because the argon atom is about 10 times as heavy as the helium atom. Moreover, wide stable region free from the ionization instability can be expected by using helium, because the ionization energy of the helium is larger than that of the argon.

Considering the above-mentioned, in this chapter, the performance characteristics of the disk generator using the cesium seeded helium plasma (C_s-H_e) are investigated. The differences between the performances of the generators using the helium and the argon are studied in detail, and it is clarified that the higher output power density and the wider stable region are obtained by the former than by the latter. Moreover, the influences of the seed fraction and the magnetic flux density on the generator performances are also made clear[53],[54].

8.2 Numerical Solution

The channel model, the basic equations, the assumptions and the numerical procedures mentioned in Chapter 5 can be used not only for the disk generator using argon plasma but also for the one using helium plasma. In the numerical analyses in this chapter, the collision cross section Q_h and the ionization and the recombination rate coefficients h_{fh} and h_{rh} of helium are chosen as follows(4),(55):

$$Q_h = 5.4\times10^{-20} \tag{8.1}$$

$$k_{fh} = 9.68\times10^{21}T_e^{3/2}\exp(-\frac{\varepsilon_{ih}}{kT_e})k_{rh} \tag{8.2}$$

$$k_{rh} = 1.09\times10^{-20}\cdot T_e^{-9/2} \tag{8.3}$$

where ε_{ih} is the ionization potential of helium.

8.3 Numerical Conditions

In this analysis, to enable the comparison of the performance characteristics between the generator using the argon gas and the one using the helium gas, almost same conditions used in Chapters 6 and 7 are adopted as numerical conditions, except the channel cross section, which is chosen so as to supply the heat input almost equal to the case where the argon gas is used. The values of the anode radius r_i, the cathode radius r_o, the channel cross section A, the channel width at the anode h_i, the stagnation and static temperatures of the gas T_s and T, the stagnation and static pressures p_s and p, the Mach number M, the gas velocity u_r, the helium number density n_{h0}, the magnetic flux density B, the seed fraction ε, the dimensions of an element Δr and $\Delta\theta$, the time step Δt used in this chapter are shown in Table 8.1. The relations of the electron number density n_e to the electron temperature T_e obtained by using Saha's equations for thermal ionization for

various seed fractions ε are shown in Fig. 8.1.

8.4 Performance Characteristics

8.4.1 Generator performances in typical case

At first, to make clear the current distribution and the other

Table 8.1 Numerical conditions used in calculations.

Anode radius	r_i	40 mm
Cathode radius	r_o	80 mm
Channel cross section	A	838 mm^2
Channel height at anode	h_i	3.33 mm
Stagnation temperature	T_s	2000 K
Static temperature	T	1134 K
Stagnation pressure	p_s	5.0 atm
Static pressure	p	1.2 atm
Mach number	M	1.5138
Gas velocity	u_r	3000 m/s
Helium number density	n_{h0}	$7.77\ 10^{24}$ m^{-3}
Magnetic flux density	B	4 T, 3 T
Seed fraction	ε	$2\ 10^{-4}$, 10^{-4}, $5\ 10^{-5}$
Dimension of element	Δr	0.5 mm
Dimension of element	$\Delta\theta$	$\pi/20$
Time step	Δt	0.167 μs

generator performances under typical conditions, numerical analyses are performed for various load resistances, where the magnetic flux density $B = 3$ T and the seed fraction $\varepsilon = 5 \times 10^{-5}$ are adopted. Here the initial condition is assumed that for $t<0$ only the helium is supplied the channel and for $t \geqq 0$ the cesium seeded helium plasma is done, which is the same as the one given in Section 6.3.

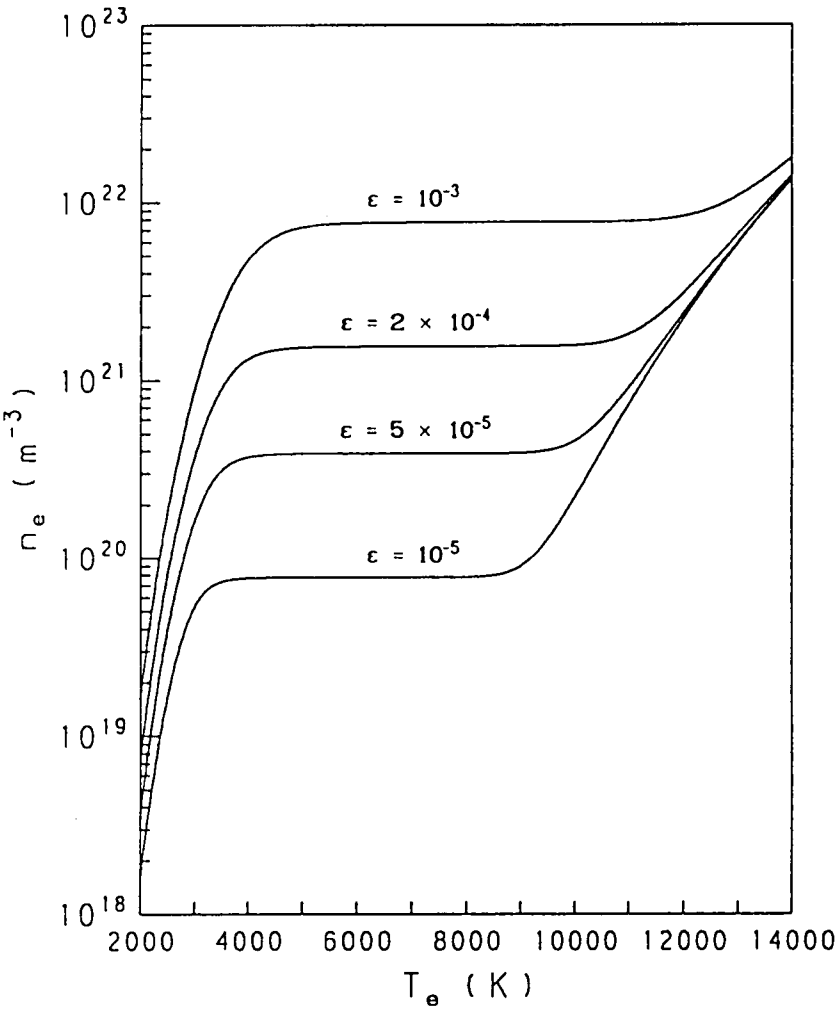

Fig. 8.1 Relations between electron temperature and electron density obtained by Saha's equations for various seed fractions.

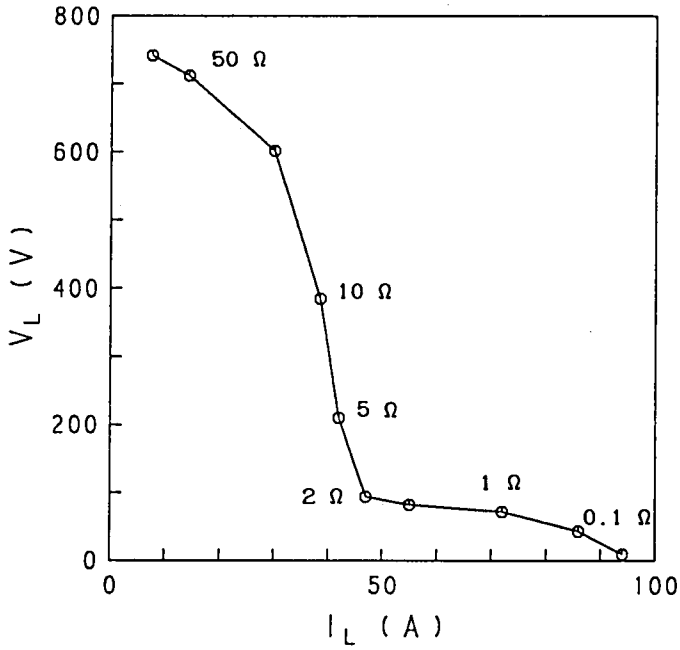

(a) Voltage-current curve.

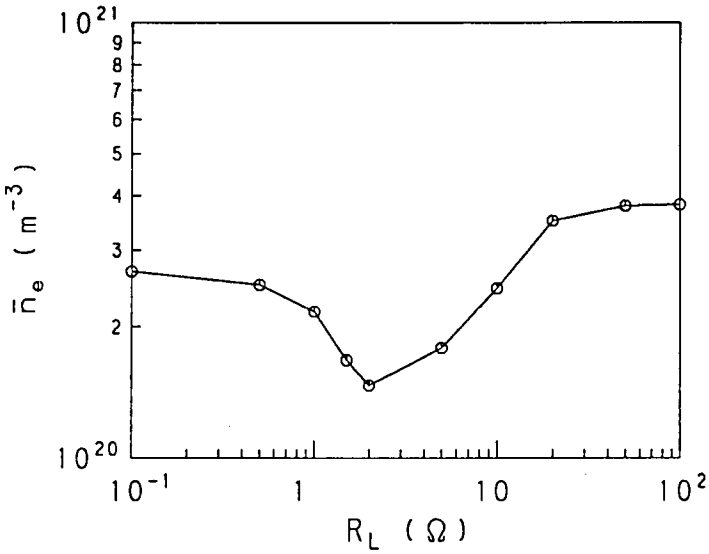

(b) Relation between load resistance and average electron density.

Fig. 8.2 Performance characteristics of generator using C_s-H_e in steady state for B = 3 T and $\varepsilon = 5 \times 10^{-5}$.

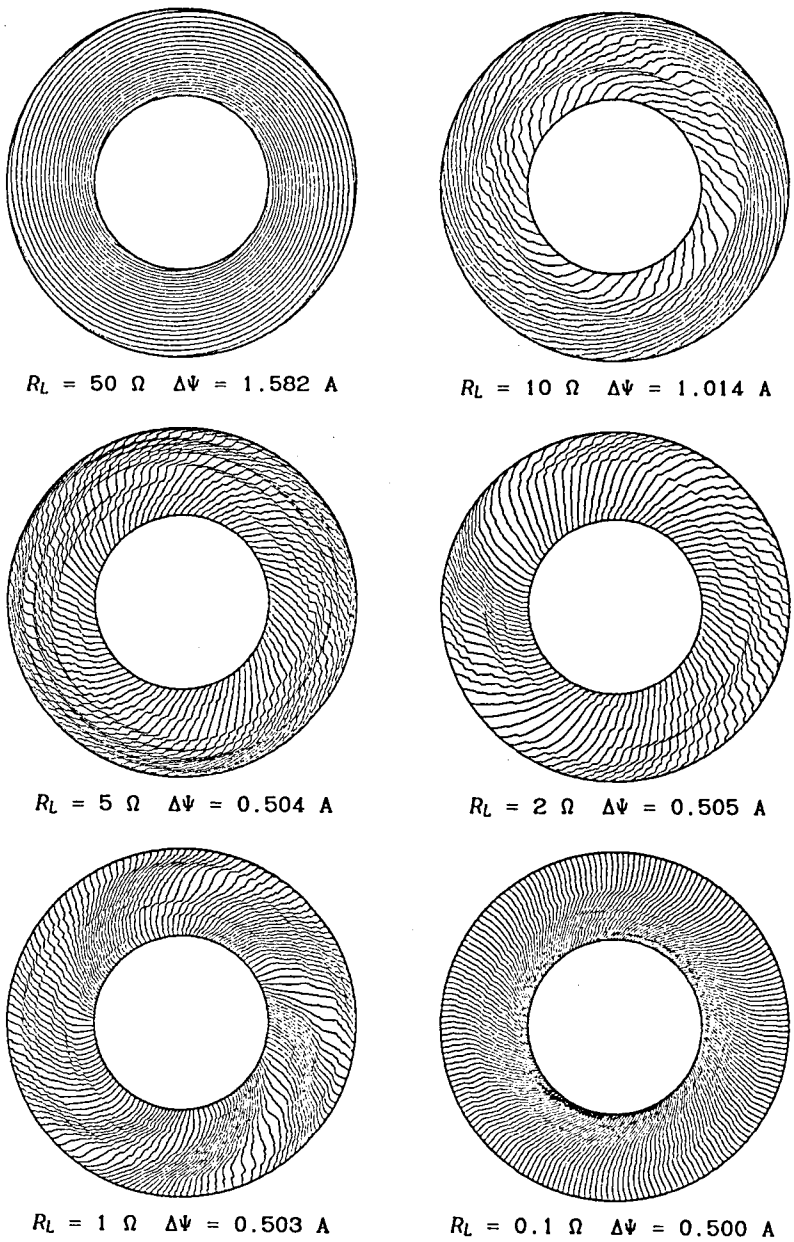

(c) Current distributions for various load resistances.

Fig. 8.2 Performance characteristics of generator using C_s-H_e in steady state for B = 3 T and $\varepsilon = 5 \times 10^{-5}$.

Also, by numerical investigations as same as in Section 6.3, it is ascertained that the current distribution in the channel becomes steady by $t \fallingdotseq 25\ \mu s$, which is about 1/3 of that in the case where the argon plasma is used. This is due to the fact that the velocity of the helium plasma is about 3 times as high as that of the argon plasma.

Next, Figures 8.2(a) to (c) show the voltage-current curve, the relation between the load resistance R_L and the average electron density $\bar{n}_e$ and the current distributions in the channel in the steady state, where $t = 30\ \mu s$, for $R_L = 50$, 10, 5, 2, 1 and 0.1 Ω. By comparing those figures with Figs. 7.1(a), (b) and (e), in which there are shown the performance characteristics of the generator using the cesium seeded argon plasma for the same magnetic flux density and the seed fraction, the following facts are made clear. The load voltage of the generator using the helium plasma is higher than the voltage of the one using the argon plasma, and the former load current is smaller than the latter one. The former high load voltage is due to the high velocity of the helium plasma and its small load current is due to the fact that the cross section of the former channel is 1/3 of the latter one as shown in Tables 6.1 and 8.1.

Since the output power P extracted from the generator is obtained by the relation of $P = I_L V_L$, Figures 8.2(a) and 7.1(a) tell that the maximum output power $P_{max} \fallingdotseq 18$ MW for both cases. Since the former cross section is 1/3 of the latter one, the former output power density is about 3 times as large as the latter one. Accordingly, comparing with the latter, the former has an advantage that the generator size which is required to generate a same output power becomes small.

Also, since the electron density $n_e \fallingdotseq 3.88 \times 10^{20}\ m^{-3}$ in the case of fully ionized seed as shown in Fig. 8.1, Figures 8.2(b) and (c) tell that the inhomogeneous current distribution, which is caused by the ionization instability of

partially ionized seed, occurs in both channels using the helium plasma and the argon plasma when the load resistance is low. On the other hand, when the load resistance is high, the noble gas is not ionized and so the current distribution is homogeneous when the helium plasma is used, although the noble gas is partially ionized and the current distribution is inhomogeneous when the argon plasma is used. Therefore, comparing with the generator using the argon, the one using the helium has advantages with respect to not only the channel size but also the stability of the plasma.

At last, Figure 8.2(a) shows that the output power takes a minimum value at $R_L = 2\ \Omega$, because the inlet relaxation region, which already covers half of the channel at $R_L = 5\ \Omega$, covers all over the channel at $R_L = 2\ \Omega$ as shown in Fig. 8.2(c). This is considered to be the same fact as mentioned in Subsection 7.2.3.

8.4.2 Influence of seed fraction on performance characteristics

To make clear the influence of the seed fraction on the generator performances, numerical analyses are performed for various load resistances, where the magnetic flux density $B = 3$ T and the seed fractions $\varepsilon = 10^{-4}$ and 2×10^{-4} are adopted, in addition to the case of $B = 3$ T and $\varepsilon = 5 \times 10^{-5}$ which was already studied in the preceding subsection.

The figures corresponding to Figs. 8.2(a) to (c) are shown in Figs. 8.3(a) to (c) for $\varepsilon = 10^{-4}$ and Figs. 8.4(a) to (c) for $\varepsilon = 2 \times 10^{-4}$, respectively. From these figures, it is seen that the load current increases as the seed fraction increases as well as in the case using the argon. Since the electron density $n_e \fallingdotseq 7.77 \times 10^{20}$ m^{-3} and 1.55×10^{21} m^{-3} for $\varepsilon = 10^{-4}$ and 2×10^{-4}, respectively, in the case of fully ionized seed, it is also made clear from these figures that the region of the load resistance in which the plasma is stable and the current distribution is homogeneous becomes wide as the seed fraction increases.

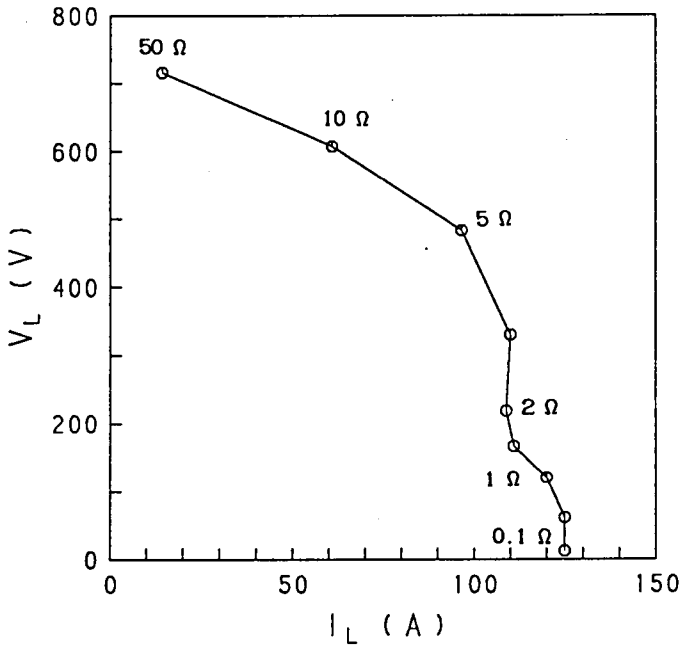

(a) Voltage-current curve.

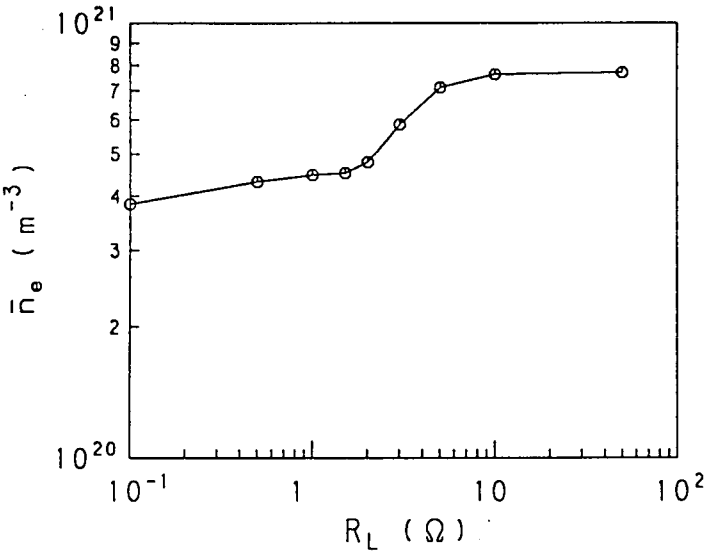

(b) Relation between load resistance and average electron density.

Fig. 8.3 Performance characteristics of generator using C_s-H_e in steady state for B = 3 T and $\varepsilon = 10^{-4}$.

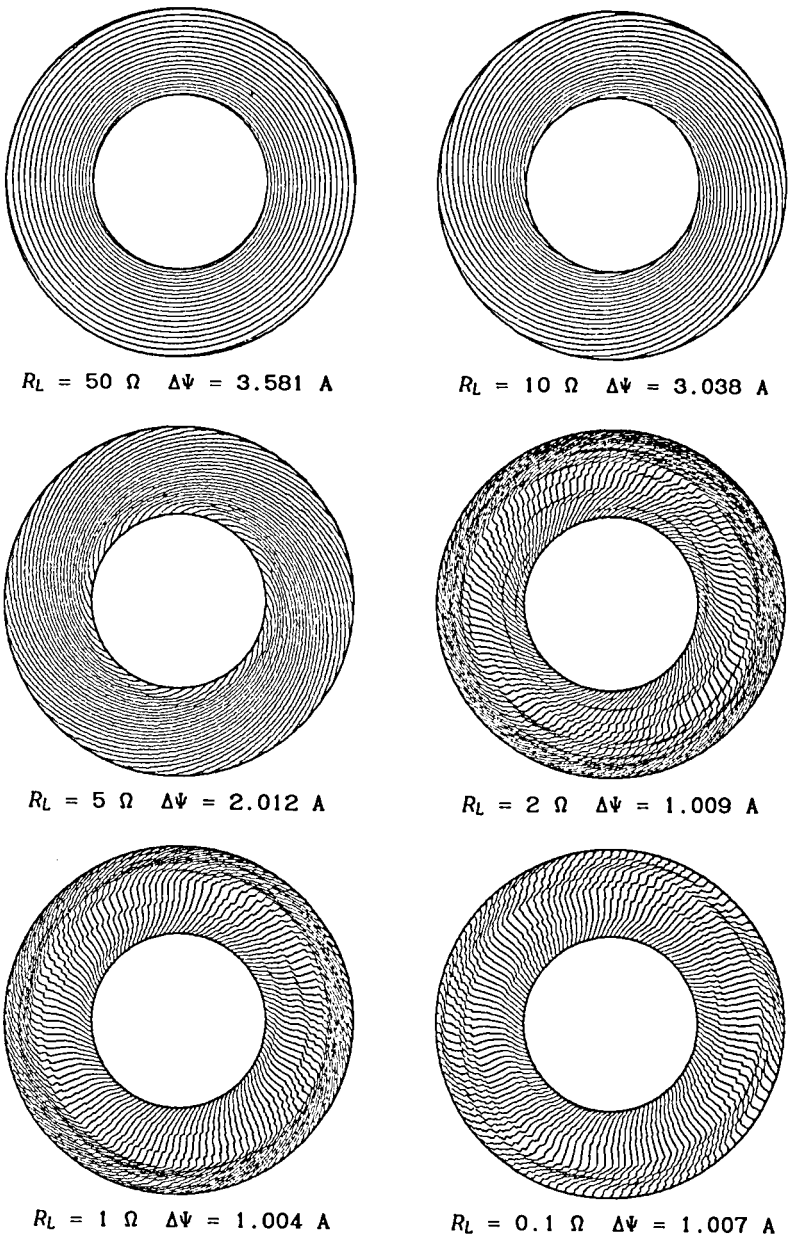

(c) Current distributions for various load resistances.

Fig. 8.3 Performance characteristics of generator using C_s-H_e in steady state for B = 3 T and $\varepsilon = 10^{-4}$.

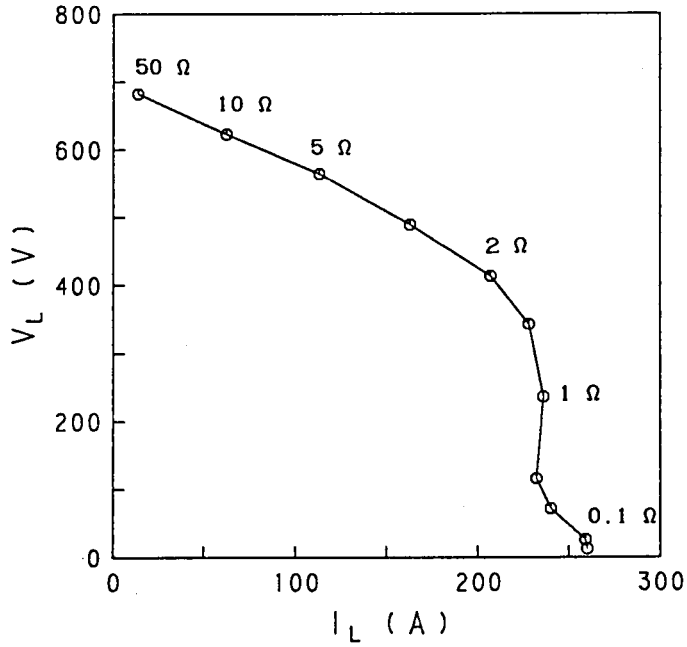

(a) Voltage-current curve.

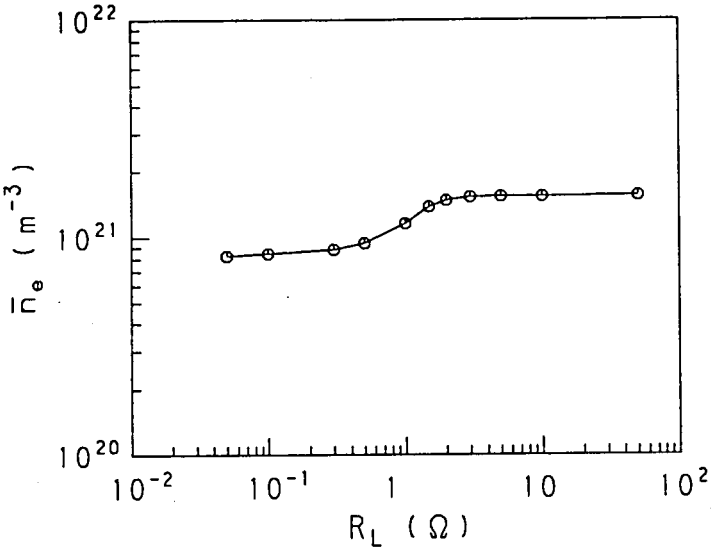

(b) Relation between load resistance and average electron density.

Fig. 8.4 Performance characteristics of generator using C_s-H_e in steady state for B = 3 T and $\varepsilon = 2 \times 10^{-4}$.

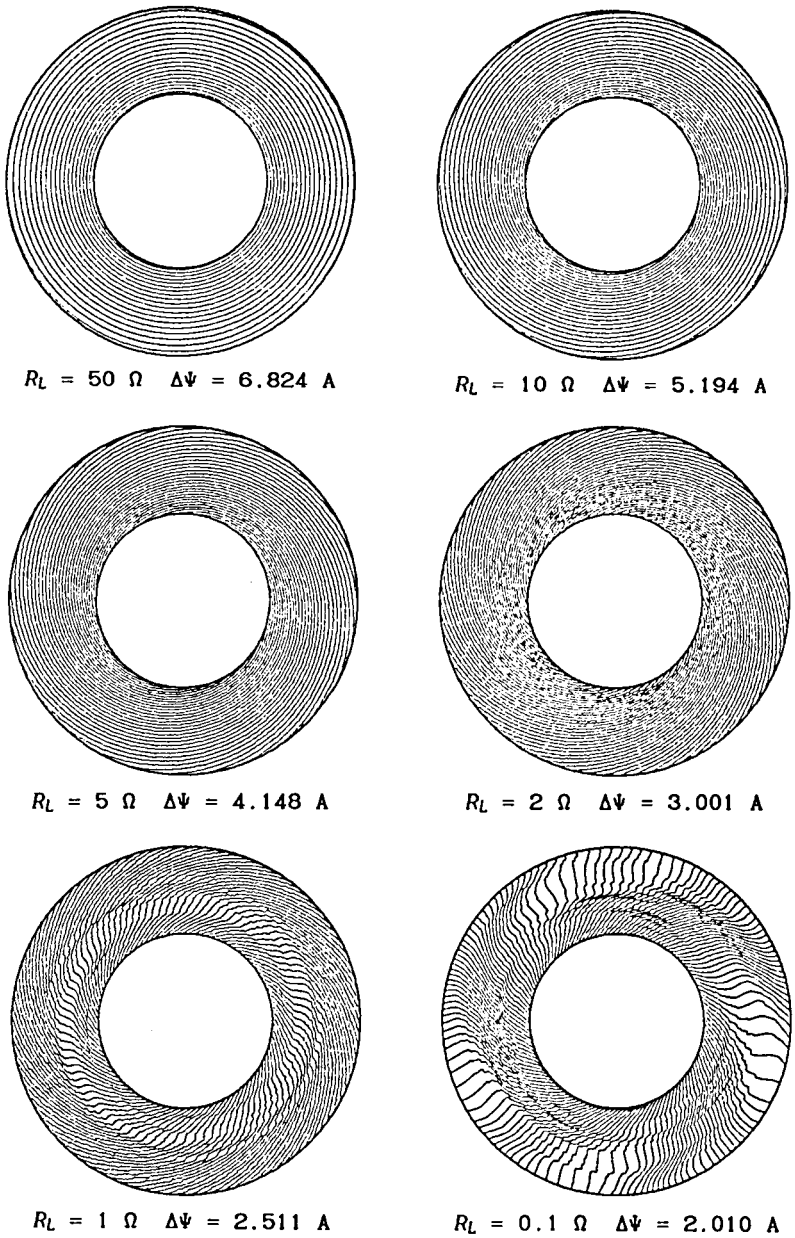

(c) Current distributions for various load resistances.

Fig. 8.4 Performance characteristics of generator using C_s-H_e in steady state for B = 3 T and $\varepsilon = 2 \times 10^{-4}$.

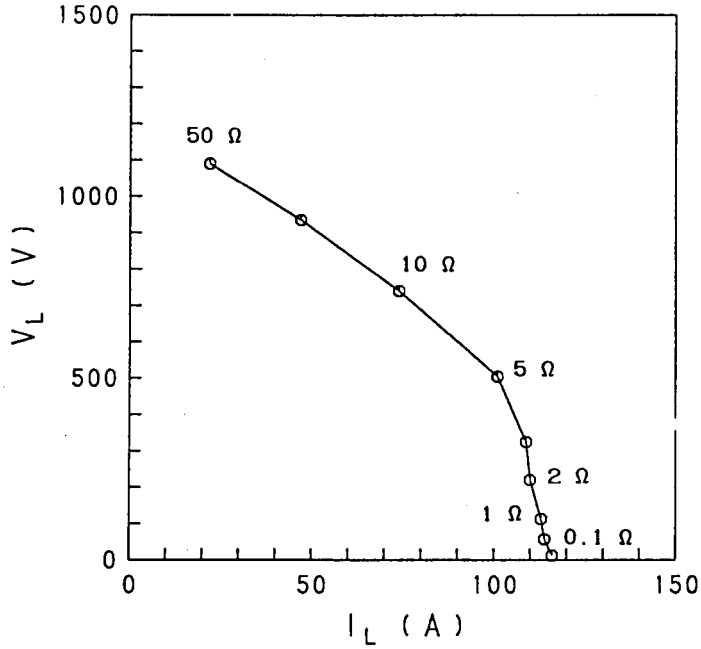

(a) Voltage-current curve.

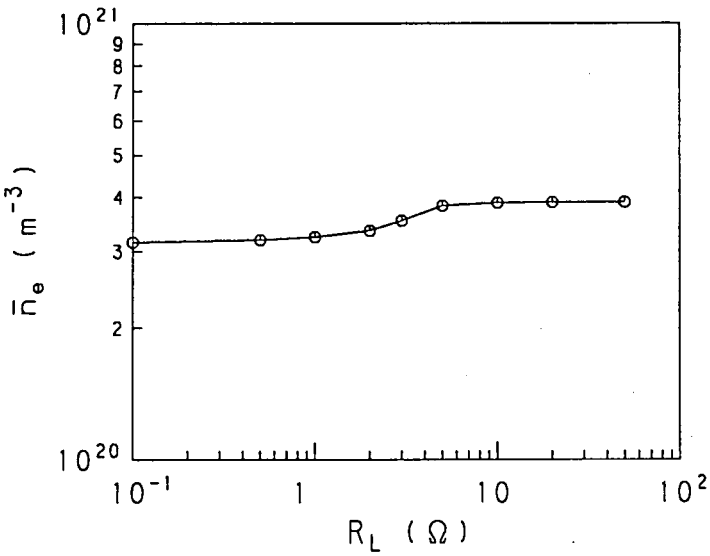

(b) Relation between load resistance and average electron density.

Fig. 8.5 Performance characteristics of generator using C_s-H_e in steady state for B = 4 T and $\varepsilon = 5 \times 10^{-5}$.

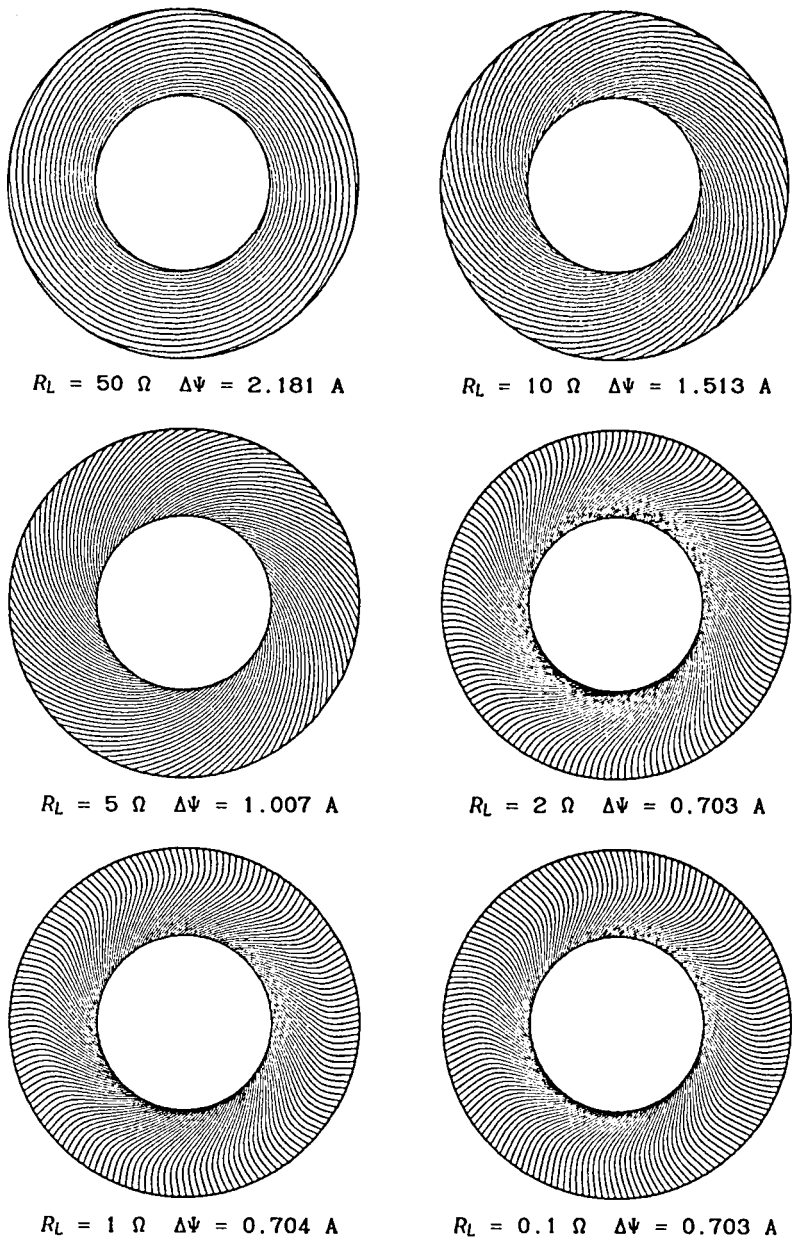

(c) Current distributions for various load resistances.

Fig. 8.5 Performance characteristics of generator using C_s-H_e in steady state for B = 4 T and $\varepsilon = 5 \times 10^{-5}$.

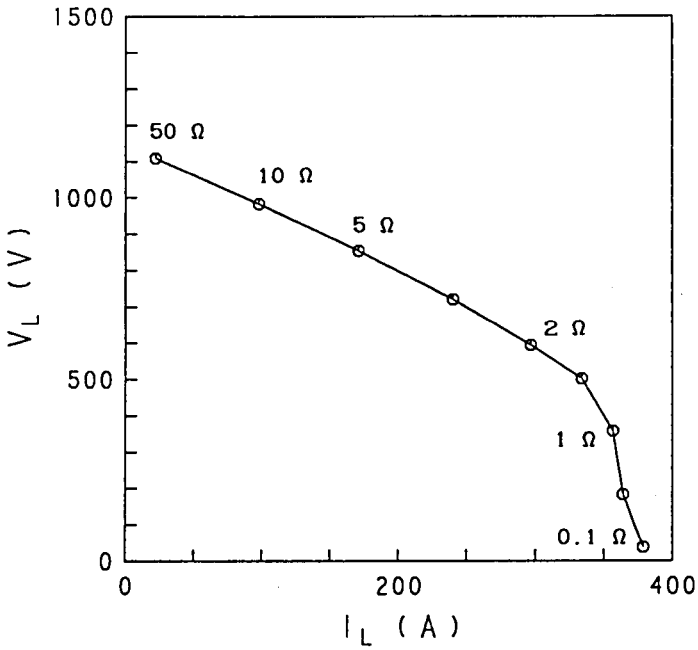

(a) Voltage-current curve.

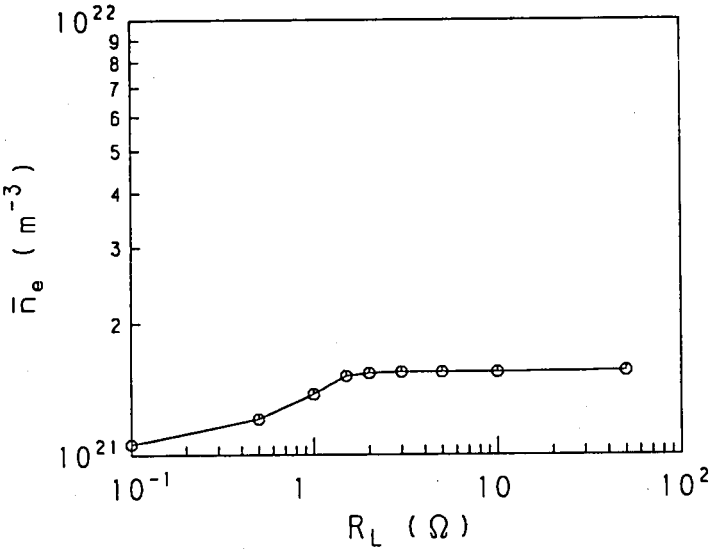

(b) Relation between load resistance and average electron density.

Fig. 8.6 Performance characteristics of generator using C_s-H_e in steady state for B = 4 T and $\varepsilon = 2 \times 10^{-4}$.

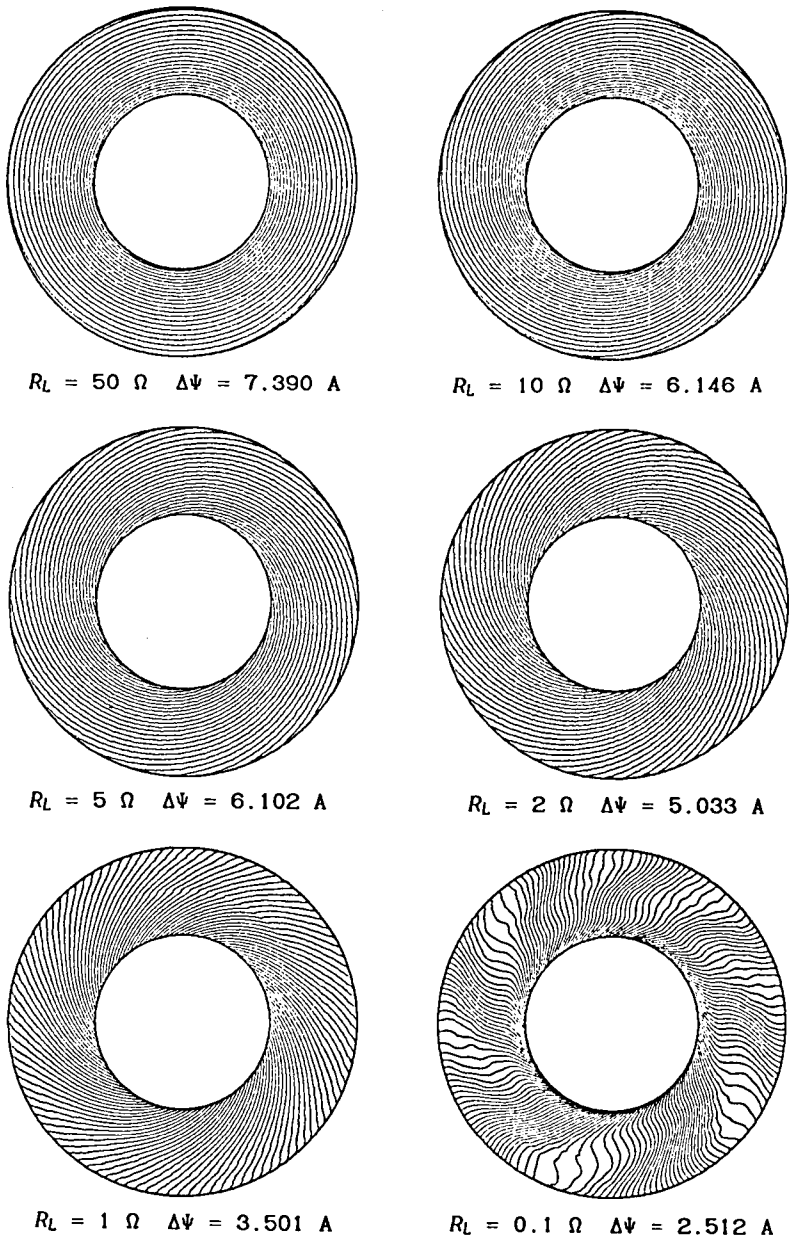

(c) Current distributions for various load resistances.

Fig. 8.6 Performance characteristics of generator using C_s-H_e in steady state for B = 4 T and $\varepsilon = 2 \times 10^{-4}$.

8.4.3 Influence of magnetic flux density on performance characteristics

From above-mentioned, it is seen that the helium gas is not ionized for B = 3 T. Therefore, in this subsection, let us study on the case of B = 4 T, where the seed fractions $\varepsilon = 5 \times 10^{-5}$ and 2×10^{-4} are adopted. The figures corresponding to Figs. 8.2(a) to (c) are shown in Figs. 8.5(a) to (c) and Figs. 8.6(a) to (c) for $\varepsilon = 5 \times 10^{-5}$ and 2×10^{-4} , respectively.

From these figures, it is made clear that the helium gas is still not ionized in the channel. Comparing Figs. 8.2(a) to (c) with Figs. 8.5(a) to (c) and Figs. 8.4(a) to (c) with Figs. 8.6(a) to (c), it is also made clear that the region of the load resistance in which the plasma is stable and the current distribution is homogeneous becomes wider and the generator performances are remarkably improved, when the magnetic flux density increases from B = 3 T to B = 4 T.

8.5 Concluding Remarks

In this chapter, the generator performances of the disk generator using the cesium seeded helium plasma were studied and the following main results were obtained.

(1) The load voltage of the generator using helium gas is higher than that of the one using argon gas, and the former load current is smaller than the latter one.

(2) The former output power density is about 3 times as large as the latter one. Accordingly, the generator using helium has the advantage that the generator size which is required to obtain a same output power is small. Moreover, the stability of the helium plasma is high in comparison with the argon one.

(3) The load current increases and the region of load resistance in which the plasma is stable becomes wide as the seed fraction increases.

(4) The region of load resistance in which the plasma is stable becomes wide and the generator performances are remarkably improved as the magnetic flux density increases.

ACKNOWLEDGMENTS

The author wishes to express his sincere and hearty appreciation to Professor Juro Umoto of Department of Electrical Engineering, Kyoto University for his continual guidances and encouragements to complete this work.

The author also wishes to express his thanks to Associate Professor Takehisa Hara of Department of Electrical Engineering, Kyoto University for his guidances and useful advices.

The author would like to thank Associate Professor Motoo Ishikawa, Instructor Tsuguo Ando of Department of Electrical Engineering, Kyoto University, Associate Professor Masaharu Yoshida of Gifu University and Associate Professor Mobuhiko Hayanose of Kobe Technical College for their useful discussions.

The author also acknowledges hearty assistances of Mr. Naomi Inoue, Mr. Yutaka Seki and other staffs of Professor J. Umoto's Laboratory.

REFERENCES

(1) Y. Aiyama: "The Status of Research and Development on MHD Power-Generation", Trans. I.E.E.J., Vol. 103, No. 12, pp. 1209-1216 (1983)

(2) S. Shioda, M. Ishikawa & J. Umoto: "Status Report of MHD Power Generation", J. At. Energy Soc. Japan, Vol. 27, No. 6, pp. 490-496 (1985)

(3) R. J. Rosa: "Experimantal Magnetohydrodynamic Power Generator", J. Appl. Phys., Vol. 31, No. 4, pp. 735-736 (1960)

(4) R. J. Rosa: "Magnetohydrodynamic Energy Conversion", McGraw-Hill, New York (1968)

(5) J. M. Sherick & G. E. Staats: "Status of MHD Testing at the U.S. Department of Energy's Component Development and Integration Facility(CDIF)", Proc. 21st Symp. on Eng. Asp. of MHD, 2.1.1-2.1.7 (1983)

(6) L. C. Farrar: "CDIF Status Report, Coal-Fired MHD Test", Proc. 3rd Workshop of the Japan-United States Co-operative Program, pp. 26-28 (1985)

(7) D. M. Jackson: "Status of Slag/Seed Interaction Testing at the Coal Fired Flow Facility", Proc. 22nd Symp. on Eng. Asp. of MHD, 11:1:1-11:1:12 (1984)

(8) Y. Kusaka, et al.: "Experimental Investigation of ETL Mark VII MHD Facility", Proc. 21st Symp. on Eng. Asp. of MHD, 2.8.1-2.8.16 (1983)

(9) B. Zauderer: "Discharge Structure and Stability of a Nonequilibrium Plasma in a Magnetohydrodynamic Channel", Phys. Fluids, Vol. 11, No. 12, pp. 2577-2585 (1968)

(10) G. Brederlow, K. J. Witte & H. Zinko, "Investigation of the Discharge Structure in a Noble Gas Alkali MHD Generator

Plasma", Part I & Part II, AIAA J., Vol. 11, No. 8, pp. 1065-1079 (1973)

(11) S. Shioda, et al.: "Power Generation Experiments and Prospects of Closed Cycle MHD with Fully Ionized Seed", Proc 7th Int. Conf. on MHD Elec. Power Gen., Vol. II, pp. 685-695 (1980)

(12) J. Blom, et al.: "High Power Density Experiments in the Eindhoven Shocktunnel MHD Generator", Proc. 6th Int. Conf. on MHD Elec. Power Gen., Vol III, pp. 73-88 (1975)

(13) C. H. Marston, et al.: "Design of 50MW Closed Cycle MHD Blowdown Experiment", Proc. 15th Symp. on Eng. Asp. of MHD, VI.2.1-VI.2.9 (1976)

(14) Ku. Yoshikawa, et al.: "Operation and Thermal Performance of Pebble Bed Regenerative Heat Exchanger for Blow-Down Experiments of Closed Cycle MHD Power Generation", Proc. 5th Symp. on Efficient Use of Energy and Direct Elec. Power Gen., S4.2.1-S4.2.31 (1983)

(15) H. Yamasaki, et al.: "Recent Results in the Closed Cycle MHD Power Generation Experimental Facility FUJI-1", *ibid*, S6.2.1-S6.2.10 (1983)

(16) H. Yamasaki, et al.: "Experimental Studies of Closed Cycle Disk Generator in the FUJI-1 Facility", Proc. 9th Int. Conf. on MHD Elec. Power Gen., Vol. II, pp. 341-350 (1986)

(17) W. F. H. Merck & P. Masse: "Electric and Gasdynamic Performance of the Eindhoven Blow-Down Experiment", Proc. 22nd Symp. on Eng. Asp. of MHD, 7:4:1-7:4:20 (1984)

(18) J. L. Kerrebrock: "Nonequilibrium Ionization Due to Electron Heating: I. Theory", AIAA J., Vol. 2, No. 6, pp. 1072-1080 (1964)

(19) A. Solbes: "Quasi-Linear Plane Wave Study of Electrothermal Instabilities", Proc. 4th Int. Symp. on MHD, Vol. 1, pp. 499-518 (1968)

(20) A. H. Nelson & M. G. Haines: "Analysis of the Nature and Growth of Electrothermal Waves", Plasma Phys., Vol. 11,

pp. 811-837 (1969)

(21) T. Nakamura & W. Riedmüller: "Stability of Nonequilibrium MHD Plasma in the Regime of Fully Ionized Seed", AIAA J., Vol. 12, No. 5, pp. 661-668 (1974)

(22) Ki. Yoshikawa: "The Effect of Nonuniformity on Rare Gas Plasma Magnetohydrodynamic Power Generation", Doctor Thesis (1973)

(23) E. P. Velikhov, et al.: "Numerical Experiment on Ionization Instability Development in a Low Temperature Magnetized Plasma", Proc. 11th Symp. on Eng. Asp. of MHD, pp. 1-4 (1969)

(24) L. L. Lengyel: "Current and Potential Distributions in Nonequilibrium MHD Plasmas at High Magnetic Field Strengths", AIAA J., Vol. 9, No. 10, pp. 1957-1962 (1971)

(25) R. J. Unkls: "A Numerical Investigation of the Current and Density Distributions for a Nonequilibrium Plasma in a Segmented Electrode Duct", Plasma Phys., Vol. 15, pp. 1053-1065 (1973)

(26) J. H. Blom: "Relaxation Phenomena in an MHD Generator with Pre-Ionizer", Doctor Thesis (1973)

(27) M. Ishikawa, J. Umoto & T. Hara: "Two Dimensional Analysis of a Diagonal Type Nonequilibrium Plasma MHD Generator", Trans. I.E.E.J., Vol. 96-A, No. 12, pp. 559-566 (1976)

(28) T. Hara, A. Veefkind & L. H. Th. Rietjens: "Numerical Simulation of the Inhomogeneous Discharge Structure in Noble Gas MHD Generators", AIAA J., Vol. 20, No. 11, pp. 1473-1480 (1982)

(29) T. Hara, Y. Inui & J. Umoto: "Inhomogeneous Discharge Structures in Nonequilibrium MHD Generator Channels", Trans. I.E.E.J., Vol. 103-A, No. 9, pp. 477-484 (1983)

(30) S. Shioda, et al.: "Experimental Studies of an Inert Gas Disk MHD Generator with a Small Seed Fraction", Proc. 18th Symp. on Eng. Asp. of MHD, D-2.6.1-D-2.6.7 (1979)

(31) N. Harada, et al.: "Experimental Studies on the Performance of Closed Cycle MHD Generators with Fully Ionized Seed", Proc.

22nd Symp. on Eng. Asp. of MHD, 3:1:1-3:1:14 (1984)

(32) H. Yamasaki, et al.: "Closed Cycle MHD Disk Experiments at T.I.T", Proc. 23rd Symp. on Eng. Asp. of MHD, pp. 430-438 (1985)

(33) T. Hara, Y. Inui & J. Umoto: "Analysis of Streamer Structure Development in the Inlet Region of Nonequilibrium MHD Generator Channels", Trans. I.E.E.J., Vol. 105-A, No. 2, pp. 63-70 (1985)

(34) L. Spitzer: "Physics of Fully Ionized Gases", Interscience Publishers, New York (1956)

(35) M. I. Hoffert & H. Lien: "Quasi-One-Dimensional Nonequilibrium Gas Dynamics of Partially Ionized Two-Temperature Argon", Phys. Fluids, Vol. 10, No. 8, pp. 1769-1777 (1967)

(36) T. Takeshita & L. M. Grossman: "Excitation and Ionization Processes in Non-Equilibrium MHD Plasmas", Proc. 4th Int. Symp. on MHD, Vol. 1, pp. 191-206 (1968)

(37) H. W. Riepmann & A. Roshko: "Elements of Gasdynamics", John Wiley & Sons, London (1960)

(38) T. Hara, J. Umoto & Y. Inui: "Streamer Structure in Noble Gas MHD Channels", Proc. 5th Symp. on Efficient Use of Energy and Direct Elec. Power Gen., S2.2.1-S2.2.15 (1983)

(39) T. Hara, Y. Inui & J. Umoto: "Numerical Simulation of Ionization of MHD Convection Plasma", I.E.E.J. Trans on RM・SA, RM-83-44・SA-83-34, pp. 33-41 (1983)

(40) T. Hara, J. Umoto & Y. Inui: "Numerical Analysis of the Nature of the Streamers in Noble Gas MHD Generator", Proc. 8th Int. Conf. on MHD Elec. Power Gen., Vol. 4, pp. 136-139 (1983)

(41) A. Veefkind, et al.: "Investigation of the Nonequilibrium Condition in a Shock-Tunnel Driven Noble Gas MHD Generator", Proc. 7th Int. Conf. on MHD Elec. Power Gen., Vol. II, pp. 703-710 (1980)

(42) Y. Inui, T. Hara & J. Umoto: "Discharge Structures in Nonequilibrium Faraday Type MHD Generator Channels", Proc. 8th

Symp. on Efficient Use of Energy and Direct Elec. Power Gen., pp. 150-159 (1986)

(43) T. Hara, Y. Inui & J. Umoto: "Relation between the Load Resistance and the Streamer Structure in the Inlet Region of Nonequilibrium MHD Generator", Convention Records at the Annual Meeting in Kansai District of I.E.E.J., G1-32 (1982)

(44) Y. Inui, T. Hara & J. Umoto: "Effects of the Seed Fraction on the Discharge Phenomena in Nonequilibrium MHD Generator", *ibid*, G1-11 (1983)

(45) Y. Inui, T. Hara & J. Umoto: "Numerical Analysis of the Discharge Structures in Nonequilibrium Disk Type MHD Generator", Trans. I.E.E.J., Vol. 105-A, No. 6, pp. 313-320 (1985)

(46) Y. Inui, T. Hara & J. Umoto: "Analysis of the Discharge Structure in Nonequilibrium Disk Type MHD Generator", I.E.E.J. Trans on ESC, ESC-84-28, pp. 111-120 (1984)

(47) Y. Inui, T. Hara & J. Umoto: "Numerical Simulation of the Discharge Structure in Nonequilibrium Disk Type MHD Generator", Proc. 23rd Symp. on Eng. Asp. of MHD, pp. 461-475 (1985)

(48) Y. Inui, T. Hara & J. Umoto: "Formation Process of the Inhomogeneous Discharge Structure in Nonequilibrium Disk Type MHD Generator", Convention Records at the Annual Meeting of I.E.E.J., 1084 (1984)

(49) S. Shioda & H. Yamasaki: "Generation Experiments with a Disk MHD Generator under the Conditions of Fully Ionized Seed", Proc. 6th Int. Conf. on MHD Elec. Power Gen., Vol. III, pp. 105-114 (1975)

(50) Y. Inui, T. Hara & J. Umoto: "Analysis of the Voltage-Current Characteristics of the Nonequilibrium Disk Type MHD Generator", I.E.E.J. Trans. on ESC, ESC-85-9 pp.77-86 (1985)

(51) Y. Inui, T. Hara & J. Umoto: "Numerical Simulation of the Voltage-Current Characteristics of the Nonequilibrium Disk

Type MHD Generator", Trans. I.E.E.J., Vol. 106-A, No. 2, pp. 47-54 (1986)

(52) Y. Inui, T. Hara & J. Umoto: "Voltage-Current Characteristics of Nonequilibrium Disk Type MHD Generator", Convention Records at the Annual Meeting of I.E.E.J., 1153 (1985)

(53) Y. Inui, T. Hara & J. Umoto: "Analysis of Nonequilibrium Disk Type Generator Using Helium Plasma", I.E.E.J. Trans. on ESC, ESC-86-18, pp. 11-20 (1986)

(54) Y. Inui, T. Hara & J. Umoto: "Numerical Simulation of Nonequilibrium Disk Type MHD Generator Using Helium Plasma", Convention records at the Annual Meeting in Kansai District of I.E.E.J., G1-31, (1986)

(55) E. Hinnov & J. G. Hirschberg: "Electron-Ion Recombination in Dense Plasmas", Physical Review, Vol. 125, No. 3, pp. 795-801 (1962)